Fakultät für Informatik

Development of Silent Multi-contrast Magnetic Resonance Imaging Acquisition Techniques

Xin Liu

Vollständiger Abdruck der von der Fakultät für Informatik der Technischen Universität München zur Erlangung des akademischen Grades einer

Doktorin der Naturwissenschaften (Dr. rer. nat.)

genehmigten Dissertation.

Vorsitzender:
    Prof. Dr.-Ing. Darius Burschka
Prüfende der Dissertation:
    1. Prof. Dr. Björn Menze
    2. Priv.-Doz. Dr. Marion I. Menzel

Die Dissertation wurde am 05.07.2021 bei der Technischen Universität München eingereicht und durch die Fakultät für Informatik am 26.10.2021 angenommen.

ABSTRACT

Magnetic Resonance Imaging (MRI) is a powerful imaging modality in biomedical field by providing non-invasive assessment of tissues properties and metabolism. The rich contrast mechanisms of MRI make it a valuable technique in both scientific and diagnostic applications. The acoustic noise during MRI scan causes discomfort and mental stress in patients. This thesis focuses on developing multi-contrast MRI acquisition schemes with reduced acoustic noise.

First, the Echo Planar Imaging (EPI) sequence with sinusoidal readout gradient was implemented and validated in phantom experiments. Sequence optimization aimed at adapting the acoustic spectrum of the gradient waveform to the scanner frequency response function, and the acoustic noise reduction can be up to 5 dBA. Second, the diffusion prepared rotating ultrafast imaging sequence (RUFIS) is presented with techniques to compensate for eddy current artifact, T1 recovery effect and bulk motion sensitivity. In phantom studies, artifact-free images were acquired, and diffusion measurements were consistent with diffusion weighted EPI when using the phase cycling method to reduce T1 recovery effect. Volunteer scans showed residual motion artifact caused by brain pulsation. The proposed sequence showed less image distortion and achieved acoustic noise reduction of 35 dBA compared to diffusion weighted EPI sequences. The third part of the thesis aims to develop a silent 3D method for T1 and proton density mapping by using inversion recovery prepared RUFIS sequence with an interleaved undersampling scheme. Accelerated reconstruction was achieved by constraining the signal evolution to a temporal subspace which was learned from the signal model. Accuracy and repeatability of the method was accessed in repeated experiments with phantom and volunteers. The results were highly consistent with the gold standard method and literature values. The acoustic noise measured at the scanner isocenter was 2.6 dBA higher compared to the in-bore background.

In summary, this thesis presents silent acquisition techniques for diffusion, T1 and proton density contrasts and compared them to conventional methods. The proposed methods could greatly improve patient comfort during examination and therefore increase the acceptance of the procedure.

ZUSAMMENFASSUNG

Die Magnetresonanztomographie (MRT) ist eine leistungsstarke bildgebende Modalität im biomedizinischen Bereich, die eine nicht-invasive Bewertung der Gewebeeigenschaften und des Stoffwechsels ermöglicht. Die reichhaltigen Kontrastmechanismen der MRT machen sie zu einer wertvollen Technik sowohl für wissenschaftliche als auch für diagnostische Anwendungen. Der akustische Lärm während der MRT-Untersuchung verursacht bei Patienten Beschwerden und mentalen Stress. Diese Arbeit konzentriert sich auf die Entwicklung von Multi-Kontrast MRT-Erfassungsschemata mit reduziertem akustischem Rauschen.

Zunächst wurde die Echo Planar Imaging (EPI) -Sequenz mit sinusförmigen Auslesegradienten implementiert und in Phantomexperimenten validiert. Die Sequenzoptimierung zur Anpassung des akustischen Spektrums der Gradientenwellenform an die Frequenzgangfunktion des Scanners und die Reduzierung des akustischen Lärm kann bis zu 5dBA betragen. Zweitens wird die diffusionskodierte 'rotating ultrafast imaging sequence (RUFIS)' mit Techniken vorgestellt, um Wirbelstromartefakte, T1-Relaxation und Bewegungsartefakte zu kompensieren. In Phantomstudien wurden artefaktfreie Bilder aufgenommen, und die Diffusionsmessungen stimmten mit dem diffusionsgewichteten EPI überein, wenn die phase cycling' methode verwendet wurde, um den T1-Wiederherstellungs Effekt zu verringern. Probanden Scans zeigten Restbewegungsartefakte, die durch Gehirnpulsation verursacht wurden. Die vorgeschlagene Sequenz zeigte eine geringere Bildverzerrung und erreichte eine akustische Lärmreduzierung von 35 dBA im Vergleich zu diffusionsgewichteten EPI-Sequenzen. Der dritte Teil der Arbeit zielt darauf ab, eine stille 3D-Quantifizierungstechnik für T1 und Protonendichte zu entwickeln, indem eine mit Inversionspuls vorbereitete RUFIS-Sequenz mit einem verschachtelten Unterabtastungsschema verwendet wird. Eine beschleunigte Rekonstruktion wurde erreicht, indem die Signalentwicklung auf einen zeitlichen Unterraum beschränkt wurde, der aus dem Signalmodell gelernt wurde. Auf die Genauigkeit und Wiederholbarkeit der Methode wurde in wiederholten Experimenten mit Phantom und Probanden zugegriffen. Die Ergebnisse stimmten in hohem Maße mit der Goldstandardmethode und den Literaturwerten überein. Das am Isozentrum des Scanners gemessene akustische Rauschen war im Vergleich zum Hintergrund in der Öffnung lediglich um 2,6 dBA höher.

Zusammenfassend wurden in dieser Arbeit stille Erfassungstechniken für

Diffusions-, T1- und Protonendichtekontraste vorgestellt und mit konventionellen Methoden verglichen. Die vorgeschlagenen Methoden könnten den Patientenkomfort während der Untersuchung erheblich verbessern und daher die Akzeptanz des Verfahrens erhöhen.

Contents

Chapter 1

MRI Basic Principles

Magnetic Resonance Imaging (MRI) is a non-invasive tomographic imaging modality based on the well-known nuclear magnetic resonance (NMR) phenomenon. It has been widely used in medical science to study tissue structure and function of human body . In this chapter, the basic principle of MRI is presented, beginning with generation and detection of the NMR signal, followed by spatial encoding and image reconstruction, finally, the basic pulse sequences and diffusion imaging are introduced.

1.1 Magnetization, Resonance and Relaxation Times

The NMR phenomenon was first introduced in 1946, independently by Purcell at Harvard and Bloch at Stanford, who later shared the Nobel Prize in 1952. As implied by the name, NMR consists of magnetized nuclei and the resonance phenomenon. Although the underlying mechanism should start from subatomic level, i.e. quantum mechanics, the NMR signal can be well described by the classical vector model, as it is the collective signal from a huge number of nuclei in the object to be imaged. In NMR experiments, the ensemble of magnetized nuclei momentum (bulk magnetization) is activated by externally applied radio-frequency (RF) excitation and reaches resonance state. The signal can be observed when the system is returning to equilibrium through relaxation.
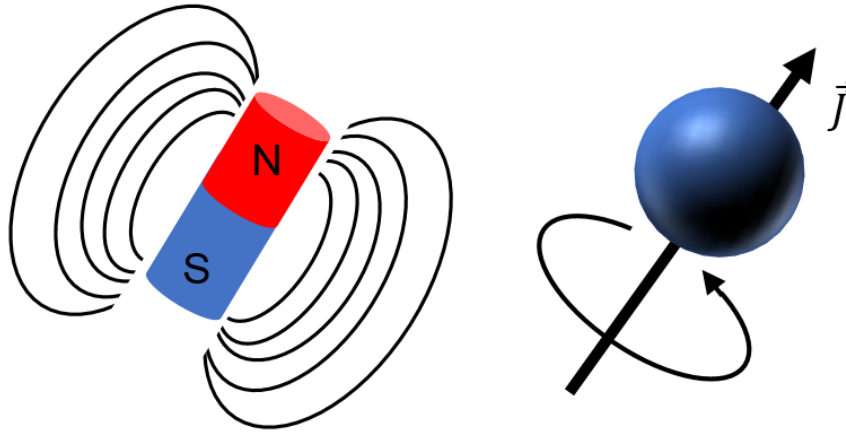
Figure 1.1: Analogy of nuclei to microscopic magnets. Nuclei with nonzero angular momentum $\vec{J}$ possess magnetic moment $\vec{\mu}$, and can be regarded as microscopic bar magnets.

1.1.1 Magnetization and Larmor Frequency

Spinning Nuclei and Magnetic Moment

We learned in basic physic and chemistry, that biological tissue is made up of molecules, which can then be broke down to atoms consisting of positively-charged nuclei and a cloud of orbiting electrons with negative charges. The nucleus consists of protons and neutrons, and carries most of the atomic mass. Protons have definite charge ($\approx 1.60 \times 10^{-19}$ coulomb) and mass ($\approx 1.67 \times 10^{-27}$ kg), neutrons have nearly the same mass and are electronically neutral. The atomic number is defined as the number of protons contained in the nucleus, and the atomic mass is defined as the sum number of protons and neutrons. As a fundamental property of nuclei, those with odd atomic numbers or weights, such as hydrogen with one proton, possess an angular momentum $\vec{J}$, also called spin. For a geometric analogy, spin can be perceived as physical rotation, similar to a gyroscope rotating around its axis.

Hydrogen atom is abundant in biological tissue, its nucleus contains a single proton with positive charge. According to electromagnetism, moving electrical charge, i.e. current, creates magnetic field. As described above, the nucleus of hydrogen has non-zero spin, thus it generates a magnetic field around it, called *nuclear magnetic dipole moment*, represented by a vector quantity $\vec{\mu}$. The spin nuclear magnetic moment can be regarded as a microscopic bar magnet, as shown in Figure 1.1.

Table 1.1: The gyromagnetic ratio γ of some NMR-active nuclei

Nucleus	Spin	Gyromagnetic Ratio $10^6 rad \cdot s^{-1} \cdot T^{-1}$
^{1}H	1/2	267.52
^{13}C	1/2	67.28
^{19}F	1/2	251.66
^{31}P	1/2	108.29

The relationship between spin angular momentum $\vec{J}$ and magnetic moment $\vec{\mu}$ is described by Eq. (1.1).

$$\vec{\mu} = \gamma \vec{J} \tag{1.1}$$

where γ is a nucleus-dependent physical constant called *gyromagnetic ratio*. The γ values of some nuclei are listed in table 1.1.

Nuclei with non-zero angular momentum possess microscopic magnetic moment. The magnitude of magnetic moment, denoted as $|\vec{\mu}|$, is determined by the nuclear spin quantum number.

$$|\vec{\mu}| = \gamma \hbar \sqrt{I(I+1)} \tag{1.2}$$

Where $\hbar$ is the Planck's constant divided by 2π, and I is the *nuclear spin quantum number*, which takes integer or half-integer values from zero:

$$I = 0, \frac{1}{2}, 1, \frac{3}{2}, \ldots \tag{1.3}$$

From Eq. (1.2) we can tell that a nuclei has non-zero spin and magnetic moment if $I \neq 0$, thus NMR-active. For nuclei with even numbers of both protons and neutrons, such as ^{12}C and ^{16}O, I $= 0$. For nuclei with odd numbers of both protons and neutrons, I values are positive integers, such as ^{14}N (I=1) and ^{10}B (I=3). For nuclei with odd sum number of protons and neutrons, such as ^{1}H and ^{13}C, I $= \frac{1}{2}$.

Although the magnitude of $\vec{\mu}$ is certain for particular nucleus, its direction is totally random due to thermal random motion in absence of external magnetic field. Therefore, no net magnetization exists for the macroscopic object at thermal equilibrium. When applying an external magnetic field, the number of possible energy level for a given nuclei is (2I+1) and net magnetization for the
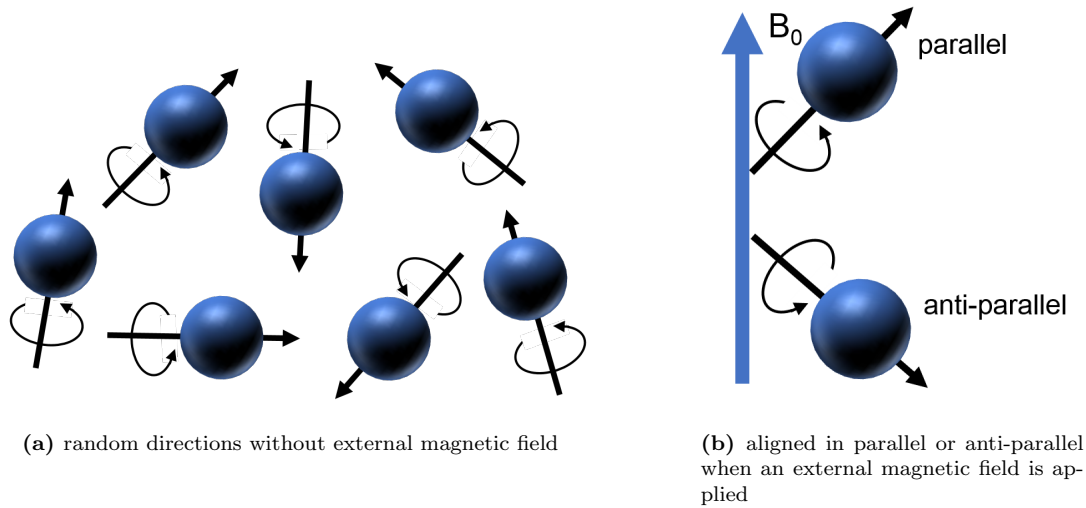
(a) random directions without external magnetic field

(b) aligned in parallel or anti-parallel when an external magnetic field is applied

Figure 1.2: Nuclear magnetic moments

macroscopic object can be achieved.

Precession and Larmor Frequency

Recall the concept of nuclear spin quantum number I in section 1.1.1. Nucleus like ^{1}H and ^{13}C has I $= \frac{1}{2}$ and are called spin $\frac{1}{2}$ system. When exposed to a strong external magnetic field, spin vectors line up and produce net magnetization for the object to be imaged. Assume the external magnetic field has strength B_0 and along the z-direction in the laboratory frame,

$$\vec{B}_0 = B_0 \vec{k} \tag{1.4}$$

In laboratory frame, we used x, y, z to denote the orthogonal axes, and $\vec{i}$, $\vec{j}$, $\vec{k}$ as their respective unit directional vectors. As an essential characteristic in the quantum mechanics, spin vectors adopt one of the $(2I + 1)$ discrete orientations. There are two available orientations for spin $\frac{1}{2}$ system: parallel (pointing up) and anti-parallel (pointing down), as shown in Figure 1.2.

While the z-component $\vec{\mu}_z$ is either parallel or anti-parallel to the direction of B_0, the direction of transverse component $\vec{\mu}_{xy}$ remains random. Consider $\vec{\mu}$ as a isolated magnetic moment without mutual interactions. Using classical treatment, the torque experienced by $\vec{\mu}$ from the external magnetic field $B_0 \vec{k}$ equals to
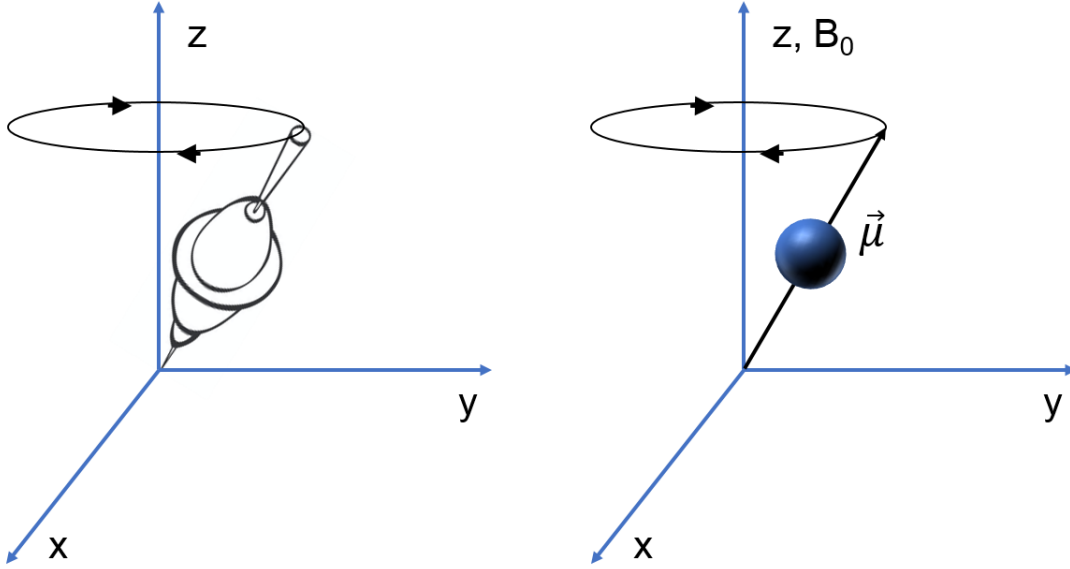
Figure 1.3: Analogy of nuclear precession to a spinning top wobbling about the gravitational axis.

the rate of change of its angular momentum $\vec{J}$,

$$\frac{d\vec{J}}{dt} = \vec{\mu} \times B_0 \vec{k} \tag{1.5}$$

According to Eq. (1.1), $\vec{\mu} = \gamma \vec{J}$, thus

$$\frac{d\vec{\mu}}{dt} = \gamma \vec{\mu} \times B_0 \vec{k} \tag{1.6}$$

The solution of Eq. (1.6) is shown in Eq. (1.7),

$$\begin{cases} \mu_{xy}(t) = \mu_{xy}(0)e^{-i\gamma B_0 t} \\ \mu_z(t) = \mu_z(0) \end{cases} \tag{1.7}$$

Eq. (1.7) describes the motion of $\vec{\mu}$ in presence of $\vec{B}_0$, the longitudinal component remains constant and the transverse component rotate clockwise when observed against the direction of $\vec{B}_0$. The precession of $\vec{\mu}$ around $\vec{B}_0$ is called nuclear precession, which is analogous to a spinning top wobbling about the gravitational axis, as illustrated in Figure 1.3.

It's evident from Eq. (1.7) that the angular frequency of nuclear precession is dependent on B_0, known as Larmor Frequency,

$$\omega_0 = \gamma B_0 \tag{1.8}$$

Bulk Magnetization

We use macroscopic magnetization vector $\vec{M}$ to illustrate the collective behavior of the spin system under external magnetic field $\vec{B}_0$. $\vec{M}$ is the vector sum of the microscopic magnetization $\vec{\mu}$ in the object to be imaged,

$$\vec{M} = \sum_{n=1}^{N} \vec{\mu}_n \tag{1.9}$$

where $\vec{\mu}_n$ is the magnetization of the nth nuclear spin, and N_s is the total number of spins in the object to be imaged.

Recall from the previous section, in absence of external $\vec{B}_0$, $\vec{\mu}$ takes random directions and the net magnetization $\vec{M} = 0$. When applying an external $\vec{B}_0$ to spin $\frac{1}{2}$ system, $\vec{\mu}$ takes one of the two possible directions, parallel or anti-parallel with respect to the $\vec{B}_0$ direction. According to the quantum mechanics, the energy of interaction between $\vec{\mu}$ and $\vec{B}_0$ can be described as:

$$E = -\vec{\mu} \cdot \vec{B}_0 = -\mu_z B_0 = -\gamma \hbar m_I B_0 \tag{1.10}$$

where m_I is the *magnetic quantum number* and takes value of $\frac{1}{2}$ and $-\frac{1}{2}$. For parallel spins, $m_I = \frac{1}{2}$ and

$$E_\uparrow = -\frac{1}{2}\gamma \hbar B_0 \tag{1.11}$$

For anti-parallel spins, $m_I = -\frac{1}{2}$ and

$$E_\downarrow = \frac{1}{2}\gamma \hbar B_0 \tag{1.12}$$

Therefore, the parallel spin are at lower-energy state while the anti-parallel spins are at higher-energy state. The energy difference between the two directions of spins are

$$\Delta E = E_\downarrow - E_\uparrow = \gamma \hbar B_0 \tag{1.13}$$

(a) Zeeman splitting   (b) magnetic moments
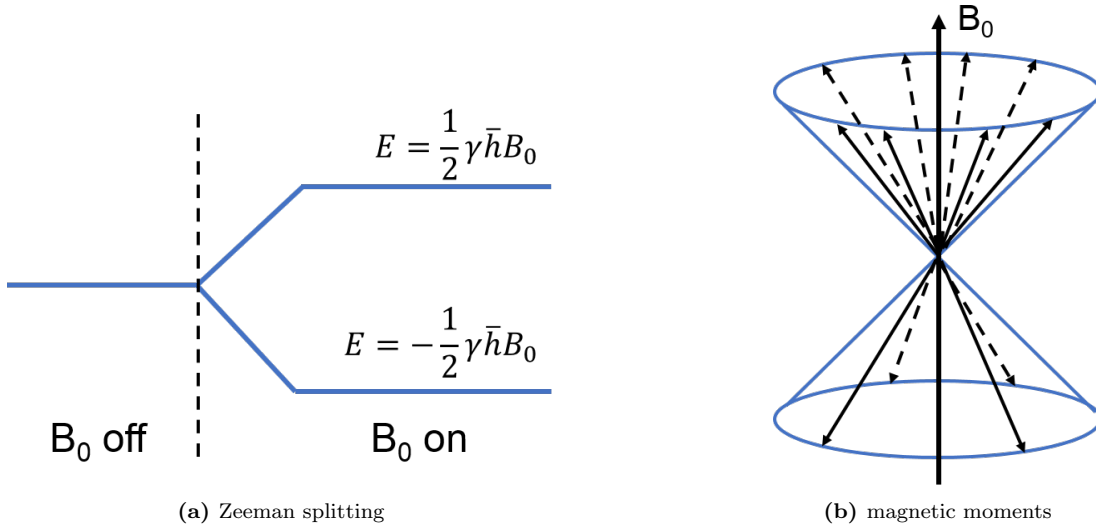
Figure 1.4: Bulk magnetization

The phenomenon illustrated in Eq. (1.13)is called Zeeman splitting, that the spin energy split into two levels after applying an external magnetic field, as shown in Figure 1.4.

According to the the Boltzmann distribution, the spin state with lower energy (parallel) has a higher probability to be occupied,

$$\frac{N_\uparrow}{N_\downarrow} = exp\left(\frac{\Delta E}{KT_s}\right) \tag{1.14}$$

where $N_\uparrow$ and $N_\downarrow$ is the number of parallel and anti-parallel spins, T_s is the absolute temperature of the spin system, and K is the Boltzmann constant ($1.38\times 10^{-23}J \cdot K^{-1}$).

In practice, $\Delta E = \gamma \hbar B_0 \ll KT_s$, therefore using first-order approximation,

$$\frac{N_\uparrow}{N_\downarrow} \approx 1 + \frac{\gamma \hbar B_0}{KT_s} \tag{1.15}$$

Therefore,

$$N_\uparrow - N_\downarrow \approx N_s \frac{\gamma \hbar B_0}{2KT_s} \tag{1.16}$$

Eq. (1.16) states that there are a small excess fraction of parallel spins as

they are more likely to occupy the state with lower energy. The uneven spin distribution generates a bulk magnetization $\vec{M}$ at thermal equilibrium pointing to the z-direction, same as the external $\vec{B}_0$. The magnitude of the $\vec{M}$

$$|\vec{M}| = M_z = \frac{\gamma^2 \hbar^2 B_0 N_s}{4KT_s} \tag{1.17}$$

This indicates that the magnitude of $\vec{M}$ is proportional to the external $\vec{B}_0$ strength and the total number of spins N_s, inversely proportional to the absolute temperature T_s. Since N_s and T_s cannot be changed for the object being imaged, the only controllable factor is the field strength B_0. For clinical applications, B_0 typically ranges from 0.2T to 2T. Note the above equations are only valid for spin $\frac{1}{2}$ system.

1.1.2   RF Excitation and the Bloch equation

The last section described how the net magnetization $\vec{M}$ is generated in the spin system under external $\vec{B}_0$. The next step is to measure it. According to Eq. (1.17), $|\vec{M}|$ is order of magnitudes smaller than the external B_0. Thus it is literally impossible to measure $|\vec{M}|$ when it's parallel to B_0 at thermal equilibrium. Nevertheless, when $\vec{M}$ is tipped down to transverse plane using RF pulses, it's a significant signal and can be measured with a detector according to the Faraday law of electromagnetic induction .

RF Pulses and Resonance Condition

In NMR, the external force that tip down $\vec{M}$ from z-axis to the transverse plane comes from RF pulse, denoted as $\vec{B}_1$. $\vec{B}_1$ is short-lived magnetic field perpendicular to $\vec{B}_0$, oscillating in the radio-frequency range. The $\vec{B}_1$ field strength is much weaker compared to $\vec{B}_0$ (typically $\vec{B}_1$=50 mT when $\vec{B}_0$=1.5 T). Typically a RF pulse takes the general form:

$$\vec{B}_1(t) = 2\vec{B}_1^e(t)cos(\omega_{rf}t + \varphi)\vec{i} \tag{1.18}$$

where $\vec{B}_1^e(t)$ is the pulse envelope function, ω_{rf} is the carrier frequency and φ is the initial phase.

In the quantum model, the energy carried by electromagnetic radiation with frequency ω_{rf} is:

$$E_{rf} = \hbar\omega_{rf} \tag{1.19}$$

To coherently induce spin transition to another energy level, the radiation energy E_{rf} and the energy difference between adjacent spin states ΔE should be the same. Therefore,

$$\Delta E = \gamma\hbar B_0 = \hbar\omega_0 = \hbar\omega_{rf} = E_{rf} \tag{1.20}$$

that is,

$$\omega_0 = \omega_{rf} \tag{1.21}$$

Eq. (1.21) shows the *resonance condition*, that induce coherent spin transition, the $\vec{B}_1$ field must rotate in the same frequency as spin precession.

To more conveniently describe the effects of RF excitation and relaxation in the following paragraphs, we can use the rotating frame of reference, whose transverse plane is rotating about $\vec{B}_0$ at angular frequency ω. When resonance condition is met and ω equals to Larmor frequency, $\omega = \omega_0 = \omega_{rf}$, both precessing spins and $\vec{B}_1$ field are stationary. To distinguish it from the conventional laboratory frame, we use x', y', z' to denote the orthogonal axes, and $\vec{i}'$, $\vec{j}'$, $\vec{k}'$ as unit directional vectors of this frame.

Bloch equation

The time-dependent changes of $\vec{M}$ during excitation and relaxation can be quantitatively described by *Bloch equation*, which takes the general form in NMR context:

$$\frac{d\vec{M}}{dt} = \gamma\vec{M} \times \vec{B} - \frac{M_x\vec{i} + M_y\vec{j}}{T_2} - \frac{(M_z - M_z^0)\vec{k}}{T_1} \tag{1.22}$$

where M_z^0 is the magnitude of $\vec{M}$ at thermal equilibrium under $\vec{B}_0$, T_1 and T_2 are the time constants characterizing the process of $\vec{M}$ returning to thermal equilibrium after it has been disturbed, i.e. the relaxation process, which will be described in section 1.1.3.

As is often the case, the RF pulse duration is way shorter than T_1 and T_2. Thus it is acceptable to use only the first term of Eq. (1.22) to describe the behavior

of $\vec{M}$ during the RF excitation, and the Bloch equation takes the simple form:

$$\frac{d\vec{M}}{dt} = \gamma \vec{M} \times \vec{B} \tag{1.23}$$

It is worth noting that the above equation shares identical form as Eq. (1.6) on spin precession, only the $\vec{\mu}$ is replaced by $\vec{M}$. Consider the equation in the rotating frame, where the $\vec{B}_1$ field is static and along x'-axis in the transverse plane, as illustrated in figure. Similar to the behavior of free spins in presence of $\vec{B}_0$, $\vec{M}$ precesses about $\vec{B}_1$, moves away from z'-axis to the transverse plane, until the $\vec{B}_1$ field is switched off. When observed in the laboratory frame, the motion looks like a spiral from z-axis to transverse plane as shown in figure.

For hard RF pulses, the flip angle α is given by

$$\alpha = \gamma B_1 t_p \tag{1.24}$$

where B_1 is the RF amplitude and t_p is the pulse duration. If $\vec{M}$ ends up in transverse plane, the RF pulse is called a 90° pulse. Double the pulse duration or strength, $\vec{M}$ will end up in negative z-axis and the pulse is flip angle is 180°.

1.1.3   Relaxation Time Constants

The last two terms in Bloch equation (1.22) illustrate the relaxation process, that the magnetization $\vec{M}$ return to the equilibrium after it has been disturbed by RF pulses. According to thermodynamics, the system will return back to equilibrium given sufficient time after the external force is removed. In the rotating frame,

$$\begin{cases} \dfrac{dM_{z'}}{dt} = -\dfrac{M_{z'} - M_z^0}{T_1} \\ \dfrac{dM_{x'y'}}{dt} = -\dfrac{M_{x'y'}}{T_2} \end{cases} \tag{1.25}$$

where $M_{z'}$ and $M_{x'y'}$ are the longitudinal and transverse magnetization components, and M_z^0 is the longitudinal magnetization at equilibrium. This is derived from the Bloch equation (1.22), where the first term is dropped since the excitation RF pulse is turned off. T_1 and T_2 are experimental parameters called the 'spin-lattice' and 'spin-spin' relaxation time. Solving Eq. (1.25), we have the time-dependent changes of longitudinal and transverse magnetization com-

Table 1.2: Approximate relaxation times at 1.5T

Tissue	T_1 (ms)	T_2 (ms)
Water/CSF	4000	2000
Gray matter	900	100
White matter	780	90
Muscle	900	50
Fat	250	70
Liver	500	40

ponents:

$$\begin{cases} M_{z'}(t) = M_z^0(1 - e^{-t/T_1}) + M_{z'}(0)e^{-t/T_1} \\ M_{x'y'}(t) = M_{x'y'}(0)e^{-t/T_2} \end{cases} \tag{1.26}$$

where $M_{z'}(0)$ and $M_{x'y'}(0)$ are the longitudinal and transverse magnetization immediately after the excitation RF pulse. Eq. (1.26) indicates that the relaxation process follows an exponential curve, as illustrated in Figure 1.5. Approximate relaxation times of biological tissue are shown in table 1.2

1.2 Signal Detection and Characteristics

With the knowledge of NMR phenomenon, this section discusses how to convert the transverse magnetization into detectable electronic signal. The mathematical expressions and demodulation of the activated signal are described, featuring variables to characterize excitation conditions and the spin system.

1.2.1 Detection Principles

The basic principle of MR signal detection is the Faraday law of electromagnetic induction, which states that magnetic flux through a receiver coil induces a voltage in the coil that is equal to the changing rate of the magnetic flux. The power generators which convert mechanical force into electricity is one of the many examples of the Faraday law in action. As common circumstances, the same RF coil is used for both excitation and detection in MRI scanners. The sensitivity of a receiver coil can be determined by the principle of reciprocity. Assume that $\vec{B}_r(\mathbf{r})$ is the magnetic field at location $\mathbf{r}$ produced by a hypothetical unit current in the coil, then according to the Faraday law of induction and the principle of
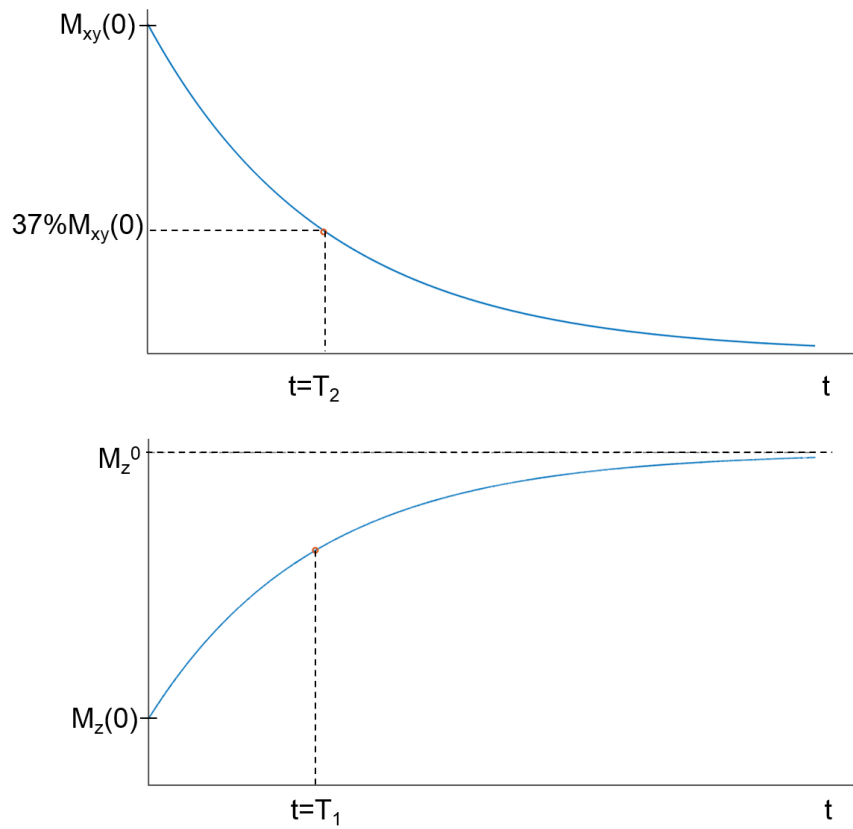
Figure 1.5: Longitudinal (bottom) and transverse (top) relaxation curves. The longitudinal magnetization regains 63% of the thermal equilibrium value M_z^0 when $t = T_1$, and the transverse magnetization loses 63% of the initial value $M_{xy}(0)$ when $t = T_2$.

reciprocity, the voltage $V(t)$ induced in the coil by magnetic flux $\vec{M}(\mathbf{r}, t)$ can be written as

$$V(t) = -\frac{\partial}{\partial t} \int_{coil} \vec{B}_r(\mathbf{r}) \cdot \vec{M}(\mathbf{r}, t)d(\mathbf{r}) \tag{1.27}$$

The voltage $V(t)$ in Eq. (1.27) is considered as the raw NMR signal. The longitudinal component M_z is neglected since it's slow varying compared to transverse components. By combining the free precession equation (1.26), demodulating high-frequency component and assuming a homogeneous main magnetic field and reception field in the region of interest (ROI), the signal detected in the rotating frame of reference is given by

$$S(t) = \int_{ROI} M_{xy}(\mathbf{r}, 0)e^{-t/T_2(\mathbf{r})}e^{-i\omega(\mathbf{r})t}d\mathbf{r} \tag{1.28}$$

where the ω is the resonance frequency in the rotating frame at location $\mathbf{r}$. For heterogeneous spin system with isochromatics, the frequency distribution can be characterized by the spectral density function $\rho(\omega)$. The relationship between bulk magnetization for an isochromatic $dM(\omega)$ and the spectral density function $\rho(\omega)$ is given by

$$dM(\omega) = \rho(\omega)d\omega$$
$$M = \int_{-\infty}^{\infty} \rho(\omega)d\omega \tag{1.29}$$

Therefore, Eq. (1.28) can be rewritten as

$$S(t) = \int_{-\infty}^{\infty} \rho(\omega)e^{-t/T_2(\omega)}e^{-i\omega t}d\omega \tag{1.30}$$

The detailed characteristics of MRI signal are discussed in the following section in three categories: free induction decays (FIDs), gradient echoes and spin echoes.

1.2.2   Free Induction Decays

Free induction decay (FID) is a basic form of transient signal arising from a single pulse excitation on a nuclear spin system. FID signals are generated by the free

precession of the bulk magnetization with decaying amplitude. The FID signal generated by an α pulse takes the form:

$$S(t) = \sin \alpha \int_{-\infty}^{\infty} \rho(\omega) e^{-t/T_2(\omega)} e^{-i\omega t} d\omega \tag{1.31}$$

Apart from flip angle α and relaxation constant T_2, an FID signal is also affected by the spectral density function $\rho(\omega)$. The maximum amplitude of an FID signal occurs at $t = 0$ with value depends on the flip angle and the bulk magnetization at thermal equilibrium:

$$A_f = \sin \alpha \int_{-\infty}^{\infty} \rho(\omega) d\omega = M_z^0 \sin \alpha \tag{1.32}$$

The decay rate of an FID signal is affected by the spectral distribution of the spin system. In a homogeneous spin system with only one resonance frequency ω_0, the FID signal is given by

$$S(t) = M_z^0 \sin \alpha e^{-t/T_2} e^{-i\omega_0 t} \tag{1.33}$$

Eq. (1.33) states that the decay rate of a homogeneous spin system is characterized by T_2. The FID signal decays much faster in an inhomogeneous spin system, described by the effective time constant T_2^*, defined by

$$\frac{1}{T_2^*} = \frac{1}{T_2} + \gamma \Delta B_0 \tag{1.34}$$

In summary, an FID is a transient signal as the response of a spin system to a pulse excitation, described by two parameters: maximum amplitude and decay rate. The maximum amplitude is reached right after the pulse excitation, with a value depends on the flip angle, spin density and the magnetic field strength. The decay rate is characterized by effective time constant T_2^*, which is determined by trasverse relaxation time T_2 and field inhomogeneity.

1.2.3 Spin Echoes

Apart from the FID, echoes are another type of signals widely used in MRI. They have symmetric shape resulting from rephasing and dephasing of the transverse magnetization. Echo signals are created by reversing magnetic field gradient or

multiple RF pulses, therefore are divided into two categories: gradient echoes and RF echoes.

Introduced by by Erwin L. Hahn in 1950 [1], spin echo is the most widely used RF echos in NMR experiments. It consists of a 90°and a 180°pulse separated by a time delay τ. The scheme is denoted as

$$90° - \tau - 180° \tag{1.35}$$

The sequence diagram of spin echo is shown in Figure 1.6. To understand the formation of spin echoes, we consider the effect of RF pulses and evolution of the transverse magnetization in the rotating frame. Assuming that the sample contains one slow precessing isochromat with frequency ω_s and one fast precessing isochromat with frequency ω_f, with negligible off-resonance effects, the 90°excitation pulse rotates both magnetization vectors onto the transverse plane. The vectors begin to precess about the z-axis at different frequencies and gradually lose phase coherence. After the time interval τ, the fast and slow precessing vectors are out of phase by $(\omega_f - \omega_s)\tau$. The 180° refocusing pulse is applied at this time point, tipping magnetization vectors to the opposite side of the transverse plane. Consequently, the fast precessing vector now falls behind by the same phase that it was ahead of prior to the 180° pulse. With continued precession, the fast vector will catch up with the slower one after the time interval τ. Therefore, the magnetization vectors regain phase coherence at $t = 2\tau$, creating an echo.

In Figure 1.6, the FID created by the 90°excitation pulse decays with T_2^*. The echo is produced at Echo Time (TE), $TE = 2\tau$. The maximum amplitude of the FID and the echo follows a T_2 decay curve.

1.2.4 Gradient Echoes

Gradient echo is another type of widely used NMR signal, created by time-varying magnetic gradient fields. A magnetic field gradient is a inhomogeneous with field strength (z-component) varied linearly along a specific direction. A field gradient $\vec{B}_G$ is called x-gradient when
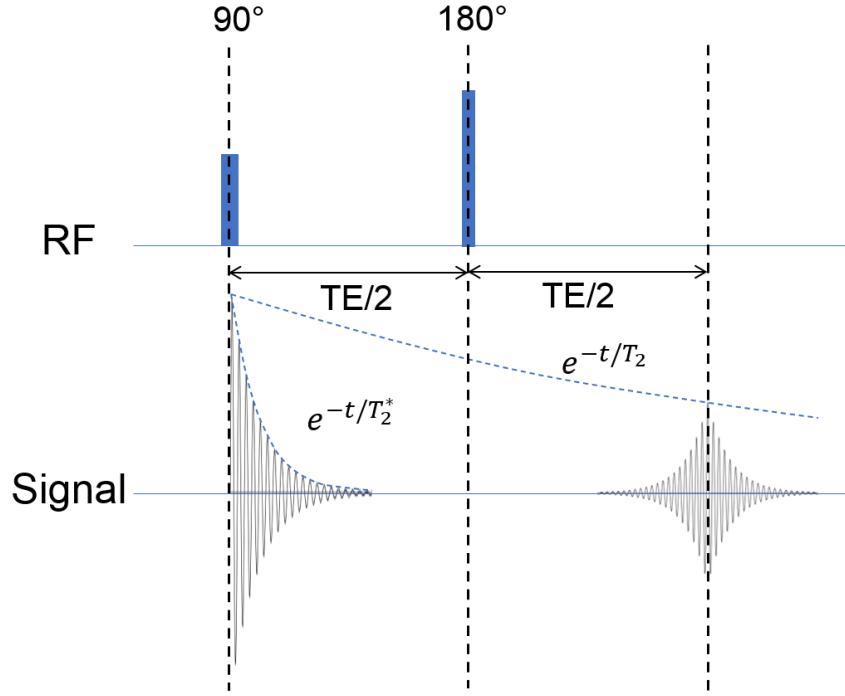
$$B_{G,z} = G_x x \tag{1.36}$$

Figure 1.6: Formation of spin echos. The 90°excitation pulse and 180° refocusing pulse are applied successively, creating an echo at TE.

Similarly, a y- or z-gradient has field strength varied linearly along y or z direction. In MRI scanners, the gradient system consists of x-, y- and z-gradient coils. The combination of theses three coils can produce field gradients along any arbitrary directions.

$$B_{G,z} = G_x x + G_y y + G_z z \tag{1.37}$$

The gradient vector $\vec{G}$ can be expressed using the three component together

$$\vec{G} = (G_x, G_y, G_z) = G_x \vec{i} + G_y \vec{j} + G_z \vec{k} \tag{1.38}$$

Where $\vec{G}$ is the gradient direction of $\vec{B}_G$. Note that regardless of field gradients, the magnetic field is always along the z-direction. The overall magnetic field can be expressed as

$$\vec{B} = (B_0 + B_{G,z})\vec{k} \tag{1.39}$$

The pulse sequence of gradient echo is shown in Figure 1.7. A small flip angle excitation pulse is often applied to achieve fast imaging. The subsequent FID decays rapidly with the dephasing gradient. Assume the dephasing gradi-
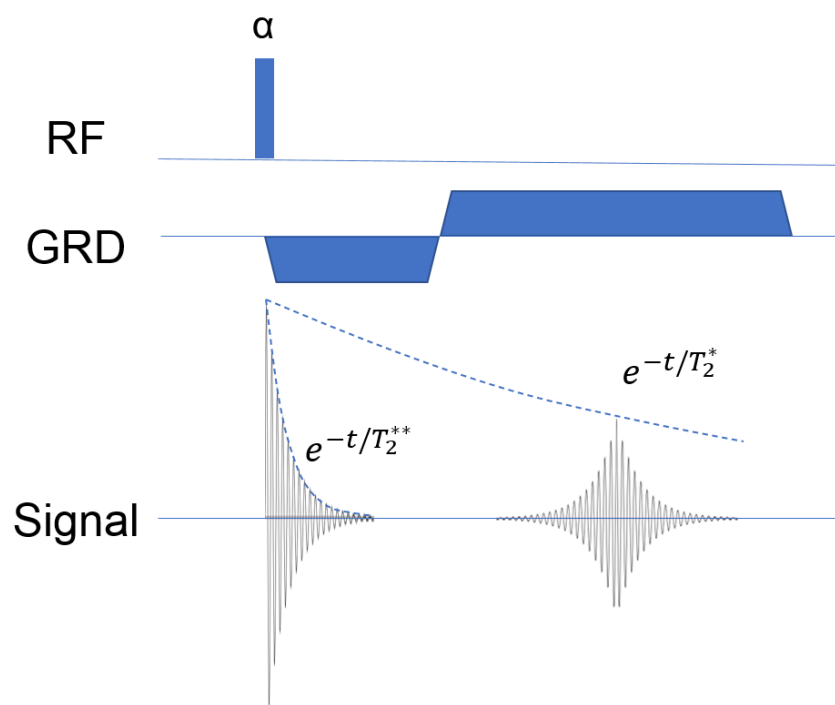
Figure 1.7: Formation of gradient echoes. After an α-degree excitation pulse, the FID decays rapidly with T_2^{**} as spins are dephased by the negative gradient, which are rephased by the subsequent positive gradient.

ent is applied along the negative x-direction, spins will acquire different phase depending on their x-positions

$$\phi(x,t) = \gamma \int_0^t -G_x x d\hat{t} = -\gamma G_x x t \qquad 0 \leq t \leq \tau \qquad (1.40)$$

Eq. (1.40) indicates that the amount of phase incoherence increases with time during the application of the dephasing gradient. The FID after the α-degree excitation pulse decays with another time constant T_2^{**}, which is more rapid than T_2^* decay. When a rephasing gradient is applied with opposite polarity to the dephasing gradient, spins gradually regain phase coherence and leads to signal regrowth. The spin phase during rephasing gradien is given by

$$\phi(x,t) = -\gamma G_x x \tau + \gamma \int_\tau^t G_x x d\hat{t} \qquad (1.41)$$

$$= -\gamma G_x x \tau + \gamma G_x x (t - \tau) \quad \tau \leq t \leq 2\tau \qquad (1.42)$$

Therefore, in case that the dephasing and rephasing gradient have the same strength, an echo is formed at $t = 2\tau$. The maximum amplitude of the FID and the echo follows a T_2^* decay curve instead of T_2.

1.3 Image Formation and Reconstruction

The previous section described how to activate and detect MR signal. However, the signal acquired is the sum of signal from all the protons in the imaged object. To generate the final image, we need to encode the signal with its spatial origin. In MRI, spatial encoding is achieved with imaging gradients. In 1973, Paul Lauterbur proposed zeugmatography, by combining magnetic field gradient with image reconstruction from projections. Selective excitation was proposed by Sir Peter Mansfield in 1974. They shared the Nobel Prize in 2003 "for their discoveries concerning magnetic resonance imaging". In this section, we focus on the spatial localization of MR signal.
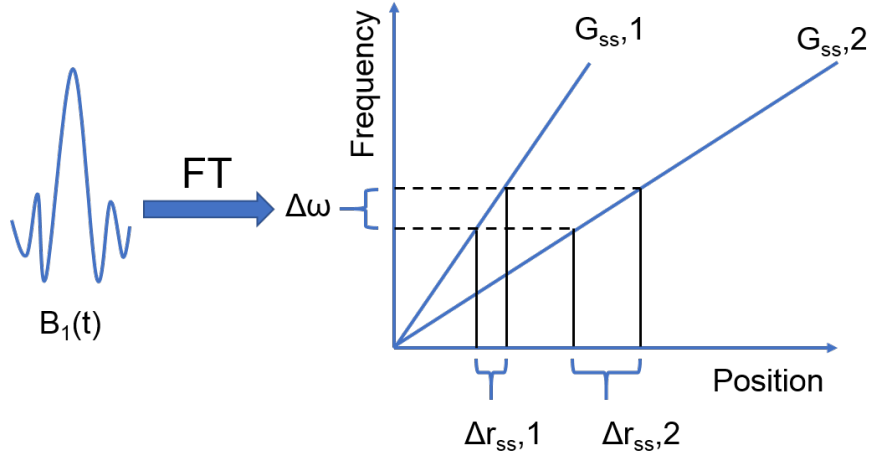
Figure 1.8: Demonstration of slice selective gradient strengths mapping the same RF pulse to different slice thicknesses. The RF pulse with bandwidth of $\Delta\omega$ selectively excites $\Delta r_{ss}, 1$ in presence of $G_{ss}, 1$, and $\Delta r_{ss}, 2$ in presence of $G_{ss}, 2$.

1.3.1 Selective Excitation

Two components are essential in slice selection: linear magnetic field gradient and shaped RF excitation. In MRI, the linear gradient refers to the spatial variation of filed strength along the z direction, same as the main magnetic field B_0. Modern MRI scanners are equipped with gradient coils mounted inside the magnet, to generate gradients oriented in three orthogonal directions, whose shape and amplitude can be adjusted. The field strength with after applying gradient can be described as $\vec{B} = (B_0 + G_x X + G_y Y + G_z Z)\vec{k}$.

For distinction, we use G_x, G_y, and G_z to denote the gradient strength in three physical axes, and G_{fe}, G_{pe} and G_{ss} to denote the the gradient strength in logical axes, also known as frequency encoding, phase encoding, and slice selection respectively. Each physical axis has its own dedicated gradient coil and amplifier, and the gradient waveform on logical coordinate is transformed to the physical coordinate by a rotation matrix based on the operator's prescription. Slices oriented in arbitrary directions can be produced by a linear combination of gradients in three physical directions with gradient strength $G_{ss} = \sqrt{G_x^2 + G_y^2 + G_z^2}$.

Therefore, slice selection can be achieved by playing out the constant gradient and the frequency-selective RF excitation simultaneously, as shown in Figure 1.8. As described in Eq. (1.8), the Larmor frequency of precession is proportional to the magnetic field strength, which can be described after applying slice selective

gradient as:

$$\omega_0 = \gamma(B_0 + \vec{G}_{ss} \cdot \vec{r}_{ss}) \tag{1.43}$$

Where the $\vec{G}_{ss}$ and $\vec{r}_{ss}$ are the vectors for the slice selection gradient and the displacement from the gradient isocenter. From Eq. (1.43), we can see that only the displacement along the direction of $\vec{G}_{ss}$ will affect resonance frequency. The constant gradient will make the resonance frequency vary linearly along the slice selective direction, translating the frequency selectivity of RF pulse into the desired location of spin excitation, as shown in Figure 1.8. With a given RF bandwidth, thinner slices can be achieved by stronger slice selection gradient. If the RF bandwidth is $\Delta\omega$, then we have the slice thickness Δr_{ss}

$$\Delta\omega = \gamma\vec{G}_{ss} \cdot \Delta\vec{r}_{ss}$$
$$\Delta r_{ss} = \frac{\Delta\omega}{\gamma G_{ss}} \tag{1.44}$$

The slice selective RF pulse is amplitude-modulated by the envelop function $B_1^e(t)$ and has a carrier frequency w_{rf}. These two parameters determine the excitation properties of the pulse. Commonly used selective RF excitation pulses include SINC pulses and Shinnar-Le Roux (SLR) pulses [2]. The Fourier transform is the simplest way of designing selective RF pulses. Briefly, the RF pulse envelop function is given by the Fourier transform of the slice selection profile.

After the selective RF excitation, there will be a phase dispersion because of a linear phase shift introduced by the selective gradient across the slice thickness. A slice refocusing gradient is used in conjunction with the slice selective gradient and has opposite polarity, to compensate for the phase dispersion and avoid unwanted signal loss. The area of the slice refocusing gradient is calculated by the isodelay of the RF pulse, which generally equal to the amount of time from the peak of the RF pulse to the end of it. That is because the transverse magnetization is formed at the isocenter, and the dephasing occurs afterwards until the end of the RF pulse. As shown in Figure 1.9, the area of slice refocusing gradient should be equal to the area of slice selective gradient after isocenter point.

Another practical consideration is the RF Pulse truncation effect. The frequency profile of the RF pulse can be approximated by the Fourier transform of the envelope, therefore determine the slice profile. In order to achieve an ideal rectangular slice profile, the SINC pulse should be infinitely long. In practice, the implemented SINC pulses have finite duration by truncating the side lobes,
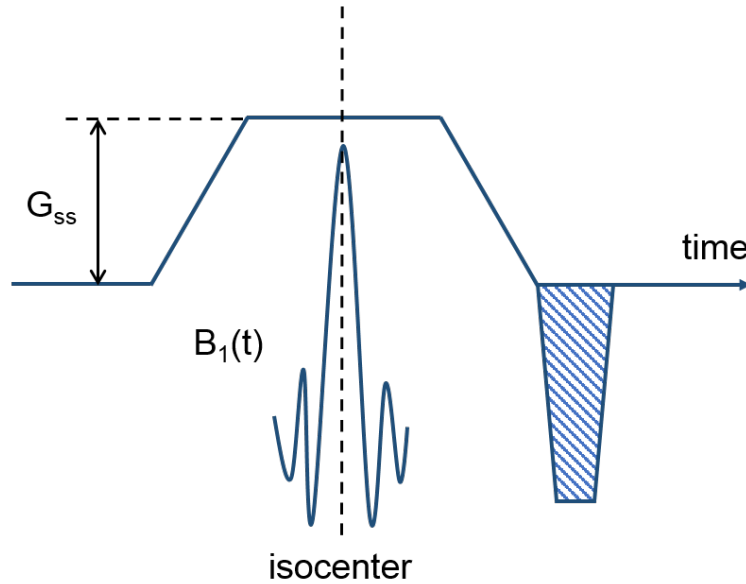
Figure 1.9: Demonstration of slice refocusing gradient (stripped ares) applied after the slice selective gradient. The area of the refocusing gradient is equal to the area of the selective gradient after RF isocenter.

making the actual slice profile deviate from the ideal one. Including more side lobes into the pulse result in a better approximation of the ideal slice profile, but at the cost of increasing the sensitivity to flow and off-resonance effect, and prolonging minimum TE and TR.

1.3.2   Spatial encoding and k-space

During the data acquisition period, spatial information can be encoded into the MR signal with a complex exponential form via two ways: frequency and phase encoding. The rather complicated spatial encoding schemes can be described clearly by the k-space notation and the Fourier transform. As implied by its name, the frequency encoding gradient makes the oscillating frequency of the detected MR signal dependent on its location along the encoding direction. For simplicity, we consider the case that the frequency encoding gradient is applied along the x direction for a one-dimensional object with spin density of $\rho(x)$. The spin at location x experiences a homogeneous B_0 field, in addition to a linear gradient field G_x. Therefore, the Larmor frequency can be written as:

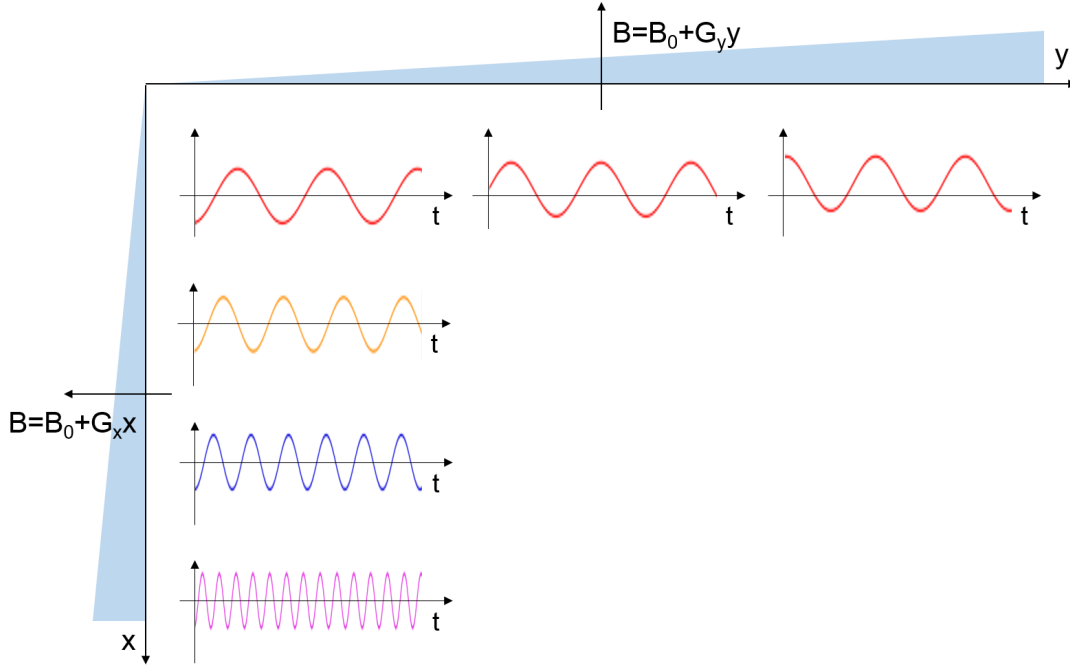$$\omega(x) = \omega_0 + \gamma G_x x \tag{1.45}$$

Figure 1.10: Illustration of spatial encoding. Assuming that the frequency encoding is applied along the x direction and phase encoding along the y direction. Local signals bears frequency and initial phase linearly related to its location on frequency or phase encoding directions.

When neglecting transverse relaxation effect, the signal from a infinitesimal sample at location x can be written as:

$$dS(x,t) \propto \rho(x)e^{-i\gamma(B_0+G_x x)t}dx$$
$$\propto \rho(x)e^{-i\omega(x)t}dx \qquad (1.46)$$

The signal from Eq. (1.46) is frequency encoded as it has the position-dependent frequency $\omega(x) = \gamma(B_0 + G_x x)$ in its expression. For two-dimensional objects, frequency encoding is not enough since only position along one direction can be defined.

To illustrate the idea of phase encoding, we again consider a simplified case that the phase encoding gradient G_y is applied along the y direction for a one-dimensional object with spin density of $\rho(y)$. The phase encoding gradients are turned on after the excitation RF pulse for a short period T_{PE}. Neglecting scaling

constant, the local signal can be written as Eq. (1.47):

$$dS(y,t) = \begin{cases} \rho(y)e^{-i\gamma(B_0+G_y y)t}dy & 0 \leq t \leq T_{PE} \\ \rho(y)e^{-i\gamma G_y y T_{PE}}e^{-i\gamma B_0 t}dy & T_{PE} \leq t \end{cases} \qquad (1.47)$$

After the phase encoding gradient G_y is turned off, the local signal has accumulated a phase that is linearly dependent on the position

$$\phi(y) = -\gamma G_y y T_{PE} \qquad (1.48)$$

Since the local signal bears an initial phase related to its location, therefore the signal is phase-encoded. The idea of frequency and phase encoding is illustrated in Figure 1.10.

The popular K-space notation establishes a connection between spatial encoding and the Fourier transform. Using the expression of local frequency encoded signal in Eq. (1.46), we have the demodulated signal from the entire object:

$$S(t) = \int_{-\infty}^{\infty} \rho(x)e^{-i\gamma G_x x t}dx \qquad (1.49)$$

substituting a variable $k_x = \gamma G_x t/2\pi$, we have

$$S(k_x) = \int_{-\infty}^{\infty} \rho(x)e^{-i2\pi k_x x}dx \qquad (1.50)$$

Therefore, the time signal $S(t)$ is mapped to k-space signal $S(k_x)$ by frequency-encoding gradient G_x. Similarly, using $k_y = \gamma G_y T_{PE}/2\pi$, we can rewrite the phase encoded signal in Eq. (1.48) to $\phi(y) = -2\pi k_y y$. Note that for each step in phase encoding, k_y has a fixed value. In frequency encoding, k_x is always a function of time. Therefore, phase encoding determines the starting point whereas frequency encoding determines the shape of the k-space trajectories of the evolving signal. Compared to an FID signal, an echo signal has symmetric shape which is also reflected in the k-space coverage, as compare in Figure 1.11. Commonly used k-space coverage and their corresponding pulse sequences are shown in Figure 1.12 [3].
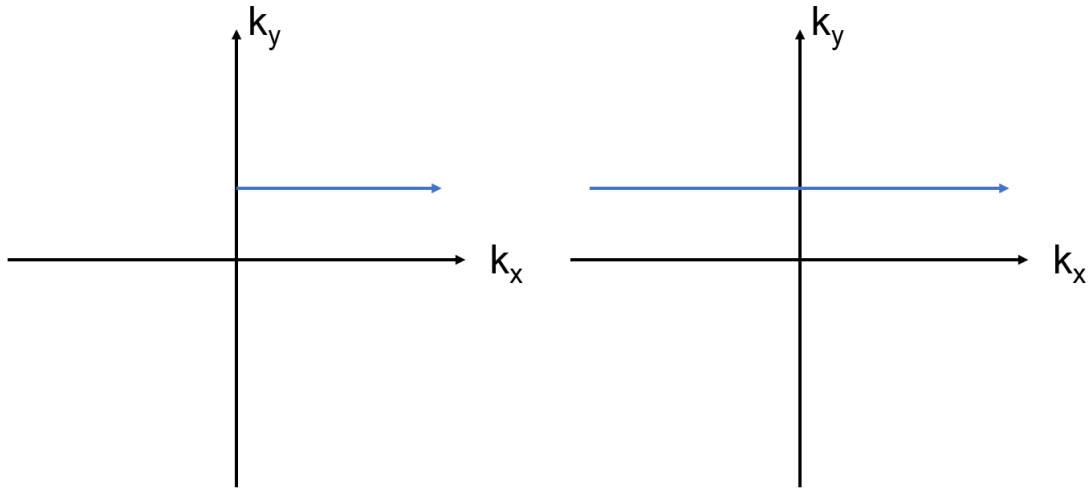
Figure 1.11: K-space sampling trajectories of a FID (left) and an echo (right) signal. The echo signal has symmetric coverage in k-space.
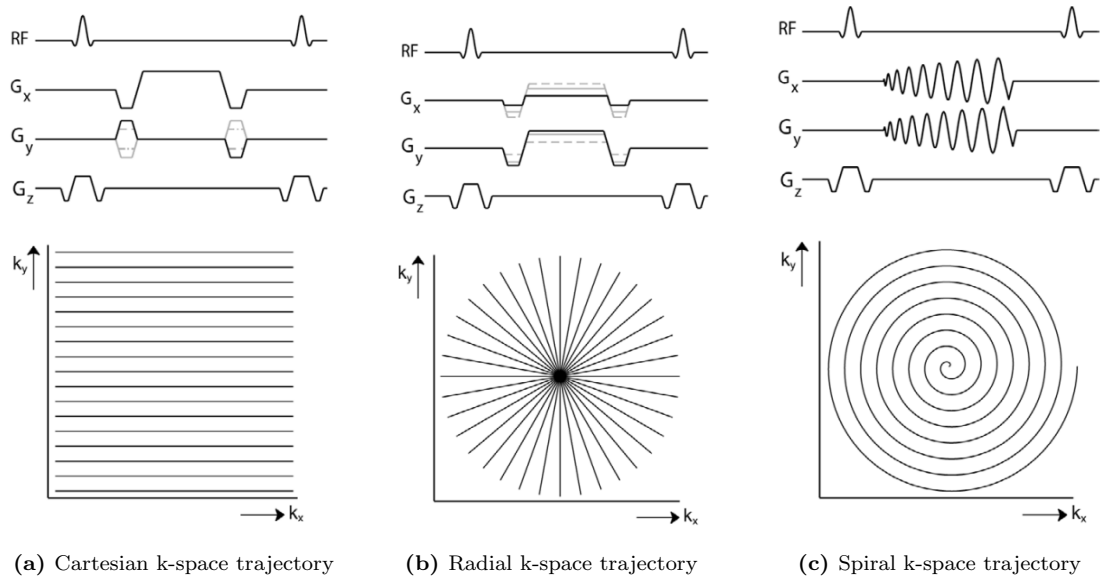

(a) Cartesian k-space trajectory **(b)** Radial k-space trajectory **(c)** Spiral k-space trajectory

Figure 1.12: Cartesian, radial, and spiral k-space sampling trajectories (bottom) and their corresponding pulse sequences (top) [3].

1.3.3 Reconstruction by Fourier Transform

The previous section described how to encode spatial information into during data acquisition. Using I to represent the image function and S as measured signal, their relationship follows the imaging equation:

$$S = f(I) \tag{1.51}$$

where f represents the spatial information encoding scheme. The aim of image reconstruction is to convert information from the measured signal into the image function. In theory, the image function I can be obtained by inverse transform when f is invertible, $I = f^{-1}(S)$. However in most cases, the inverse function f^{-1} cannot be computed as data sampling is discrete. Recall the definition of k-space data in Eq. (1.50), it corresponds to the Fourier transform (FT) of transverse magnetization. Therefore in MRI, f is the Fourier transform operator. The reconstruction problem can be formulated as:

$$\text{Given} \quad S(k_n) = \int_{-\infty}^{\infty} I(\mathbf{r})e^{-i2\pi k_n \mathbf{r}}d\mathbf{r} \tag{1.52}$$

$$\text{determine} \quad I(\mathbf{r})$$

Consequently, MRI reconstruction requires a 2D or 3D inverse Fourier transform (IFT). When the k-space data sampling is discrete, finite and uniform along the Cartesian trajectory as in Figure 1.12a, image reconstruction can be achieved using the discrete Fourier transform (DFT) For simplicity, consider only the one-dimensional case along the x direction, the reconstruction formula can be written as:

$$I(x) = \Delta k \sum_{n=-N/2}^{N/2-1} S[n]e^{i2\pi n \Delta k x} \qquad |x| < \frac{1}{\Delta k} \tag{1.53}$$

where the signal $S[n]$ is collected at k-space points

$$n\Delta k, -N/2 \leq n < N/2 \tag{1.54}$$

To avoid aliasing, the sampling interval has to satisfy the Nyquist criteria. The DFT is computationally cumbersome, but can be efficiently implemented by a series of fast Fourier transforms (FFTs). The relationship between image pixel

size Δx, sampling interval Δk and field of view (FOV) is given by

$$\Delta x = \frac{FOV}{N} = \frac{1}{N \Delta k} \tag{1.55}$$

When The k-space data is sampled in other trajectories instead of Cartesian, such as spiral or radial trajectories shown in Figure 1.12b and 1.12c, the data needs to be resampled into the Cartesian grid, known as regridding.

Chapter 2

Diffusion Weighted Echo Planar Imaging with Sinusoidal Gradient

2.1   Introduction

Diffusion weighted EPI

Echo planar imaging (EPI) is a ultra-fast MRI pulse sequences first introduced by Mansfield [4], which employs a series of bipolar readout gradients to generate consecutive echoes. With corresponding phase encoding gradients, multiple k-space lines or the entire image can be sampled after a single excitation pulse. The vast majority of EPI applications use 2D single-shot sequences to acquire a snapshot image within a second. Despite drawbacks of low resolution and susceptibility artifact, the ultra-fast imaging speed of EPI makes it optimum choice to a number of challenging MR applications, such as diffusion and perfusion imaging, neuro-functional imaging and other dynamic or real-time imaging. Given the challenges of bulk motion sensitivity, most diffusion imaging techniques are based on single-shot EPI. In addition, when multiple diffusion directions and b-values need to be acquired, single-shot EPI can reduce the scanning time to be acceptable in clinics.

Compared to more conventional sequences, EPI utilizes fast and heavy gradient switching in readout, which is very demanding on gradient hardware, and generates high level of acoustic noise especially in high field strength. When ac-

companied with diffusion gradients, the sound pressure levels (SPL) is beyond the sufferance of human ears, causing temporary or even permanent hearing damage [5].

Acoustic noise reduction

As a consequence of mechanical vibrations of gradient coils, the acoustic noise response $S(f)$ is dependent on two factors: the inherent acoustic frequency response function of gradient coils $H(f)$ and the sound spectrum of the sequence $G(f)$.

$$S(f) = G(f) \cdot H(f) \tag{2.1}$$

The frequency response function is mostly determined by hardware settings, including gradient coil assembly and field strength. Several hardware-based acoustic noise reduction approaches have been proposed, such as the use of sound-attenuating materials, Lorentz force balancing [6], rotating DC gradient[7] and active vibration control [8]. The sound spectrum of the sequence depends on software factors, such as gradient shape and amplitude, slew rate and readout (RO) bandwidth. Software-based approaches can effectively reduce acoustic noise by adapting the sound spectrum of the sequence to the frequency response function of the scanner. This can be achieved without costly hardware modification, and can be incorporated into any existing MRI system. Generally, it is a trade-off between noise reduction and scan efficiency. Decreased gradient amplitude and slew rate contributes to noise reduction at the cost of prolonged acquisition time. A number of studies [9, 5] have developed quiet version of standard MRI sequences by using smoothed gradient switching to achieve a low-pass filtering effect on the acoustic spectral envelope.

Pulse sequence programming

MRI pulse sequences were developed using EPIC, which stands for ***E****nvironment for **P**ulse programming **I**n **C***. A pulse sequence consists of linear orthogonal gradients in X, Y and Z directions, RF excitation and data acquisition that generates MR data. An EPIC program is called a Pulse Sequence Databases (PSDs), which are developed offline and can be executed on MR scanners to generate the prescribed sequence by controlling system hardware. Essentially, EPIC is a Software Development Kit for programming MR scanners. It's a collection of subroutines
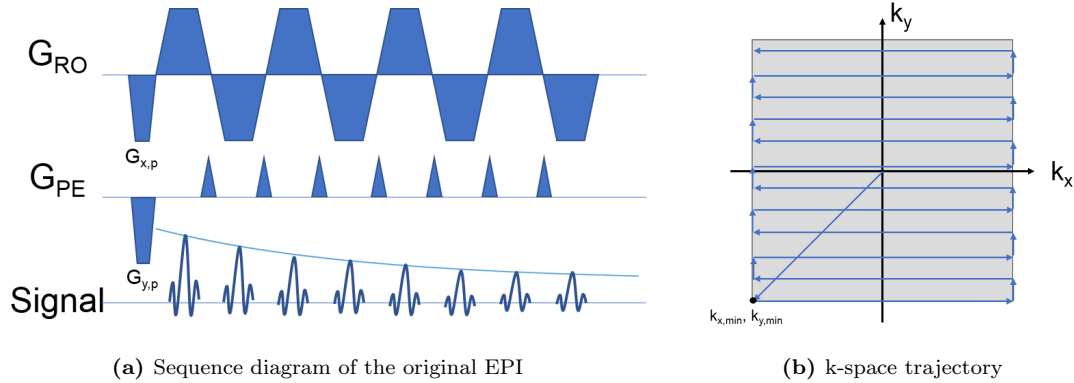
(a) Sequence diagram of the original EPI

(b) k-space trajectory

Figure 2.1: The EPI sequence with rectilinear k-space trajectory

and macro definitions. Basic imaging sequences are starting points for sequence developers, such as spin echo, spoiled and unspoiled gradient echo sequences. The main structure of an EPIC source file is similar for any pulse sequences, which consists of host and target routines. Host routines perform variable initialization and calculations, update prescription inputs from the advisory panel, and checks for allowed combinations of variable values and boundary conditions. Target routines load the hardware sequencer memory with data to allow it play out the pulse sequence, and makes modifications to the sequences during run-time.

Two important concepts in EPIC programming are macros and control variables (CVs). Macros are predefined in header files to declare and initialize host and target variables, create RF and Gradient waveforms and the corresponding instruction to control hardware devices. They have been employed to simplify pulse programming, by achieving tasks in one line of code which takes many lines in C. A good example would be the 'TRAPEZOID' macro, which generates a trapezoid waveform with defined start time, area and the flat portion of the trapezoid. CVs are enhanced global variables used to communicate between the scan, host and target PSD processes. Scan parameters such as TE, TR, FOV can be transmitted to the PSD via corresponding CVs at the time of the prescription. Dependent pulse sequence information such as pulse widths and amplitudes can be transferred to the target process. Some of them can also control image database and reconstruction.
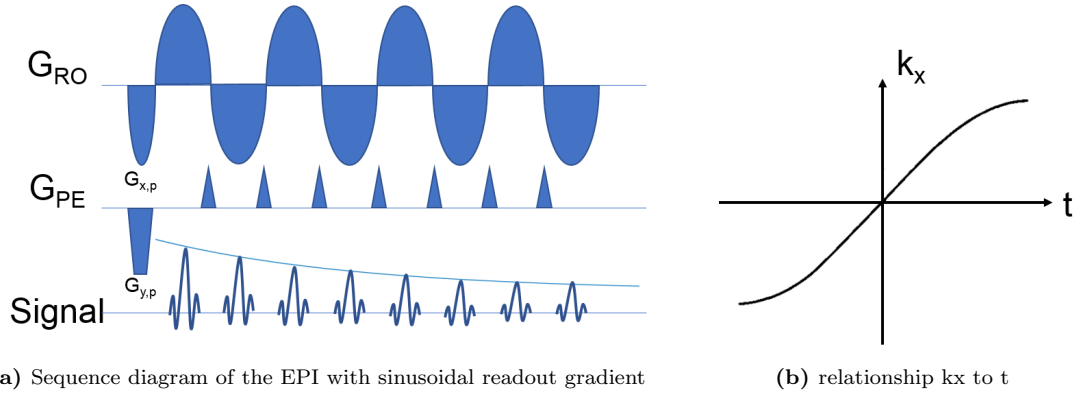
(a) Sequence diagram of the EPI with sinusoidal readout gradient

(b) relationship kx to t

Figure 2.2: the EPI sequence with sinusoidal readout gradient

2.2 Methods

2.2.1 Sequence Implementation

The sequence diagram for the original EPI and its rectilinear k-space trajectory are shown in Figure 2.1. It makes the maximal uses of the transverse magnetization of a single RF excitation by generating a series of gradient echoes using bipolar readout gradients pared with blipped phase encoding gradients. The phase encoding gradients have a constant area and are stepped incrementally, encoding each echo into a orthogonal k-space line. The direction of the k-space lines alternates in line with the readout gradient, which normally consists of a train of identical gradient lobes with alternating polarity. The prephasing gradients $G_{x,p}$ and $G_{y,p}$ moves the initial sampling point from k-space center to the $k_{x,min}, k_{y,min}$ to get full k-space coverage. The number of readout echoes generated by each RF excitation is called the echo train length (ETL), denoted as N_{ETL}. The echoes are evenly spaced and the time interval between consecutive echoes is called the echo spacing (ESP), denoted as t_{ESP}. The main frequency is calculated as $1/2t_{ESP}$

Since the first introduction of EPI in 1977, a number of its variants have been developed. Figure 2.2a shows a common EPI variant with sinusoidal readout gradients, described by $G_x(t) = G_x \cos(2\pi\Omega t)$, and a prephasing gradient of area $-G_x/(2\pi\Omega)$. In acquisition window, the progress of k-space variable k_x with time can be written as:

$$k_x(t) = \frac{\gamma G_x}{4\pi^2\Omega} \sin 2\pi\Omega t \tag{2.2}$$

(a) Sequence diagram of the EPI with constant phase encoding
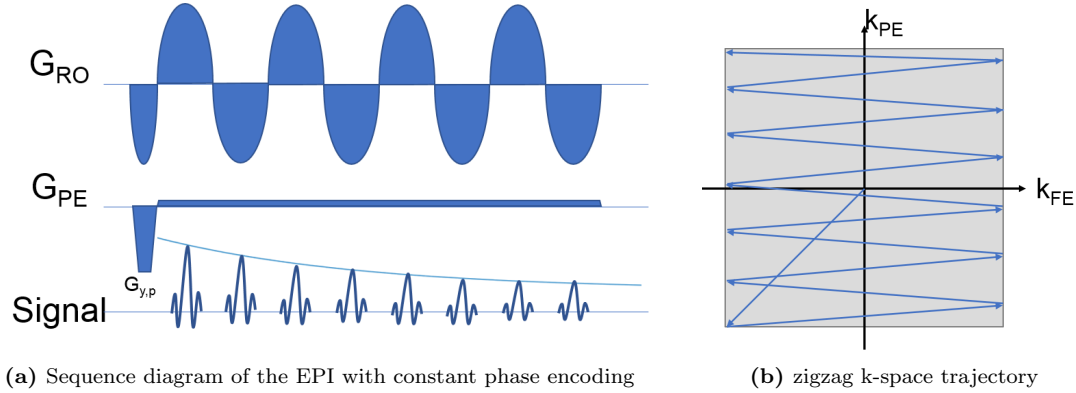

(b) zigzag k-space trajectory

**Figure 2.3:** the EPI sequence with zigzag trajectory

Therefore, the k-space sampling is nonlinear with respect to time t and need to be interpolated to an equidistant grid along the readout direction. Same as the original EPI, phase encoding is conducted by a series gradient blips G_y with identical area and the same polarity, typically with triangular shape. Each blip is played out before the echo acquisition, corresponding to the progress of k-space step in k_y direction.

Another EPI variant has a small constant phase encoding gradient, thus each echo generated by the alternating readout gradient corresponds to a tilted k-space line, forming a zigzag trajectory, as shown in Figure 2.3. The two EPI variants described above were implemented and validated on a 3T MR750w system (GE Healthcare, WI, USA), the gradient waveform recorded on scanner was shown in Figure 2.4. Echo spacing t_{ESP} can be controlled by a variable in user interface for convenient testing.

2.2.2   Image Acquisition and Reconstruction

Data acquisition was conducted on a GE 3T MR750w scanner (GE Healthcare, Waukesha, WI) with a 12-channel GEM head array coil. Spherical water phantom was used to compare the following sequences: product EPI sequence, sinusoidal readout EPI sequence with blipped or constant phase encoding. B value were set to 1000 s/mm^2 for all sequences, echo spacing (ESP) were adjusted from 548 us to 1328 us to investigate its influence on acoustic noise level.

Reconstruction was conducted in MATLAB (The MathWorks, Inc., Natick, USA) using raw k-space data. K-space trajectories of the three sequence are
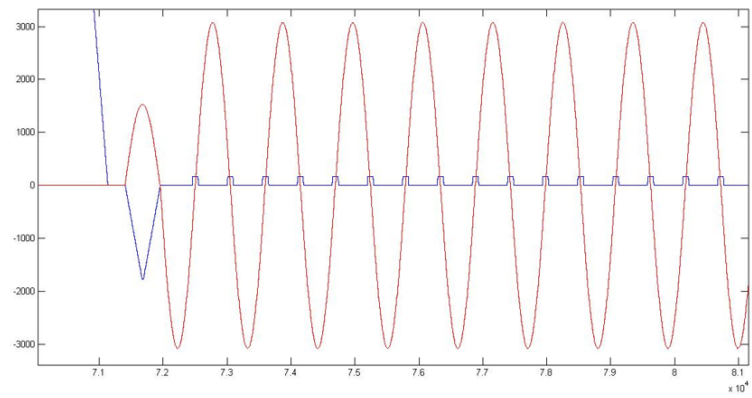
(a) blipped phase encoding (blue) and sinusoidal readout (red)
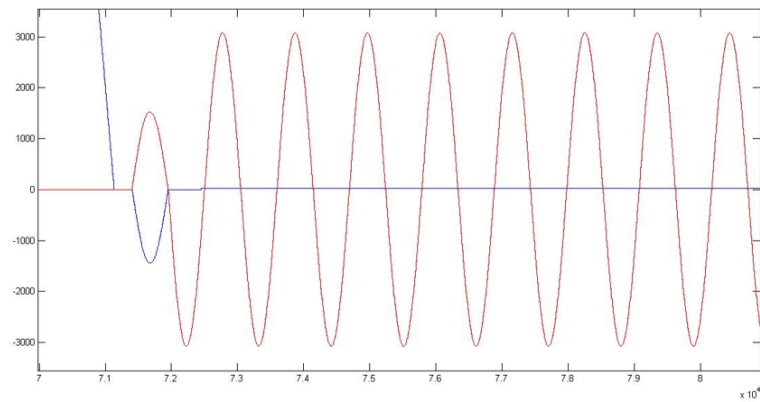
(b) constant phase encoding (blue) and sinusoidal readout (red)

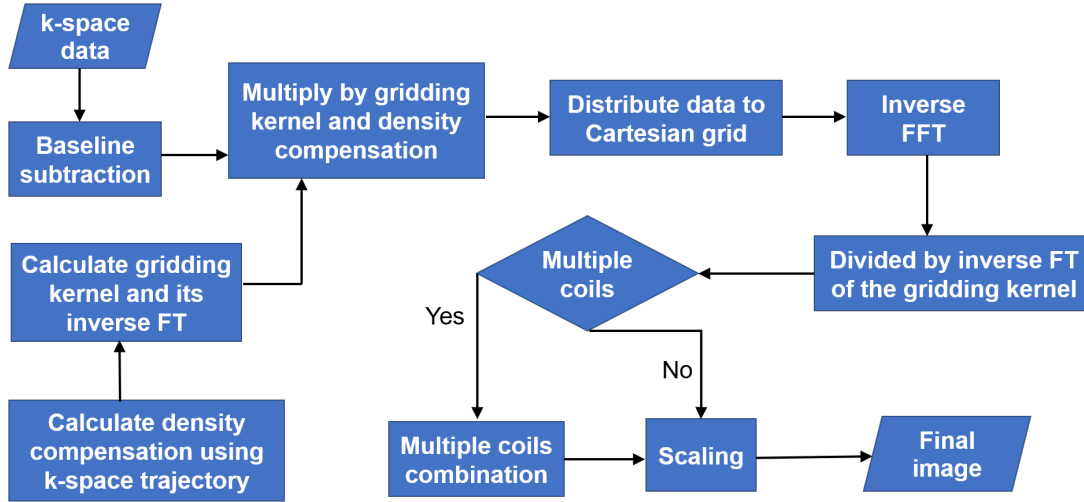**Figure 2.4:** the EPI sequence waveform on plotter

Figure 2.5: Flowchart of gridding reconstruction process

shown in Figure 2.1, 2.2 and 2.3. For the non-Cartesian trajectories in Figure 2.2 and 2.3, gridding reconstruction is used as shown in the flowchart in Figure 2.5. In brief, data are resampled onto the Cartesian grid to enable FFT reconstruction. To avoid artifacts from straightforward interpolation, convolution-based gridding is commonly utilized in MRI as an efficient reconstruction method to produce adequate image quality. First, the k-space data was convolved with a gridding kernel, as in the current study, the Kaiser-Bessel function. The inverse FT of the Kaiser-Bessel function was calculated. The density compensation The gridding matrix and reconstruction result for sinusoidal readout EPI are shown in Figure 2.6.

2.2.3 Acoustic Noise Measurement

Acoustic noise was measured using a Bruel&Kjaer Type 2250 sound level meter with MR compatible type 4189 microphone. The sound level meter was calibrated before the measurement using a 94dB and 114dB sound source. The testing was conducted with the microphone placed at the approximate location of the patient's right ear. RF was disabled during the test to prevent damage to the microphone and RF power has no measurable impact on SPL. The acoustic noise was measured in 1 minutes' duration for the in-bore ambient background, product EPI sequence with b value=1000 s/mm^2, sinusoidal EPI sequence with blipped phase encoding and constant encoding, b value=1000 s/mm^2. A-weighted aver-
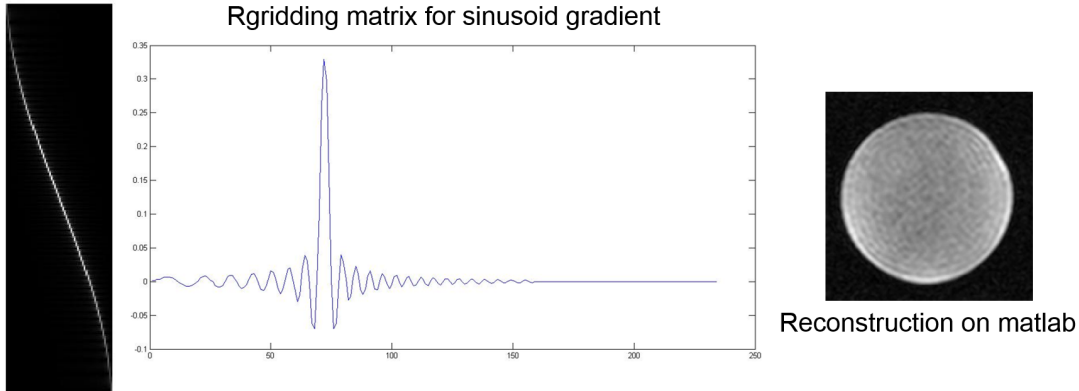
Figure 2.6: Reconstruction with sinusoidal readout gradient

age (LAeq, dBA) and C-weighted peak (LCpeak, dBC) were recorded.

2.3   Results

The comparison of SPL for product EPI sequence and sinusoidal readout gradient EPI sequence with blipped phase encoding are shown in Figure 2.7. Echo spacing (ESP) were adjusted from 548 us to 1328 us. SPL measurement for product EPI sequence ranged from 93.8 dBA to 98.1 dBA for A-weighted average, 113.8 dBC to 116.7 dBC for C-weighted peak. SPL measurement for EPI sequence with blipped phase encoding ranged from 92.2 dBA to 97.6 dBA for A-weighted average, 110.8 dBC to 114.0 dBC for C-weighted peak. The comparison of measured SPL for product EPI sequence and sinusoidal EPI sequence with constant phase encoding are shown in Figure 2.8. SPL measurement for EPI sequence with constant phase encoding ranged from 92.0 dBA to 96.9 dBA for A-weighted average, 110.6 dBC to 114.0 dBC for C-weighted peak. The comparison of measured acoustic noise level for sinusoidal EPI sequence with blipped and constant phase encoding are shown in Figure 2.9. SPL levels showed nearly no difference for these two sequences.

The average noise reduction when using sinusoidal EPI sequence with blipped phase encoding was 1.1±0.39 dBA, 2.4±0.75 dBC. The average noise reduction when using sinusoidal EPI sequence with constant phase encoding was 1.3±0.38 dBA, 2.5±0.70 dBC. The A-weighted average SPL for the three sequences reached minimum when echo spacing is 908 us, the C-weighted peak SPL reached minimum when echo spacing is 1088 us.
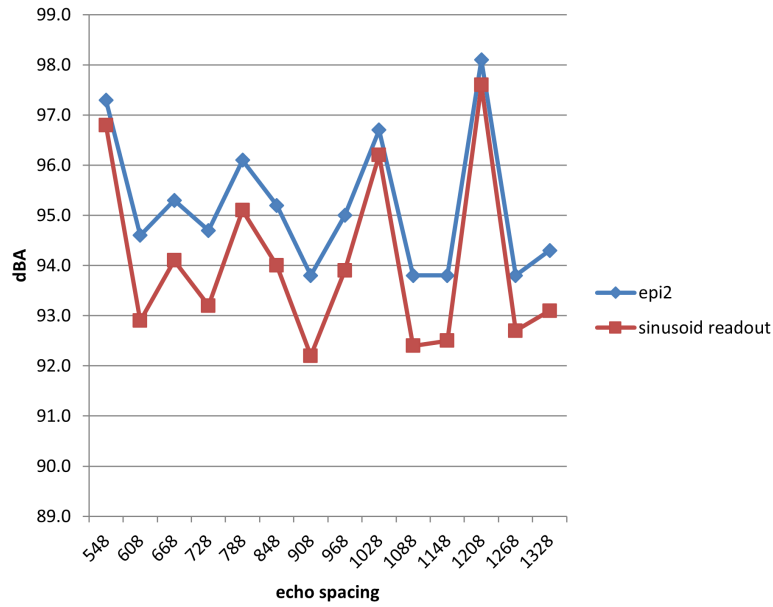
(a) comparing product sequence and sinusoid readout with b=1000, LAeq
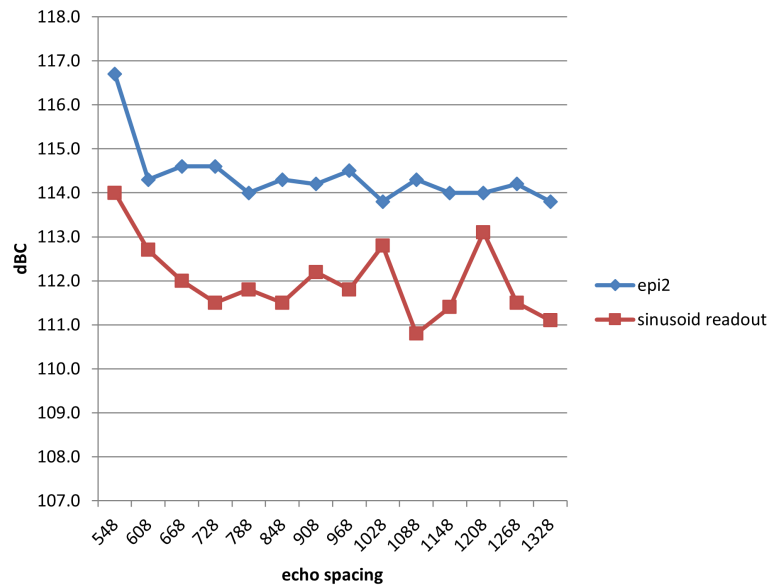
(b) comparing product sequence and sinusoid readout with b=1000, LCpeak

Figure 2.7: comparing product sequence and sinusoid readout with b=1000
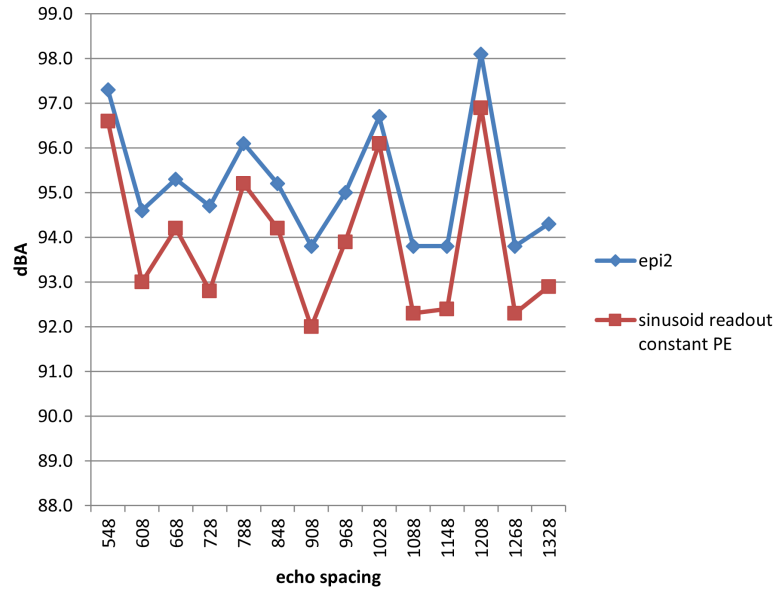
(a) comparing product sequence and sinusoidal readout plus constant phase encoding with b=1000, LAeq
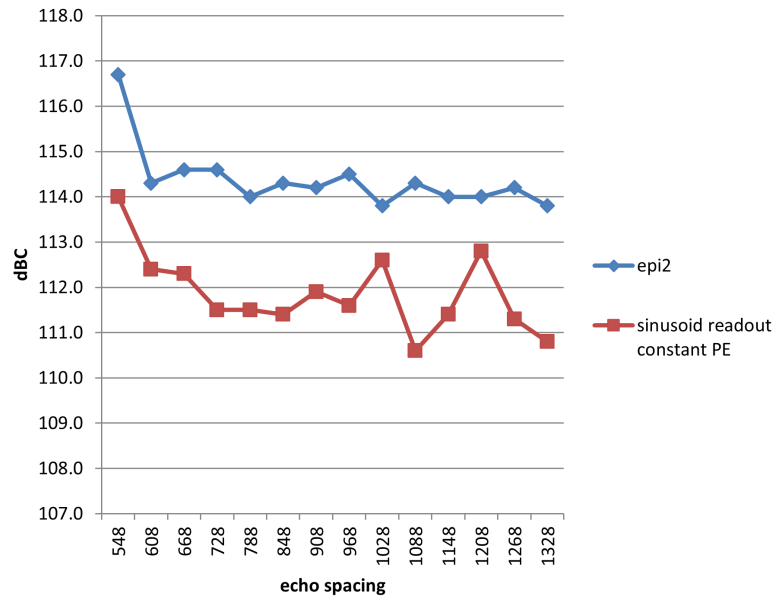
(b) comparing product sequence and sinusoidal readout plus constant phase encoding with b=1000, LCpeak

Figure 2.8: comparing product sequence and sinusoidal readout plus constant phase encoding with b=1000

2.4 Discussion

EPI sequences generally make use of the maximum gradient capacity, leading to high level of acoustic noise. Using smaller gradient amplitudes and slew rate can reduce acoustic noise at the cost of prolonged scanning time and increased image distortion or blurring. The current study aims to investigate the effect of using sinusoidal readout gradient and constant phase encoding, as well as switching main frequency of the sequence to reduce acoustic noise. The sound pressure levels are recorded for comparison in terms of A-weighted average (LAeq) and C-weighted peak (LCpeak). Phantom experiments were conducted to validate the method, the relationship between echo spacing and acoustic noise level was investigated.

The acoustic noise in MRI scanner is generated by the gradient system. During MRI examinations, the amplitude and polarity of imaging gradients are switched in less than milliseconds to serve the purpose of spatial encoding and enable faster scanning. In electromagnetic theory, combination of electric and magnetic force produces Lorentz forces, which is proportional to the magnetic field strength and gradients amplitude in MRI scanners. Lorentz forces causes mechanical vibrations of the gradient coil, which result in sound pressure waves perceived by patients as acoustic noise. Efforts toward acoustic noise reduction can be grouped into two categories: hardware based and software based approaches. According to the linear response theory introduced by Hedeen and Edelstein [10], the output acoustic noise level can be determined by a transfer function, i.e. frequency response function (FRF) and input gradient waveform of the three axes. The FRF is determined by hardware settings of the system, and can be measured to design 'soft' versions of generic MRI pulse sequences [9, 11]. Hennel and colleagues developed silent versions of basic MR sequences by using sinusoidal ramps, including gradient-echo, spin-echo and rapid acquisition with relaxation enhancement sequences. Based on the principle that the FRF of gradient system is relatively low in the frequency range below 200HZ, band-limited gradient pulse shapes, i.e. sinusoidal ramps can be applied and adjusted to fit the spectra to FRF minima.

Three sequences were compared to demonstrate the influence of imaging gradient on the acoustic noise level: the product EPI sequence, sinusoidal readout gradient with blipped and constant phase encoding. Echo spacing was switched from 548 us to 1328 us to find the main frequency to minimize acoustic noise.
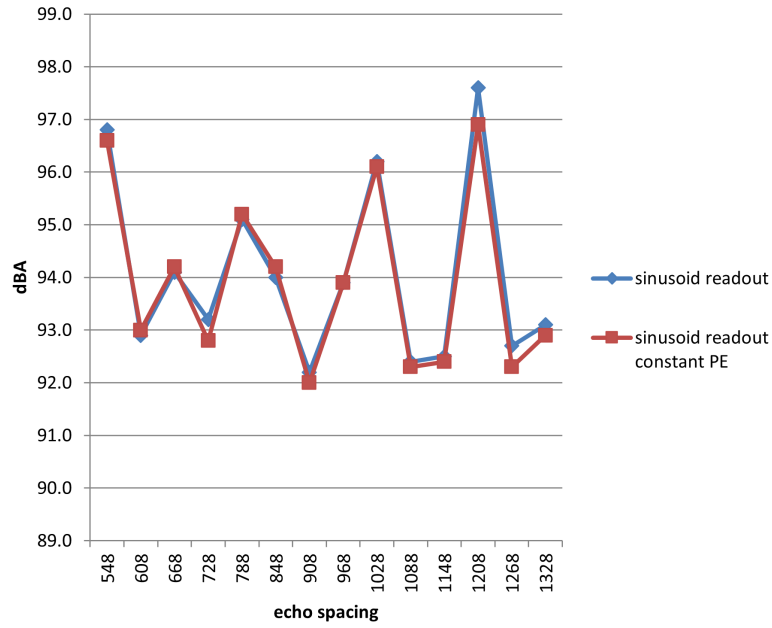
(a) Comparison of sinusoid readout+blipped phase encoding and sinusoidal readout+constant phase encoding, LAeq
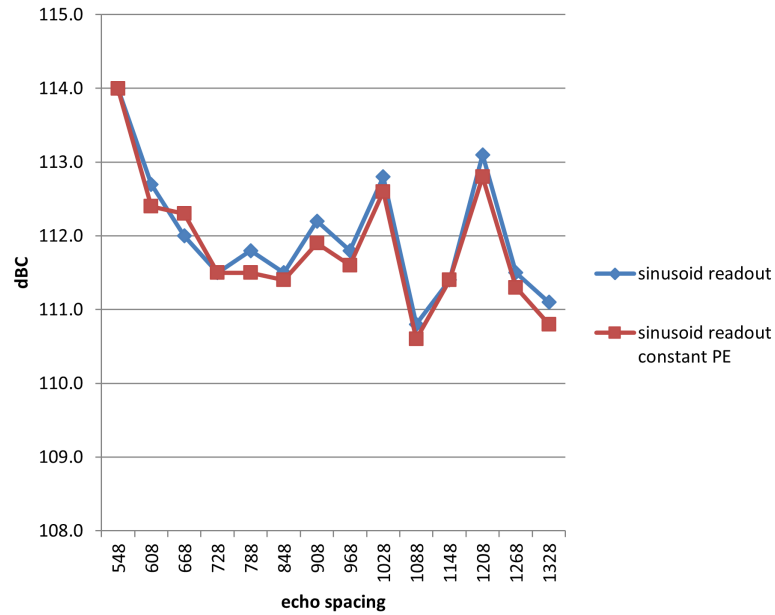
(b) Comparison of sinusoid readout+blipped phase encoding and sinusoid readout+constant phase encoding, LCpeak

Figure 2.9: Comparison of acoustic noise level from sinusoidal readout EPI sequence with blipped phase encoding and constant phase encoding

Previous studies reported that the placement of microphone has significant impact on SPL measurements [12]. In current work, the microphone was placed approximately at the location of the patient's right ear, and was kept constant for all sequences. The comparison between sinusoidal readout EPI sequences with blipped and constant phase encoding showed no difference in SPL measurement, suggesting that the main contribution of acoustic noise comes from frequency encoding. When echo spacing was set to 548, 1028 and 1208 us, the sequence produced maximum acoustic noise. This was consistent for all three sequences compared.

Silent EPI sequences have more significance for fMRI applications. Since scanner noise can cause unwanted blood oxygen level dependent (BOLD) signal in auditory cortex, noise reduction is especially nontrivial for auditory fMRI. Schmitter and colleagues reported using modified EPI sequences with 20 dBA in noise reduction for autitory and non-auditory fMRI [5]. The low acoustic noise EPI sequence was validated with 5 subjects and produced activation map with higher statistical significance compared to the standard EPI sequences. Hutter and colleagues [13] presented a framework of acoustic noise reduction for all EPI based sequences, including fMRI and DWI. The framework utilized sinusoidal EPI readout and constant phase encoding gradients, as described in the current work. In addition, they merged the crusher into diffusion gradient to further refine the sequence, and full optimization was conducted by tuning the frequency response functions of the gradient system. They achieved up to 12 dBA reduction in acoustic noise with maintained image quality, SNR and diffusion measures compared to standard sequence, illustrated in adult and fetus imaging.

The Lorentz force is proportional to the magnetic field strength, therefore so increases the acoustic noise, as indeed the case for the range of 0.2-3.0T [14]. Due to the trend towards using higher field strengths, safety and subjective tolerance of ultra-high field MRI scanner has raised wide interests and investigated by several studies. Contrary to intuitive speculation, the acoustic noise of ultra-high field scanner (7T) is only slightly higher than a clinical 3 T scanner [15]. This is because noise level is not solely determined by field strength, but also closely related to the engineering of gradient system. However, head coils designed for 7T systems are much more tight-fitting than that for 3T system, making it impossible to use headphones in 7T. As a common practice in 3T, headphones and earplugs are used together to ensure effective noise suppression, whereas patients rely solely on earplugs in 7T system, of which the effectiveness depends critically on correct

insertion and geometry of ear canal. Not surprisingly, side effects on 7T are larger than the reported for lower field strengths and 33% of subjects reported excessive acoustic noise as distress and the overall [16]. One recent study has shown the feasibility of using quiet sequences in 7T MRI [17] by keeping gradient activities to minimum on each physical axis, achieving acoustic noise reduction 13.8 dBA, which equals to 80% reduction in sound pressure for FLAIR sequence with maintained image quality. Thees studies assist evaluating subject tolerance and help to bring ultra-high field MRI into clinical practice.

In the current work, the main frequency of acoustic spectrum was swept from 912 HZ to 377 HZ (corresponding to echo spacing of 548 *us* to 1328 *us*) to empirically find the optimal echo spacing. For future studies, the scanner FRF can be explicitly measured to minimize output acoustic noise. Theoretically, it can be measured by recording the acoustic response of a certain gradient coil after a delta pulse excitation, but in practice this cannot be realized. Another approach is to sweep the frequency of the sinusoidal gradients continuously in the range of interest and record the scanner responses. Furthermore, crusher gradients placed beside the refocusing RF pulse can be merged into diffusion gradients to further reduce acoustic output. In addition, it would be interesting to investigate the contribution of each physical gradient axis to the acoustic noise level. Since the frequency encoding utilizes the heaviest gradient capacity and produces majority of output acoustic noise, the physical axis of frequency encoding direction can be determined accordingly.

Chapter 3

Silent Diffusion MRI Using Magnetization Prepared RUFIS

3.1 Introduction

Diffusion MRI provides information of white matter microstructure and reveals information that is not available by other imaging modalities [18]. As described in the last chapter, the majority of diffusion technique is based on 2D single-shot echo planar imaging (SS-EPI), due to its high speed and insensitivity to motion[19]. However, SS-EPI sequence suffers from limited spatial resolution and severe off-resonance distortion artifacts, which are even more predominant with higher magnetic field [20]. Compared to 2D sequences, 3D sequences have the advantage in obtaining isotropic voxel and contiguous slices, thus improving the accuracy of diffusion analysis[21, 22, 23].

Great efforts have been investigated into developing non-SS-EPI diffusion sequence, such as diffusion weighted turboFLASH [24, 25], SSFP [26], FISP [27] etc. These sequences utilize a diffusion preparation block, typically comprised of diffusion weighting gradient inserting into Standard driven equilibrium Fourier transform (DEFT) [28] pulses, and tips the diffusion weighted transverse magnetization into longitudinal axis before the signal read out, which is denoted as diffusion weighted driven equilibrium (DWDE). DEFT method consists of 3 consecutive hard RF pulse [90°x–180°y–90°-x], which is originally used for enhancing T2 contrast or reducing unwanted T1 contrast without increasing TR. The mag-

netization is excited by the first 90°x pulse, refocused by the 180°y pulse and flip back to the longitudinal axis by the second 90°x pulse. The use of DEFT in combination with gradient echo is also called T2-prep, which can increase T2 weighting without increasing TE [29]. Diffusion weighted longitudinal magnetization can also be created by inserting diffusion gradient into the DEFT pulses [24, 25]. In comparison to single-shot diffusion weighted EPI, multi shot acquisition is usually performed using these techniques, resulting in higher spatial resolution and reduced distortion. In addition, the shorter preparation time compared to TE in SS-EPI could ameliorate signal decay problem due to T2 relaxation. The feasibility of using DWDE to create diffusion contrast is validated in previous studies [24, 25, 26, 27, 30].

As another alternative, stimulated echo (STE) is formed by the combination of three 90° RF pulses [31], and has broad application in chemical-shift-selective imaging, zoom imaging, multi-slice imaging etc. In STE sequence, the first and third interval of RF pulses is referred to as TE/2, as the magnetization is in the transverse plane and decay with T2 effect; The second interval is referred to as middle interval as the magnetization is in the longitudinal axis and relaxes with T1 effect. The sequence is very versatile because of variations of timing of the three RF pulses and spatial encoding. However, a main disadvantage is that STE inherently have half of the signal amplitude as comparable spin echo, thus lead to reduced SNR. Diffusion weighted STE experiment can be conducted by inserting diffusion gradient into the first and third interval of the RF pulses. The main advantage of DW STE is that diffusion time Δ is not limited by T2 decay, thus long Δ is made possible for tissue with T1≫T2 and achieve big diffusion sensitivity. Modified DW STE schemes are proposed [32] to overcome additional signal attenuation caused by background gradient, therefore avoiding systematic error in diffusion measurement. Another study [33] utilized DWDE in combination with STE for a limited imaging volume, and reduced susceptibility artifact in SS-EPI. The stimulated echo acquisition mode (STEAM) overcomes the bulk motion effect in diffusion preparation by using cardiac triggering to synchronize two diffusion gradient lobes to the same cardiac phase of two neighboring cardiac cycles. Edelman et al. [34] utilizes this technique in cardiac diffusion imaging and spread the diffusion period to the entire cardiac cycle. This is not possible in spin echo sequence due to the limitation of T2 decay. The main assumption for this approach is that the bulk motion is repeatable for each cardiac cycle, which is valid for healthy volunteers [35, 36]. Dou et al [37] applied two bipolar

diffusion gradients at the identical phase of consecutive cardiac cycles, to achieve flow compensation and limiting the diffusion sensitivity to the duration of each bipolar pulses, thus the diffusion preparation scheme is insensitive to periodic motion and cardiac strain.

RUFIS is a rapid radial acquisition sequence that utilizes a succession of low flip angle RF to readout FID [38]. In contrast with traditional spin echo and gradient echo, the frequency encoding gradient in RUFIS is turned on before the nonselective RF excitation, therefore enables detecting the freshly created transverse magnetization without any delay. RUFIS makes it possible to image tissue with ultrashort T2 time like bone structure or lung [38, 39], which is not visible in standard MR sequences in which TE are typically in range of millisecond, thus the signal has already decayed at the time of acquisition. Except for the advantage of imaging tissue with extreme short T2, RUFIS has some other advantages. First, the frequency encoding gradient is gradually reoriented with every TR. Therefore, it has a lower demand on hardware in terms of slew rate and reduces eddy current effect and acoustic noise caused by readout gradient. Second, the sequence is time efficient owing to its short TR [39]. Third, the RUFIS is less prone to inhomogeneity of the magnetic field [40], because the time between excitation and readout is extremely short. It can image tissue in air-tissue interfaces and implants.

However, RUFIS faces several challenges and limitations. First, the spatial encoding gradient is on during the RF pulses. Therefore, RF excitation pulse needs to be short enough to achieve high bandwidth allowing uniform excitation over the whole volume. This puts limit on achievable RF flip angles and requires the RF hard pulse to be large to enough to achieve it, causing higher requirement for hardware and increasing SAR. Second, the dead time from RF transmitting to receiving causes the missing data points in k-space center, which must be compensated to achieve robust reconstruction. Several techniques have been proposed to this end [40, 41, 42, 43]. In addition, the solid material in hardware may cause additional artifact. The contrast option is limited in RUFIS as the choice of TE and flip angle is limited. RUFIS is inherently proton density and T1 weighted depending on different choice of TR and flip angle [40]. Preparation block is needed in order to achieve other contrast. Previously, long T2 suppression preparation [44] and magnetization transfer contrast preparation [45] is already implemented for RUFIS. In the current project, we plan to implement diffusion contrast using preparation block based on DWDE.

There's a dead time between RF transmission and data acquisition in RU-FIS. However, as the k-space acquisition starts after the center of RF pulse, data in the k-space center is omitted. Two kinds of techniques have been developed for the purpose of compensating the gap in k-space center. In the first class of technique, the missing k-space center is acquired using additional measurement. PETRA [40] (pointwise encoding time reduction with radial acquisition) consists of a radial projection imaging part to acquire high spatial frequency data, and Cartesian single point imaging (SPI) part to acquire low resolution k-space center. The radial part of the sequence employs the same strategies as in normal projection imaging. Hard low-flip angle pulses are applied during the frequency encoding gradient, followed by the readout of one k-space data spoke after dead time. The start of data readout is set to TE, which is flexible given the value is bigger that the dead time plus half of the RF duration. The absolute readout gradient strength $|\vec{G}| = \sqrt{G_x^2 + G_y^2 + G_z^2}$ is kept constant for all the directions. Therefore, a sphere in k-space center with $|k| < \gamma|\vec{G}|TE$ is missing. The missing points are filled up point wisely during the Cartesian SPI acquisition. One single point is acquired at $t = TE$ after each RF excitation during readout gradient. The orientation as well as strength of the gradient is adjusted given by the desired k value. Another technique, water- and fat-suppressed proton projection MRI (WASPI) [44], acquires the missing k-space center using additional scan with reduced gradient strength and acquisition bandwidth. With decreased bandwidth, dead time is decreased in unit of dwell time. Consider using the reduced gradient strength and dwell time increased by the same factor. The missing data points can be regained when the dwell time equals the dead time. The two datasets can be combined using linear transition and 3D gridding. In the other class of technique, the missing data points are filled up by algebraic reconstruction (AR) [43]. Each k-space data line is over-sampled after the dead time. AR combines two acquisitions with the same direction but opposite in polarity together to create 1-D projection, from which the k-space data without initial gap and oversampling is obtained using inverse Fourier transform, followed by standard 3D gridding reconstruction.

The current study aims to develop a novel multi-shot acquisition scheme for diffusion prepared RUFIS to improve image quality and patient comfort. Compared to diffusion weighted single-shot echo planar imaging (SS-EPI), which suffers from severe distortion and produces loud acoustic noise, the new technique is more robust against susceptibility artifacts and reduces the level of acoustic

noise. Its inherent multi-shot capability enables acquisition of high resolution diffusion weighted images.

3.2 Theory

3.2.1 Diffusion weighting schemes and motion sensitivity

Diffusion can be characterized as random walk of molecules in tissue or other media. The unrestricted diffusion can be described by the Einstein equation:

$$r_{rms} = \sqrt{2Dt} \tag{3.1}$$

Where the r_{rms} is the one-dimensional root-mean-squared displacement that takes place during diffusion time t and the diffusion coefficient D. For 3D cases, the equation becomes $r_{rms} = \sqrt{6Dt}$. The diffusion coefficient of water at 37°C is $3 \times 10^{-3} mm^2 s^{-1}$. In biological tissues, diffusion process is hindered by macromolecules, cellular structures etc. These obstacles can considerably reduce the D of water and cause diffusion anisotropy, i.e. the diffusion rate varies with spatial orientation.

The basic scheme of modern diffusion measurement by NMR was introduced by Stejskal and Tanner [46], called pulsed gradient spin-echo, where the diffusion sensitizing gradients were inserted into a spin-echo sequence, As demonstrated in Figure 3.1. The diffusion pulse duration δ is the encoding time, and the separation of the two pulses Δ is the diffusion time. According to Equation (1.8), spins experience different field strength along the gradient direction and therefore have different Larmor frequency. The spin displacement from Brownian motion causes phase change when applying diffusion gradients,

$$\phi = \phi_2 - \phi_1 = -q(x_2 - x_1) \tag{3.2}$$

Where $q = \gamma \delta G$, x_2 and x_1 are the spin position at the first (dephasing) and second (rephasing) diffusion gradient lobes. When spins remain stationary so $x_2 = x_1$, the net phase ϕ is zero as the phase given by dephasing and rephasing gradients cancel each other. When spins diffuse randomly, net phase accumulated within the voxel, i.e. phase dispersion, causes signal attenuation on top
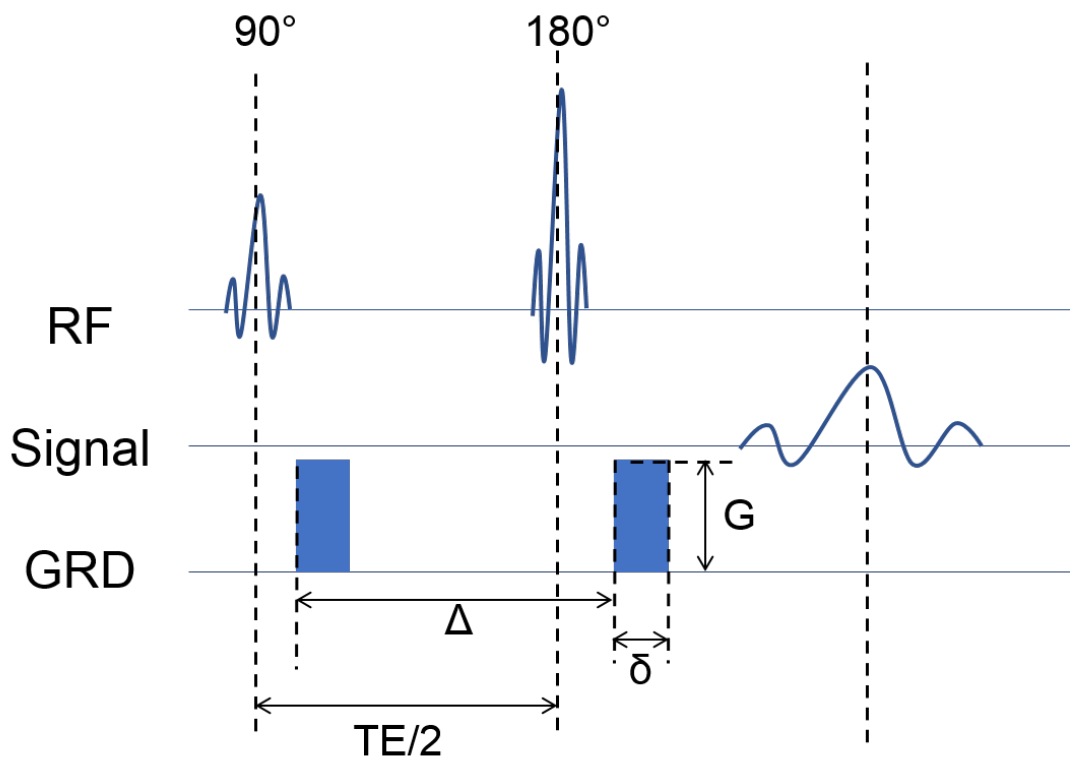
Figure 3.1: Stejskal-Tanner diffusion weighting technique, where the diffusion sensitizing gradients were inserted into spin-echo sequence. The diffusion pulse duration δ, separation of the two pulses Δ, and echo time $TE/2$ are indicated in the diagram.

of relaxation effect. The signal attenuation can be obtained by using two signal measurements, typically one with diffusion encoding and the other without.

$$\frac{S_b}{S_0} = \exp(-\phi_2) = \exp(-bD) \tag{3.3}$$

$$b = \gamma_2 G_2 \delta_2 (\Delta - \delta/3) \tag{3.4}$$

Equation (3.4) shows the calculation of b value of the Stejskal-Tanner diffusion scheme illustrated in Figure 3.1. B value is determined by the strength and duration of diffusion gradients, and characterizes the level of diffusion sensitivity induced by the gradients. The ratio of measurements with and without diffusion weighting, S_b/S_0, is determined by the product bD. When sensitized to diffusion, also introduced unwanted sensitivity to bulk motion, The effect of bulk motion on diffusion preparation can be modeled using the concept of gradient moments. In absence of bulk motion, the Stejskal-Tanner scheme would result in a signal decay reflecting incoherent phase shifts arising from microscopic thermal motion. In presence of bulk motion, assuming proton moves along the x axis, the initial position x_0, velocity v_0 and acceleration a_0. Then the location of proton at later times $x(t)$ can be the extrapolated by the Taylor series expansion:

$$x(t) = x_0 + v_0 t + \frac{1}{2} a_0 t^2 + \cdots \tag{3.5}$$

The resultant transverse magnetization has a coherent non-zero phase ϕ, which can be calculated as follows:

$$\begin{aligned}
\phi(t) &= \gamma \int_0^t G(u)x(u)du \\
&= \gamma \int_0^t G(u)(x_0 + v_0 t + \frac{1}{2} a_0 t^2 + \cdots)du \\
&= \gamma m_0(t)x_0 + \gamma m_1(t)v_0 + \frac{\gamma}{2} m_2(t)a_0 + \cdots
\end{aligned} \tag{3.6}$$

In Equation (3.6), m_0, m_1 and m_2 represents the zero order, first order and second order gradient moment respectively. Gradient moment nulling (GMN) is the process to design gradient waveform insensitive to artifacts caused by bulk

motion. The nth gradient moment is written as:

$$m_n(t) = \int_0^t G(u)u^n du \tag{3.7}$$

3.2.2 Eddy current and compensation

Eddy current is a function of the amplitude of the gradient transition followed by a multi-exponential decay. The rise and fall part of a single trapezoid gradient waveform induces the same amount of eddy current in opposite polarity. The existing eddy current after the application of trapezoid gradient can be described as:

$$EC = EC_0(e^{-\frac{t-t_a}{\tau}} - e^{-\frac{t-t_b}{\tau}}) = EC_0 e^{-\frac{t}{\tau}}(e^{\frac{t_a}{\tau}} - e^{\frac{t_b}{\tau}}) \tag{3.8}$$

Where t_a and t_b denotes the time points for the rising and falling portion of trapezoid respectively, and EC_0 being the initial amplitude of eddy current as a function of amplitude of the gradient transition. If shorter trapezoid waveforms are utilized, the residual eddy current tends to cancel each other, resulting in a minimum distortion on images.

When utilizing DWDE preparation, the spatially dependent eddy current lead to the variation in final longitudinal magnetization after the tip up pulse. This effect again can be eliminated using phase cycling and SRSS technique [47, 25]. Another approach is to apply dummy cycle gradients that are identical to the timing and amplitude of diffusion gradients before the start of actual diffusion preparation. This is to create a steady state of eddy current before the excitation and tip-up pulse of the diffusion module.

3.2.3 Correction for T1 contamination

The magnetization continues to evolve after diffusion preparation, known as the longitudinal relaxation, which introduces unwanted T1 weighting into the diffusion contrast. If not accounted for, it can cause significant error into the diffusion measurements. When using Cartesian trajectory, this problem can be addressed by acquiring central k-space lines immediately after the preparation block. In radial imaging, the contrast is equally updated by each spoke, thus it's not possible to manipulate contrast by rearranging k-space acquisition order.
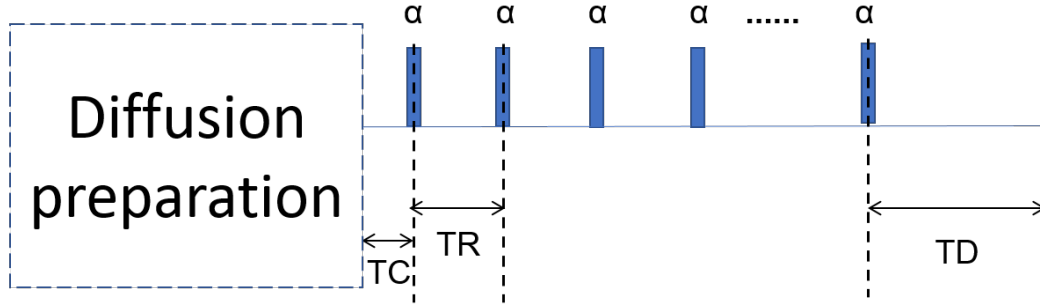
Figure 3.2: Diffusion-weighted RUFIS sequence. A diffusion-weighted preparation is applied before RUFIS readout. TC is the time delay needed for crusher gradient to eliminate the residual transverse magnetization. TR is the repetition time between consecutive α pulses and TD is the time allow for magnetization recovery before the next diffusion reparation.

Figure 3.2 is the sequence diagram for Diffusion-weighted sequence featuring RUFIS readout. Denote the longitudinal magnetization before and after the $n^{th}\alpha$ pulse as $M_z(n_-)$ and $M_z(n_+)$, their relationship can be described as:

$$M_z(n_+) = M_z(n_-)\cos\alpha \tag{3.9}$$

Between the consecutive RF pulses, the magnetization continues to evolve as longitudinal relaxation,

$$M_z(n+1_-) = M_z(n_+)E_{TR} + M_0(1 - E_{TR}) \tag{3.10}$$

Where $E_{TR} = \exp{-TR/T1}$, M_0 is the longitudinal magnetization at equilibrium.

Substituting Eq. (3.9) into Eq. (3.10), we get the relationship between $M_z(n_-)$ and $M_z(1_-)$, which is the longitudinal magnetization before the first α pulse:

$$M_z(n_-) = M_z(1_-)(E_{TR}\cos\alpha)^{n-1} + M_0(1 - E_{TR})\frac{1 - (E_{TR}\cos\alpha)^{n-1}}{1 - E_{TR}\cos\alpha} \tag{3.11}$$

The $M_z(1_-)$ is the longitudinal magnetization before the first α pulse, determined by the diffusion preparation and the time delay TC for crusher gradients .

$$M_z(1_-) = M_0 E_{TP}\exp(-bD)E_{TC} + M_0[1 - E_{TC}] \tag{3.12}$$

Where TP is the duration of diffusion preparation, $E_{TP} = \exp(-TP/T2)$ and stands for the T2 attenuation during the preparation block, $E_{TC} = \exp(-TC/T1)$,

D is the diffusion coefficient and b is the b value. According to Eq. (3.11) and (3.12), the transverse magnetization $M_t(n)$ after the $n^{th}\alpha$ pulse can be expressed as

$$
\begin{aligned}
M_t(n) &= M_z(n_-)\sin\alpha \\
&= [M_z(1_-)(E_{TR}\cos\alpha)^{n-1} + M_0(1 - E_{TR})\frac{1 - (E_{TR}\cos\alpha)^{n-1}}{1 - E_{TR}\cos\alpha}]\sin\alpha \\
&= A(n)\exp(-bD) + B(n)
\end{aligned}
\tag{3.13}
$$

Eq. (3.13) shows that the transverse magnetization, therefore the detected signal can be split into diffusion dependent and independent terms $A(n)\exp(-bD)$ and $B(n)$

$$
\begin{aligned}
A(n) &= M_0 E_{TP} E_{TC}(E_{TR}\cos\alpha)^{n-1}\sin\alpha \\
B(n) &= [M_0(1 - E_{TC})(E_{TR}\cos\alpha)^{n-1} + M_0(1 - E_{TR})\frac{1 - (E_{TR}\cos\alpha)^{n-1}}{1 - E_{TR}\cos\alpha}]\sin\alpha
\end{aligned}
\tag{3.14}
$$

As quantitative diffusion measures are obtained by linear fit of logarithm of diffusion-weighted signal S_b, the diffusion independent terms $B(n)$ will introduce systematic error if not accounted for.

The diffusion independent term can be eliminated using a phase cycling scheme [24], where the 90° tip-up pulse and α pulses in the readout are phase cycled and the receiver phase stay fixed: $[90°_x - 180°_y - 90°_{(-x,x)}]_{prep} - TC - [\alpha_{(x,-x)}]_n$. When subtracting data of these two sequences, diffusion independent terms in Eq. (3.13) cancel each other and the resulting magnetization is given by

$$
\begin{aligned}
M_t(n) &= 2M_0 E_{TP} E_{TC}\exp(-bD)(E_{TR}\cos\alpha)^{n-1}\sin\alpha \\
&= 2A(n)\exp(-bD)
\end{aligned}
\tag{3.15}
$$

Therefore, the diffusion coefficient D can be calculated without the systematic error caused by T1 relaxation.

3.3   Methods

3.3.1   Simulation studies

Varies factors that may influence the image quality were investigated by simulation, including signal attenuation caused by bulk motion during the diffusion preparation block, and signal contamination from T1 recovery during readout.

Effects of bulk motion

In order to investigate the signal fluctuation arisen from brain pulsation, an iterative Bloch simulation was conducted considering the diffusion gradients and bulk motion effects. The simulation put $N = 10^3$ spins in a single voxel of size $1mm \times 1mm$. Each spin was assigned with a 3D position vector and a magnetization vector. During each time step of $0.05\ ms$, random walk of water molecules were calculated according to the diffusion coefficient D, and position vectors were updated according to the Einstein equation $\Delta x = \sqrt{2DT}$. Bulk motion arisen from brain pulsation was calculated based on the data from reference [48]. Only the motion along the direction of diffusion gradient was considered. The magnetization vector was updated according to the Bloch equation, by taking the RF pulses, diffusion gradients and relaxation into account. The impact of brain pulsation on signal attenuation for different diffusion preparation schemes was examined: Stejskal-Tanner diffusion scheme with and without bulk motion; a flow compensated diffusion scheme, and SRSS technique for Stejskal-Tanner diffusion scheme.

Effects of T1 relaxation

The simulation was conducted using MATLAB to investigate the effect of imaging parameters and RF cycling scheme to reduce T1 contamination for diffusion prepared RUFIS. We set up a 3D uniform sphere phantom for simulation, represented by a 16^3 matrix. The phantom was assigned with: $T2 = 80ms$, diffusion coefficient $D = 10^{-3}mm^2/s$ and variable T1 values ranging from 600 to 1800 ms. Diffusion prepared RUFIS acquisition was set for perfect diffusion preparation (duration $Tprep = 50ms$) and 256 spokes, 8 data points and $TR = 1.5ms$ per

spoke for the readout, and encoding matrix was calculated accordingly. The simulated k-space data was multiplied by a weighting function corresponding to the evolution of longitudinal magnetization affected by T1-recovery and repetitive excitation. Algebraic image reconstruction was applied via explicit inversion of the encoding matrix.

The diffusion coefficient was calculated based on the model $log(S_b/S_0) = -bD$. A region in the central part of the image profile was chosen, and the mean calculated diffusion coefficient D_{cal} was compared to the input D_{in}. The systematic deviation of measurement was represented in percentage: $DEV = (D_{cal} - D_{in})/D_{in} \times 100\%$. The impact of flip angle and b-value on the underestimation of D, as well as the correction method using phase cycling was investigated.

3.3.2 Sequence implementation

The diffusion prepared RUFIS sequence consisted of a diffusion preparation block to generate diffusion weighted longitudinal magnetization, followed by a segmented 3D radial RUFIS readout. The missing k-space gap caused by finite RF transmit-receive switching was reacquired using a second measurement with reduced imaging bandwidth [42]. The two measurements were merged and reconstructed using 3d gridding. The diffusion-weighted driven-equilibrium preparation module consisted of [90°x–180°y–90°-x] RF pulse train with diffusion gradients inserted besides the 180° refocusing pulse. Dummy cycles were played out before the excitation to reduce eddy current artifacts [49]. The preparation time was $56ms$ for Stejskal-Tanner (ST) schemes and $90ms$ for flow compensated (FC) scheme for a b value of $1000s/mm^2$. The sequence diagram is illustrated in Figure 3.3. Phase cycling was used to reduce T1 signal contamination [24].

3.3.3 Data acquisition

All experiments were conducted on a GE 3.0T MR750w scanner with a GEM head array coil (GE Healthcare, Waukesha, WI). A phantom (DiagnosticSonar, Livingston, UK) consisting of samples with different T1 values was used in the first experiment. The imaging parameters were: flip angle=2°, FOV=$19.2cm$, imaging matrix = $64 \times 64 \times 64$ with $3mm$ isotropic resolution, BW = $\pm31.25kHz$, and $500ms$ wait time between segments for signal recovery. The diffusion coef-
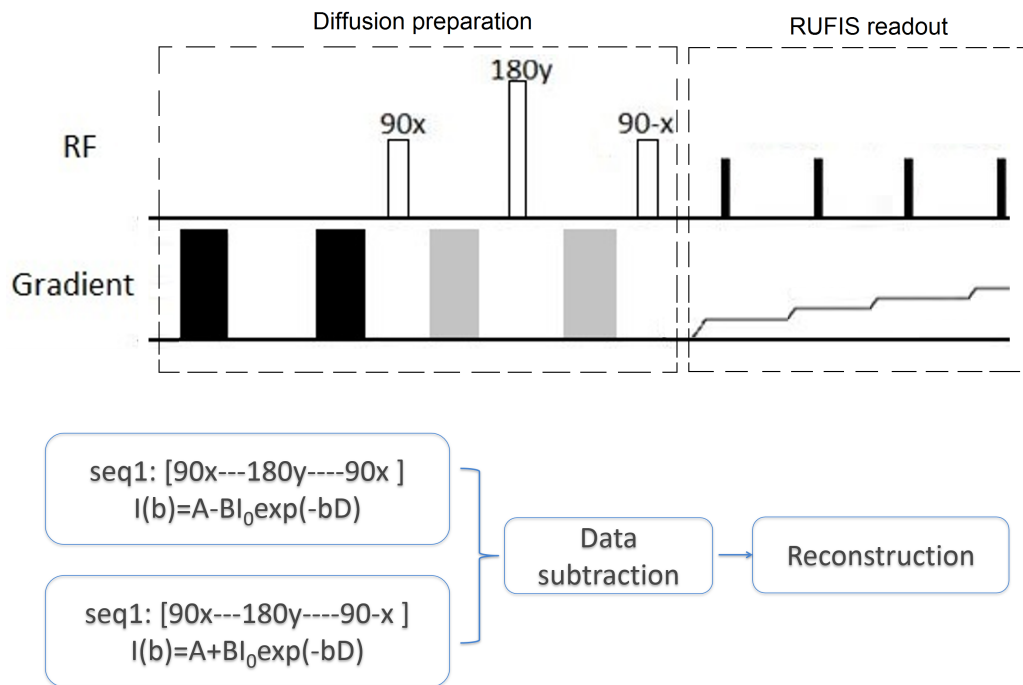
Figure 3.3: Sequence diagram of diffusion weighted RUFIS shown on top. The dummy cycle gradients are illustrated in black and diffusion gradients are illustrated in gray. Bottom: Phase cycling scheme to reduce T1 contamination.

ficient D was measured using different b values $(300, 500, 700, 1000s/mm^2)$. A total of 4868 spokes were acquired for each volume with 256 radial spokes per segment. In addition, a DTI dataset was acquired with b value $=1000s/mm^2$ and six directions on a pineapple to test for anisotropy. Volunteer data were collected using flip angle$=3°$, 256 or 64 radial spokes per segment, with $3mm$ isotropic resolution. Diffusion weighted images with b value$=1000s/mm^2$ were acquired with the Stejskal-Tanner and flow-compensated diffusion scheme, non-diffusion weighting T2 images were acquired with the exact same sequence but diffusion gradients turned off.

3.3.4   Acoustic noise measurement

Acoustic noise measurement was conducted using a Bruel&Kjaer sound level meter (Type 2250) equipped with MR compatible microphone (type 4189). Sound level meter calibration was conducted before the measurement with a 94 dB and 114 dB sound source (Calibrator Type 4231). RF transmit was disabled during the measurement because the RF field can cause damage to the microphone, and RF power has no impact on Sound Pressure Level (SPL). The main contributor to SPL increase during a MRI scan is the gradient coil, which were enabled during all tests. Manual Prescan was started and stopped, in order to start the scan without RF. The acoustic noise of the in-bore ambient background, the original RUFIS sequence, EPI and the diffusion weighted RUFIS was measured in 2 minutes' duration. The microphone was placed at the scanner isocenter inside the head coil. The A-weighted average (LAeq) sound pressure levels were recorded. As human ear does not respond uniformly to all frequencies, A-weighted SPL measurements are most similar to the response of human ear. The A-weighting discriminates against low frequencies, while C-weighting measures almost uniformly over the frequency range.

3.4   Results

3.4.1   Simulation

Figure 3.4 illustrates the underestimation of D caused by T1-recovery using different acquisition parameters. The systematic deviation DEV is shown in red and
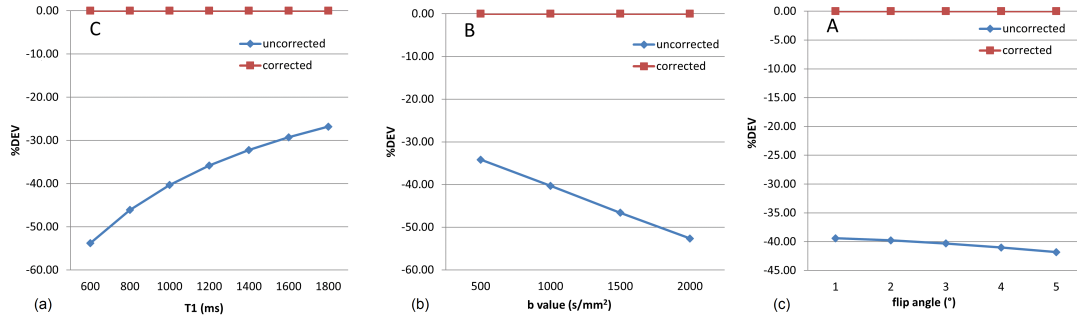
Figure 3.4: Comparison of diffusion coefficient underestimation for different parameters with and without correction: (a) T1 value, (b) b value. (c) flip angle. T1 value was set to 1000ms for (b) and (c), flip angle was set to 3° for (a) and (b), b value was set to 1000 s/mm^2 for (a) and (c).

blue for sequence with and without correction. In Figure 3.4(a), the acquisition parameter were kept at $b = 1000 s/mm^2$, flip angle $= 3°$, DEV ranged from -54% to -27% for T1 value increasing from 600 to 1800 ms. In Figure 3.4(b), b value from 500 to 2000 s/mm^2 were tested when T1 = 1000 ms and flip angle $= 3°$. The DEV ranged from -34% to -53%. Figure 3.4(c) shows the influence of flip angle. When T1 = 1000 ms and b = $1000 s/mm^2$, the DEV was -39% to -42% for flip angle of 2° to 5°. These results confirmed significant underestimation of D caused by T1-recovery without correction schemes, and the deviations are more predominant with increasing b-value, flip angle and decreasing T1. When RF-cycling scheme is employed, bias were reduced to be less than 1% for all cases.
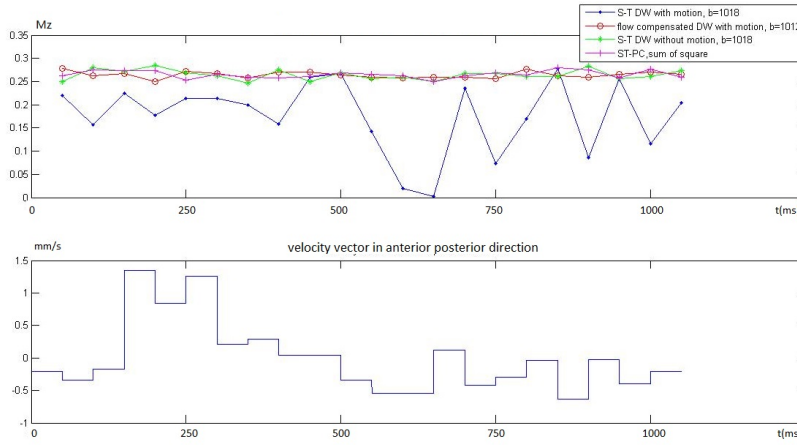
Figure 3.5 presents the final longitudinal magnetization after the tip-up pulse, which corresponds to signal to be acquired in the image. Signal fluctuation caused by brain pulsation occured on all three directions, but largest on foot head direction. Stejskal-Tanner diffusion scheme was significantly affected by brain pulsation. Phase-cycled Stejskal-Tanner and first moment nulled diffusion scheme produced stable magnetization after the tip up pulse. However, this may not be valid in experiments since the motion effect was highly digitalized in the simulation, and only flow was considered.

3.4.2   Observed artifacts

Figure 3.6 shows the dark strips artifacts observed in T2 images. The pattern of artifacts was consistent in different data sets. In volunteer images, they typically appeared on the corners of images. Strip artifacts were also observed in water
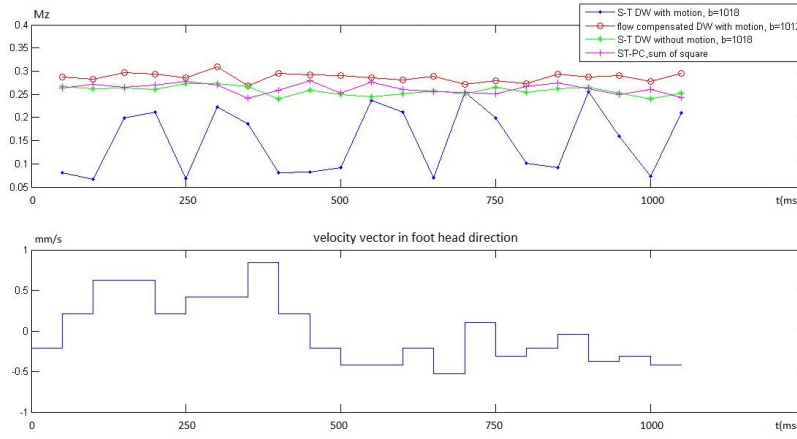
(a) motion simulation in foot-head direction.

(b) motion simulation in anterior-posterior direction.
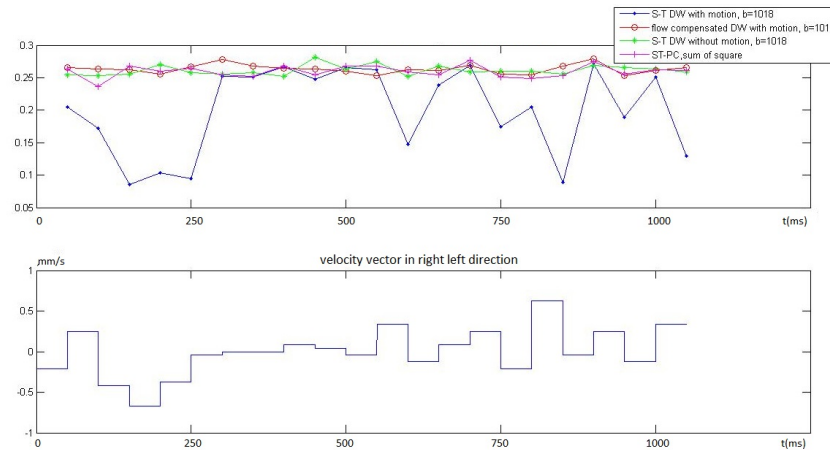
(c) motion simulation in right-left direction.

Figure 3.5: Simulation of brain pulsation effects on diffusion signal. The final longitudinal magnetization (Mz) after Stejskal-Tanner diffusion scheme with and without bulk motion, flow compensated diffusion scheme, and SRSS signal of Stejskal-Tanner diffusion scheme are shown in blue, green, red and magenta. (a), (b) and (c) shows the effect of brain pulsation on the foot-head, anterior-posterior, and right-left directions respectively. The preparation block takes 50ms for all the schemes.

and oil phantom, which could be caused by difference in resonance frequency between water and oil. T2 images of spectroscopy phantom also suffered from dark strip artifacts, and more severe with less spokes per segment. These artifacts could arise from the special characteristic of the spectroscopy phantom (multiple metabolism substances, different dielectric constant etc.). Severe signal loss and modulation was present in different diffusion preparation schemes and directions. Figure 3.7 shows severe signal loss in diffusion images acquired with 64 spokes per segment. In data sets acquired with 256 spokes per segment, the artifacts were much less severe but still observable as shown in Figure 3.8.There are several possible causes. First, strip artifacts were already significant in the T2 images, which were possibly caused by filed inhomogeneity. Diffusion gradients could make it worse. Second, higher orders of coherent motion (acceleration) were not compensated in either of the diffusion schemes. Therefore diffusion images acquired with the flow compensated scheme were no better than images acquired with Stejskal-Tanner scheme. Although the repeat test shown below proved that the flow compensated diffusion preparation reduced majority of motion.

3.4.3 Repeat test

To investigate the amount of signal fluctuation caused by brain pulsation, 15 low resolution, single-shot scans were conducted consecutively with Stejskal-Tanner and flow compensated diffusion encoding along Anterior-Posterior (A/P) and Superior/Inferior (S/I) direction. The signal variance over time (standard deviation divided by mean value) is shown in Figure 3.9. Signal variation of diffusion images in S/I direction is much more than that of A/P direction. This is consistent with previous studies that the majority of flow occurs in the S/I direction [48]. In A/P or S/I direction, signal variation of flow compensated diffusion images is much less compared to Stejskal-Tanner diffusion images, however still exists. This proved that the flow compensated diffusion scheme can resolve most of motion-related artifacts, but higher orders of bulk motion were still non-negligible.
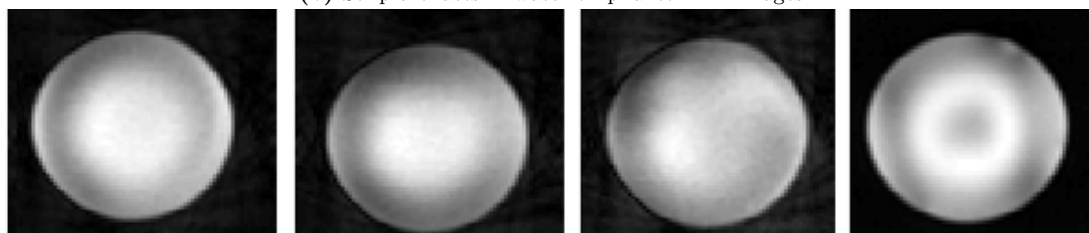
3.4.4 Phantom experiments

Figure 3.10 shows the measured diffusion coefficient of the T1 phantom using different b values. Despite the different T1 values, the phantom has a uniform
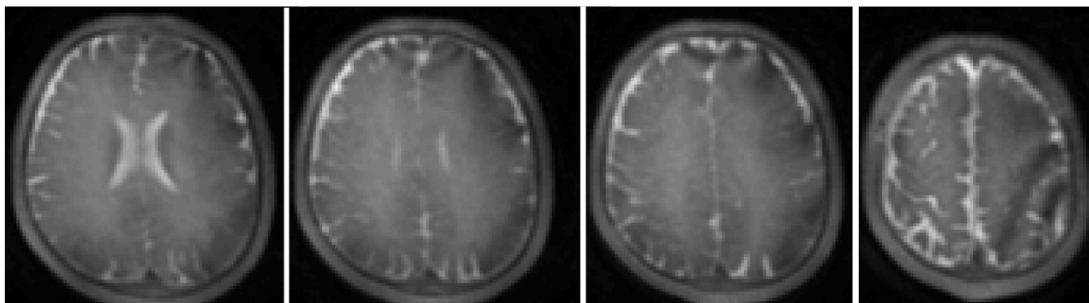
(a) Strip artifacts in volunteer T2 images
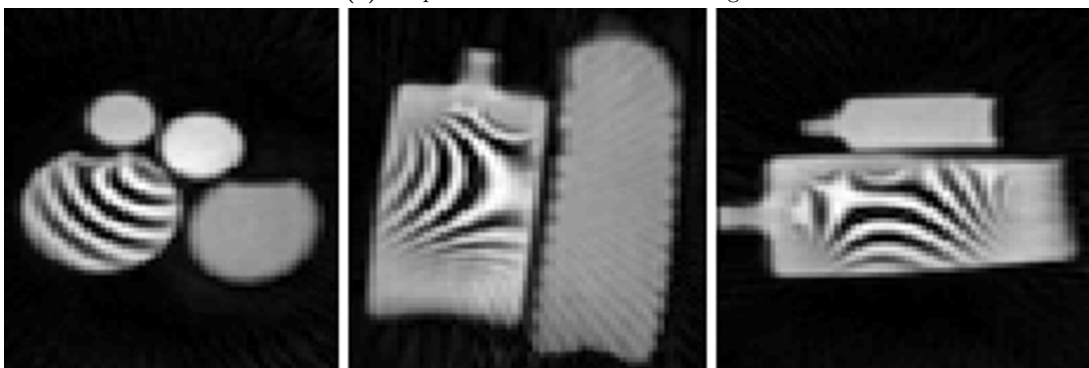
(b) Strip artifacts in water oil phantom T2 images

(c) Strip artifacts in spectroscopy phantom T2 images

Figure 3.6: Strip artifacts in T2 images

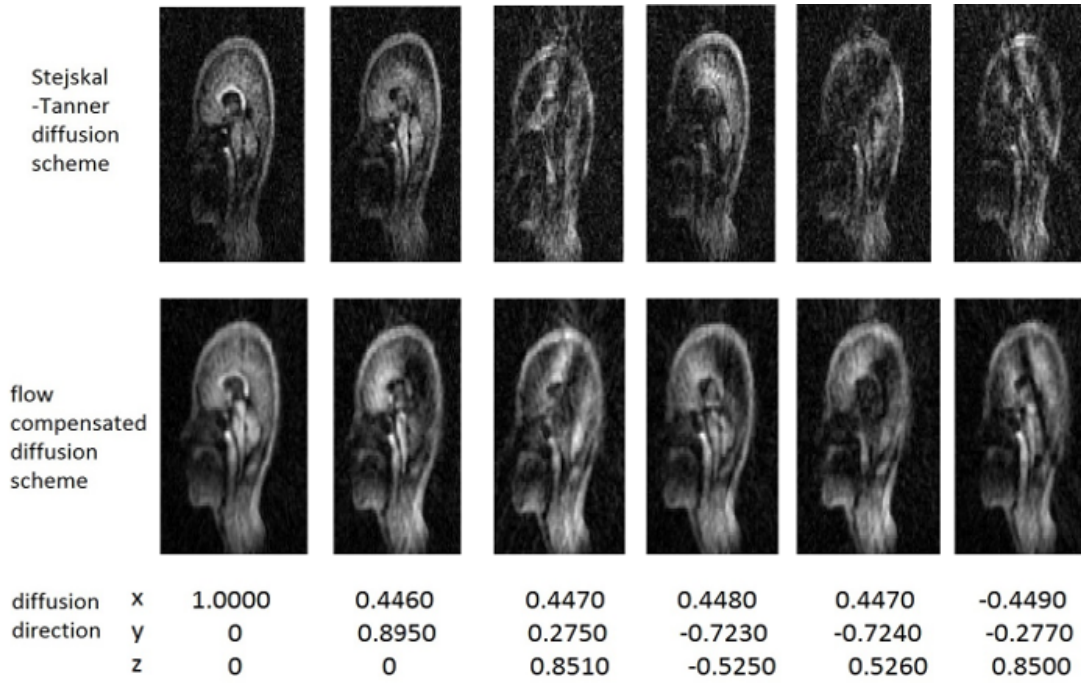| diffusion direction	x	1.0000	0.4460	0.4470	0.4480	0.4470	-0.4490
	y	0	0.8950	0.2750	-0.7230	-0.7240	-0.2770
	z	0	0	0.8510	-0.5250	0.5260	0.8500

Figure 3.7: Severe motion artifacts were present in volunteer diffusion images when acquired with 64 spokes per segment, Stejskal-Tanner or flow-compensated diffusion preparation
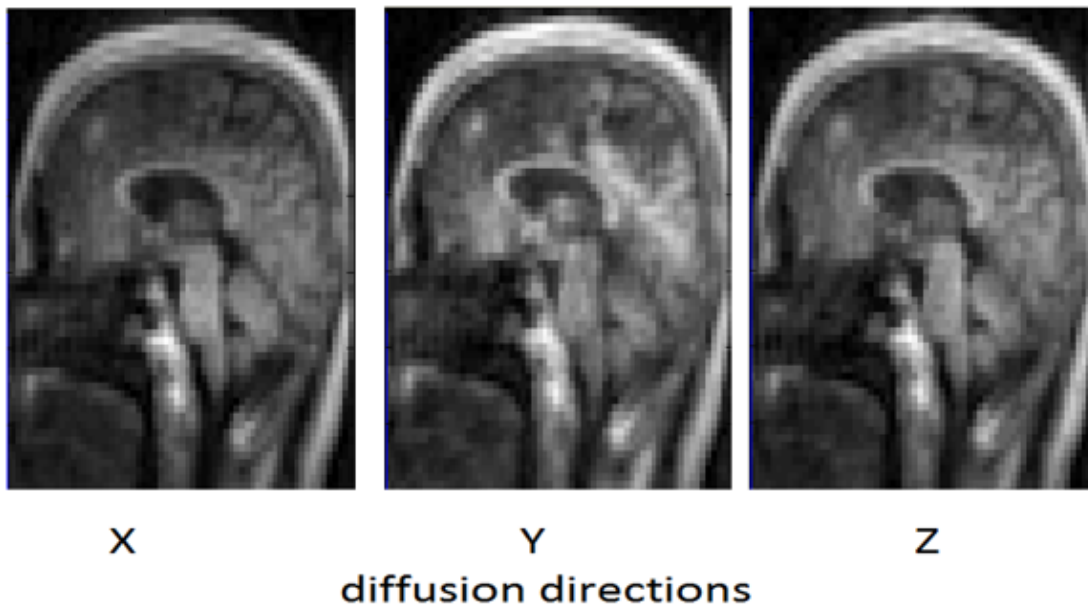

Figure 3.8: Motion artifacts in volunteer diffusion image were less severe when acquired with 256 spokes per segment and with flow-compensated diffusion preparation
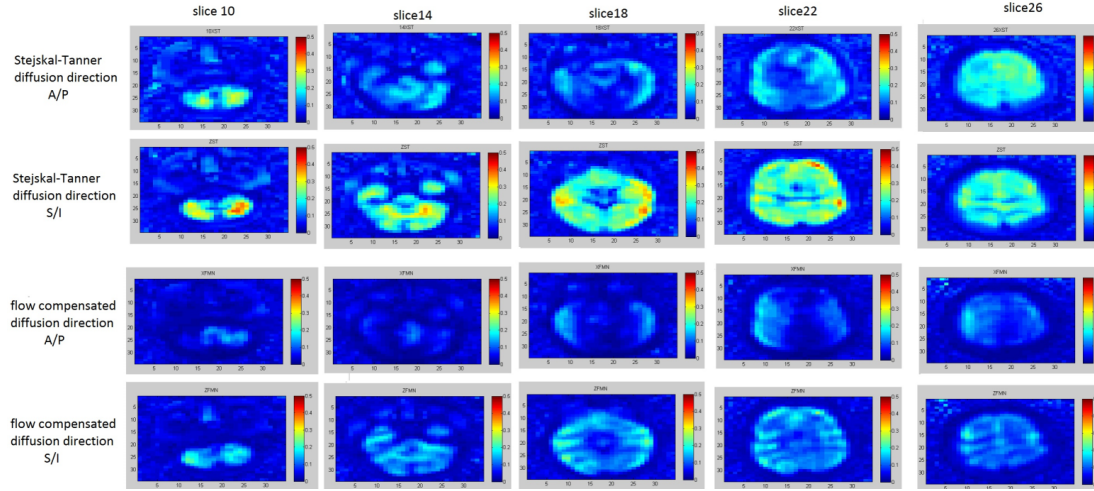
Figure 3.9: Single shot diffusion images to investigate brain pulsation

diffusion coefficient of $2 \times 10^{-3} mm^2/s$, as measured by diffusion weighted EPI. The results indicated that the diffusion prepared RUFIS is capable of measuring diffusion coefficients. A significant underestimation of the diffusion coefficient is observed for samples with short T1 values, in case no phase cycling is employed (red). With the phase cycling scheme employed (blue), the obtained diffusion coefficients are closer to the ground truth. Figure 3.11 shows the fractional anisotropy (FA) and mean diffusivity (MD) map obtained with DW RUFIS and DW EPI respectively. The average FA value from a region of interest (ROI) at the center of the pineapple was 0.125 for DW EPI and 0.135 for DW RUFIS. The average MD value from the same ROI was $0.980 \times 10^{-3} mm^2/s$ for DW EPI and $0.958 \times 10{-3} mm^2/s$ for DW RUFIS.

3.4.5 Acoustic noise measurement

The A-weighted average SPL (LAeq) value of in-bore ambient background were 71.5 dBA. SPL value of DW-EPI (Stejskal-Tanner with b value $= 1000 s/mm^2$, echo spacing=968 us, TR= 5.6 s) was 97.8 dBA. SPL value of DW-RUFIS (Stejskal-Tanner with b value $= 1000 s/mm^2$, 256 radial spokes per segment, 500 ms wait time between segments) was 77.6 dBA, approaching ambient level. Compared to DW-EPI, the proposed DW-RUFIS achieved 20.2 dBA acoustic noise reduction. Since the acoustic measurement is in logarithmic scale, it corresponds to 90% reduction in sound pressure.
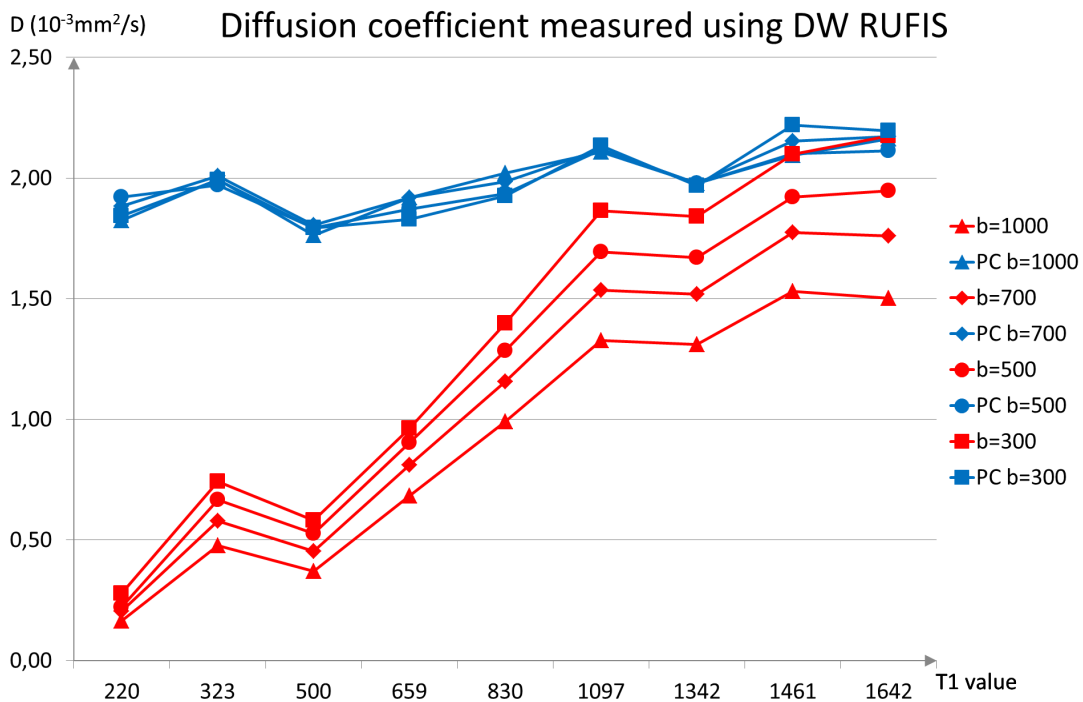
Figure 3.10: The diffusion coefficients measured in phantom using diffusion weighted RUFIS with (blue) and without (red) phase cycling (PC) in phantom with different T1 values. The experiment was repeated with different b value of 1000, 700, 500, 300 s/mm^2 as denoted in triangle, diamond, circle and square.

FA and MD map obtainted by DW RUFIS
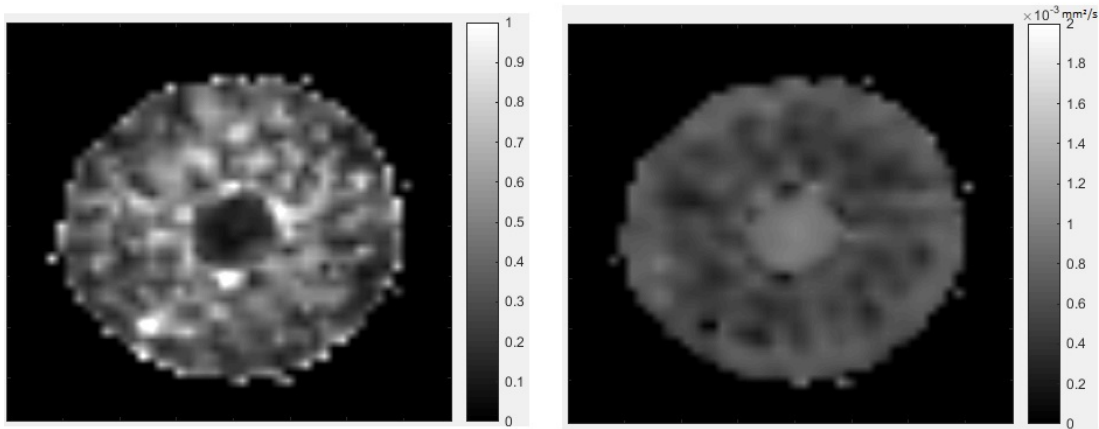
FA and MD map obtainted by DW EPI

Figure 3.11: FA and MD obtained on pineapple as an anisotropy phantom: The left column shows fractional Anisotropy (FA) obtained with DW RUFIS (top) and DW EPI (bottom), the right column shows that of mean diffusivity (MD).

3.5   Discussion

The current study proposed a novel diffusion weighted sequence based on RU-FIS with the advantage of reduced distortion and acoustic noise. The biggest concerns were artifact and metrics bias caused by motion, eddy current and T1 contamination. The sequence and correction techniques were first addressed by simulation, and then va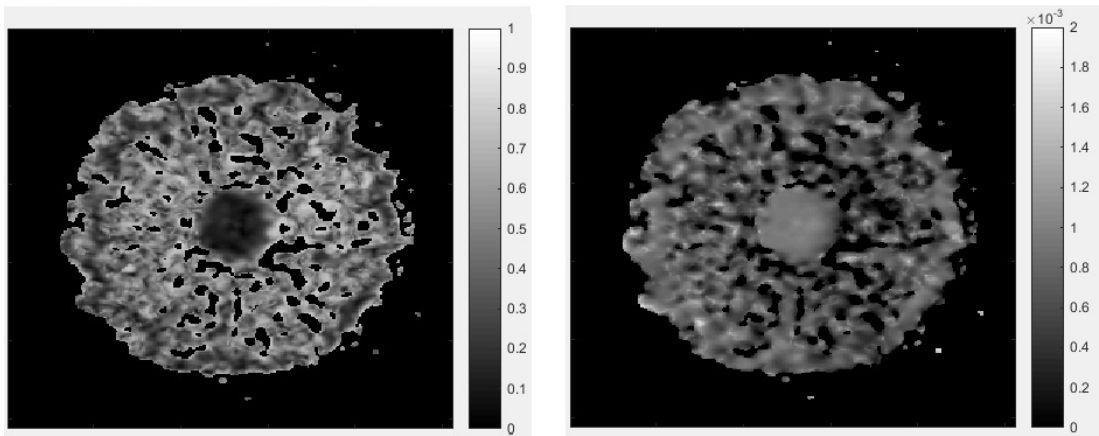lidated on phantom and volunteers. The diffusion metrics acquired by the proposed method were compared and found consistent with gold-standard diffusion EPI.

T1-recovery during readout is a common issue for magnetization prepared sequences and introduces unwanted bias. Previous studies reported strategies including optimizing imaging parameter [26], RF phase cycling [24] or k-space filtering [24, 50] to reduce T1 contamination. Unlike turboFLASH in which the problem can be ameliorated by centric phase encoding, in RUFIS the T1-contamination affects the whole k-space. The simulation results confirmed that the underestimation of diffusion coefficient induced by T1 recovery can be up to -50% with commonly used acquisition parameters for T1 value of 600-1800 ms, in the range of physiological T1 values of brain tissue at 3T. The influence of acquisition parameters were compared, and results suggest that more accurate measurement can be conducted with lower b value and flip angle at the cost of reduced SNR. The phase cycling and subtraction scheme eliminates the error caused by T1 contamination and gives the most accurate results.

The time varying magnetic fields generate eddy currents in conduction structures such as the magnet and coils, which in turn induce unwanted magnetic fields and degrade image quality. In diffusion imaging, maximum gradient amplitudes are employed to achieve the desired diffusion weighting in minimum TE. Therefore, the effects of eddy current can be substantial and cause prominent image distortion. In conventional SS-EPI based DWI sequences, if the residual gradient field from eddy current exits during the EPI readout echo train, the reconstructed image will be degraded by shear, scaling and translation in the phase encoding direction [51], leading to misregistration problems when multi-directional diffusion images are combined to calculate tensors. In DWDE sequences, the effect of eddy current is presented as non-uniform image intensity arising from incomplete rephasing of transverse magnetization induced by spatially variant eddy current field [52].To alleviate this problem, Thomas and colleagues [25] proposed a method to take the square root of sum of squares of the two images acquired

with preparation module with phase-cycled tip-up pulse. For a diffusion sequence with standard spin echo EPI, the unipolar trapezoid diffusion gradient with the same polarity is placed symmetrically besides the refocusing RF pulse, thus adding up the residual eddy current. In a bipolar scheme described by Alexander et al [51] and Trudeau et al [53], the residual gradient is cancelled by utilizing bipolar gradient at the cost of reduced diffusion efficiency or increased minimum echo time. In another scheme to reduce the eddy current effect, Reese et al [54] designed the twice-refocused spin echo sequence that split the diffusion gradient into shorter pulses with alternating polarity by adding an additional RF refocusing pulse. Using this scheme, eddy current with single exponential decay can be nulled without compromising the diffusion efficiency, as well as allowing more flexibility in diffusion timing. In case of long time constant for eddy current decay, it is also possible to minimize the eddy current effect by adding prepulse. Previous studies have reported the use of prepulse in diffusion NMR spectroscopy [55] and MRI [51, 56] to partly compensate the eddy current effect. One of the advantages of such technique is that it causes no additional penalty on minimum echo time and diffusion efficiency. This technique was utilized in the current study and was sufficient to compensate for eddy current artifacts.

Two types of bulk motion could interfere with diffusion gradient: the general head motion and brain pulsation. Head motion can be characterized as rigid body motion, introducing global phase change and a shift [57, 58] with clear spatial dependence. Brain pulsation is the blood flow throughout the brain that synchronizes with cardiac cycle [59, 48]. It causes non-linear phase change across the image, resulting in piece-wise shift of the image data in different directions. In addition, the brain pulsation-induced displacement (phase incoherence) within one voxel could cause extra signal decay beyond the diffusion effect, biasing the diffusion measurement within that voxel. The residual phase gained from bulk motion in presence of diffusion gradients [60, 26] is not problematic for SS-EPI after the magnitude image is taken. For multi-shot techniques, however, phase error between different shot could largely degrade the image. When utilizing DWDE, the transverse magnetization is tipped up in the end and a spoiler gradient applied to remove remaining magnetization, therefore the residual phase error is converted in amplitude variation due to the incomplete refocus. If this is not compensated, in addition to the bias in estimating diffusion coefficient, the signal variation in k-space would cause ghosting artifact [60]. To overcome this problem, Thomas and Jeong [26, 25] reported a technique to phase cycle the last

tip-up pulse 90° out of phase, and take the square root of sum of squares (SRSS) of the two phase cycled images on voxel by voxel basis, producing an image that is not affected by motion induced phase error. Flow compensated diffusion weighting schemes have been developed by having gradient moment nulling. First order moment nulling [61] and second order gradient nulling [60] demonstrated a good solution to bulk motion effect in cardiac diffusion imaging. However, the use of moment nulling has a drawback of reducing diffusion efficiency in the same preparation time [62] especially for higher order moment nulling. The choice is to make a trade-off between bulk motion sensitivity and SNR. In the current study, we used both Stejskal-Tanner and flow-compensated diffusion scheme and compared image quality. However, although flow compensation did reduce majority of motion, it wasn't sufficient to produce artifact free diffusion images of brain. Higher orders of motion caused sever artifacts.

The proposed sequence has been validated on phantoms, and shown to accurately resolve the diffusion coefficients compared to diffusion weighted EPI. T1 recovery during readout period could heavily contaminate the desired diffusion contrast. By comparing the diffusion coefficient measured in samples with different T1 values, we can conclude that for T1 values shorter than 1000ms, it's necessary to compensate for T1 contamination to avoid errors in diffusion coefficient measurement. The sequence was also validated in a pineapple serving as an anisotropy phantom. Reasonable image quality and similar FA and MD values were obtained compared to diffusion weighted SS-EPI. The images from volunteer study are significantly deteriorated by various artifacts. Strip artifacts are observed in T2 weighted images as shown in Figure 3.6, which could possibly be caused by RF mismatch. However, those artifacts are not present in images acquired using the original T2 preparation block. There are several differences between the acquisition protocol of the original and modified T2 preparation module. First, the original T2 preparation consists of two RF refocusing pulses, which could significantly reduce the effects of field inhomogeneity. However, in the T2 weighted preparation we tailored to add diffusion gradients, only one RF refocusing pulse was utilized. Therefore, it is more sensitive to artifacts caused by field inhomogeneity. For future studies, twice-refocused spin echo [54] could be implemented to compensate for field inhomogeneity and eddy current artifacts. Second,the original T2 preparation used initial ramp in the radial readout as crusher, while modified T2 preparation didn't. There could be interference between the T2 prep crusher gradient and the radial readout, when the crusher

has opposite sign to the radial readout and with same integral. Using initial ramp as crusher can avoid this problem because the crusher has the same sign as radial readout. In addition, diffusion images produced by flow-compensated scheme were still severely affected by residual motion, indicating that flow compensation alone is not sufficient to overcome motion artifacts, and further steps are needed.

Chapter 4

Silent T1 and Proton Density Imaging Based on Interleaved RUFIS

This chapter introduces a volumetric, fast and silent approach for quantitative T1 and PD mapping, while producing multiple bias-field corrected T1 images at different TIs using IR prepared RUFIS. It was implemented by combing an interleaved radial trajectory design and reconstruction of unaliased images using subspace constraints. The approach was validated in phantom and healthy volunteers, the accuracy and repeatability of the method was demonstrated. The content of this chapter was published in *Physics in Medicine & Biology*, 2020 volume 65 [63].

4.1 Introduction

T1 imaging

High resolution T1-weighted (T1w) imaging is widely applied in neuro-scientific and clinical studies, such as demyelinating diseases (e.g. multiple sclerosis) [64], brain development and pediatric imaging [65], brain aging [66]. The most common way of generating T1w images is by inversion or saturation recovery prepared rapid gradient-echo or fast spin echo (FSE) sequences. Quantitative T1 mapping

would further increase the diagnostic value of the method, because it provides un-biased tissue characterization for evaluating pathology, and facilitates statistical modelling, multi-center and longitudinal studies [67]. The gold standard of quantitative T1 mapping is performed by inverting the longitudinal magnetization and then sampling the MR signal at multiple inversion times (TIs) along the exponential recovery curve, known as inversion recovery (IR) T1 mapping [68]. The method provides robust T1 quantification since it takes the inversion efficiency into account, but lengthy scanning time hinders its clinical application. Widely used alternative methods to speed up the scanning include look-locker (LL) and the variable flip angle (VFA) method [68]. However, the VFA method is highly sensitive to B1 errors, and requires careful consideration of the spoiling regimes, pulse sequence parameters and magnetization transfer effect [69, 70, 71], whereas the LL method presents a tradeoff between spatial and temporal resolution and scanning time especially for 3D imaging [72].

Dynamic imaging with radial trajectory

Radial imaging has wide clinical application due to its resilience to motion and undersampling artifacts. A recent study on pediatric abdominal imaging suggests that 3D radial outperforms its Cartesian counterpart due to motion insensitivity [65]. In addition, 3D imaging is free from non-perfect slice profiles compared to 2D imaging and provides isotropic resolution which has the advantage of being reformatted and viewed in different planes. Various radial trajectories have been proposed to improve the uniformity of readout distribution and sampling efficiency [73]. With each radial spoke, an equal amount of low and high spatial frequency data is collected to provide homogeneous image updates. This feature makes radial imaging well-suited for time-resolved, dynamic techniques which need to capture motion kinetics or contrast variations and have wide applications in angiography, functional MRI, dynamic contrast-enhanced imaging, cardiac imaging etc [74, 75]. These techniques require radial profiles designed to allow uniform k-space sampling in each time frame. Winkelmann et al. proposed an optimal radial profile based on the Golden Ratio, which yields a high flexibility in choosing an appropriate temporal resolution [75] and is later adapted by Ehses et al. for quantitative T1, T2 and proton density (PD) mapping using TrueFISP [76].

Acceleration techniques

Several methods have been developed to speed up dynamic MRI using reduced data acquisition and without significantly compromising image quality. These methods exploit data redundancy in dynamic MRI that the image series typically exhibit spatiotemporal correlations. Liang [77] proposed using partially separable functions to overcome the requirement of dense sampling at the Nyquist rate, therefore achieving high spatiotemporal resolution with sparsely sampled k-t space. The applications include fMRI, dynamic contrast-enhanced imaging and spectroscopic imaging. Tsao et al. [78] proposed a model-based approach called k-t BLAST/SENSE for reconstruction of undersampled k-t space. The aliasing artifact is resolved in Fourier reciprocal x-f space using signal covariance learned from low-resolution training data [79]. The method is widely applicable especially for the imaging of objects exhibiting quasiperiodic motion, such as heart, lung and abdomen. Based on k-t BLAST/SENSE, Pedersen et al. [80] proposed the k-t PCA method to further facilitate the reconstruction by constraining each temporal frequency to be a linear combination of the basis functions, predetermined by the training images using principal component analysis (PCA). Tamir et al. [81] applied low-dimensional temporal subspace constraints on dynamic FSE data with randomly shuffled view ordering, and reduced T2 blurring and generated multicontrast T2 weighted images at virtual echo times (TEs). These acceleration techniques are especially important for 3D imaging to achieve decent spatiotemporal resolution.

Acoustic noise reduction

The acoustic noise originating from the imaging gradient can be up to 130 dB at 3T. This causes patients discomfort, anxiety and even hearing loss, limiting the use of MRI especially in pediatric imaging, patients with hyperacusis etc [5]. The high acoustic noise raises more concern in fetal examinations, as studies have revealed vulnerability of the human fetus to excessive acoustic noise. Exposure of the fetus to high intensity of noise could cause hearing loss and decreased birth weight [82, 13], while external noise protections (ear plugs) are not applicable. In addition, even with external noise protections, exposure to acoustic noise during 3T MRI scan can cause altered cochlear function and temporary increase of hearing threshold [83, 84]. It has been shown that improved patients comfort during MRI scanning, mainly by reducing noise and confined sensation, is essential to

reduce mental stress and claustrophobia occurrence during examination [85, 86]. Therefore, silence is a desired feature and and healthcare providers endeavor to develop noise reduction techniques, including the use of sound-attenuating materials, Lorentz force balancing, rotating DC gradient, active vibration control, optimization of MRI sequences [9, 5] and minimizing gradient switching [38]. Sequence optimization methods can be incorporated into any existing MRI system and achieve noise reduction of 10-20 dBA [5, 13], thus they are more commonly used by various manufacturers. Previous studies explored the use of silent T1w sequences for intracranial tumor patients and other clinical population [87, 88, 89]. Those sequences were achieved by using the magnetization prepared rotating ultrafast imaging sequence (RUFIS) [38], a 3D radial technique in which the frequency encoding gradient is gradually reoriented with repetition. Therefore, it has a lower demand on hardware in terms of slew rate and leads to nearly inaudible scanning. These studies have reported comparable efficiency of silent T1w scanning in terms of signal/contrast to noise ratio and lesion conspicuity rated by radiologists, suggesting they can be used as viable quiet alternatives for conventional T1w imaging [87, 88, 89].

Aim and contribution

The aim of this study was to develop a volumetric, fast and silent approach for high resolution quantitative T1 and PD mapping. The main contribution includes: (i) interleaved RUFIS trajectory design to enable uniform undersampling in each time frame, (ii) reconstruction of unaliased images using subspace constraints and (iii) produce quantitative maps and multiple bias-field corrected T1 images at different TIs. The approach was validated in phantom and healthy volunteers, the accuracy and repeatability of the method was demonstrated.

4.2 Methods

4.2.1 Sequence and undersampling strategy

The IR prepared RUFIS sequence is depicted in Figure 4.1. The magnetization is prepared by an adiabatic inversion pulse followed by RUFIS readout, which consists of repetitive small flip angle α excitations and short repetition time (TR).
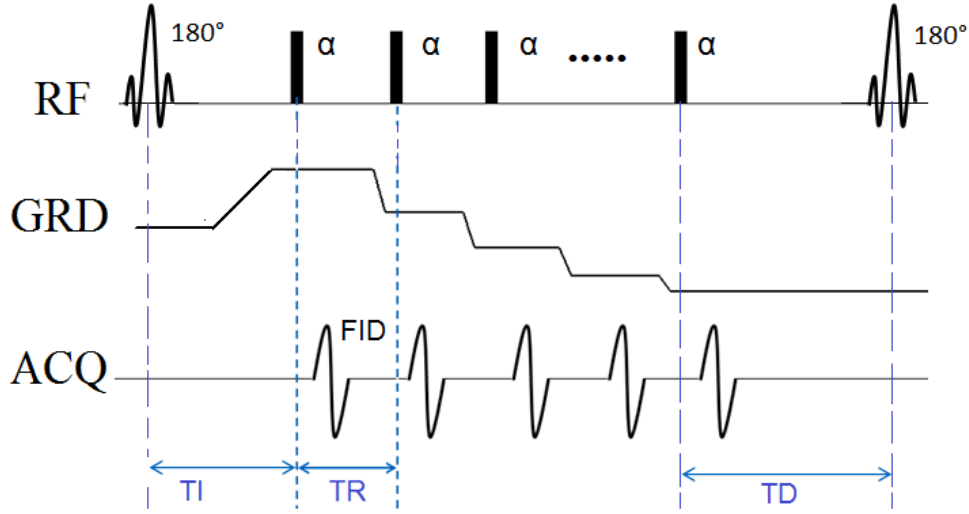
Figure 4.1: Diagram of the IR prepared RUFIS. After the adiabatic inversion preparation, a train of low flip angle α excitation was applied with short TR. The gradient was active during RF excitation and was gradually reoriented with each TR. A waiting time (TD) was placed between consecutive interleaves to allow for free magnetization recovery.

A waiting time (TD) is placed between consecutive interleaves to allow for magnetization recovery. The signal model for original IR-snapshot-FLASH imaging was designed for Cartesian trajectory [90], which assumes that the contrast is defined at the time point where the k-space center is acquired. When using radial trajectories, the center of k-space is constantly updated by each projection, making it possible to sample signal evolution along the temporal dimension.

Unlike standard sequences, RUFIS utilizes nonselective hard pulse excitations in presence of the encoding gradients, immediately followed by 3D radial center-out data acquisition, resulting in nominal zero TE. After data acquisition in each TR, signal spoiling is achieved by the combination of gradient ramping before next excitation and RF phase cycling. To achieve uniform excitation in the FOV, the RF excitation bandwidth must be wide enough to cover the imaging bandwidth spanned by the gradient. The typical B1 amplitudes ($\sim 15\mu T$) on clinical MR scanners limits the flip angle to maximum only a few degrees. Small and smooth gradient update between successive repetitions leads to robustness against eddy currents and silent scanning. Because of the small flip angle and short TR, the original RUFIS is PD weighted.

To achieve high spatial and temporal resolution, the data acquisition is conducted in an interleaved manner. Data segments with similar TI (adjacent posi-

tion in the readout) from different interleaves are grouped together to generate undersampled images. The effective TI for each time frame is defined at the center of the acquisition window. In the work of Wong and Roos [73], an interleaved radial trajectory was designed with the end point of each radial spokes uniformly distributed on a surface of sphere, and each interleave was rotated from one another. The expression for x, y, z components of the interleaved trajectory are as follows:

$$\begin{cases} z(n) = \dfrac{2n - N - 1}{N} \\ x(n) = \cos(\sqrt{\dfrac{N\pi}{M}} \sin^{-1} z(n) + \dfrac{2m\pi}{M})\sqrt{1 - z^2(n)} \\ y(n) = \sin(\sqrt{\dfrac{N\pi}{M}} \sin^{-1} z(n) + \dfrac{2m\pi}{M})\sqrt{1 - z^2(n)} \end{cases} \quad (4.1)$$

where M is the number of interleaves, N is the number of spokes per interleave, $n = 1, 2, \ldots, N$ and $m = 1, 2, \ldots, M$.

The current work needs a trajectory where: (i) each time frame contains data sample roughly uniform across 3D K-space and (ii) the step-wise gradient update should be small enough to maintain the silent feature of the sequence. We adapted the trajectory in ref [73] to meet the above requirements by resorting the trajectory interleaves into each time frame. First, we decide the total number of spokes N, the number of time frames N_{TI} and another parameter G. The trajectory is generated according to Eq (4.1) with interleave number $M = \frac{N_{TI}}{G}$. Then this trajectory is rearranged by assigning every G^{th} spoke into a specific time frame. In this study, we used $N_{TI} = 32$ and $G = 16$. The undersampling strategy and trajectory design are illustrated in Figure 4.2.

4.2.2 Signal model and temporal subspace

For simplicity, we consider longitudinal magnetization in a single voxel, since the measured signal is proportional to longitudinal magnetization by a factor of $sin\alpha$. The signal after applying $n^{th}\alpha$ pulse can be described as

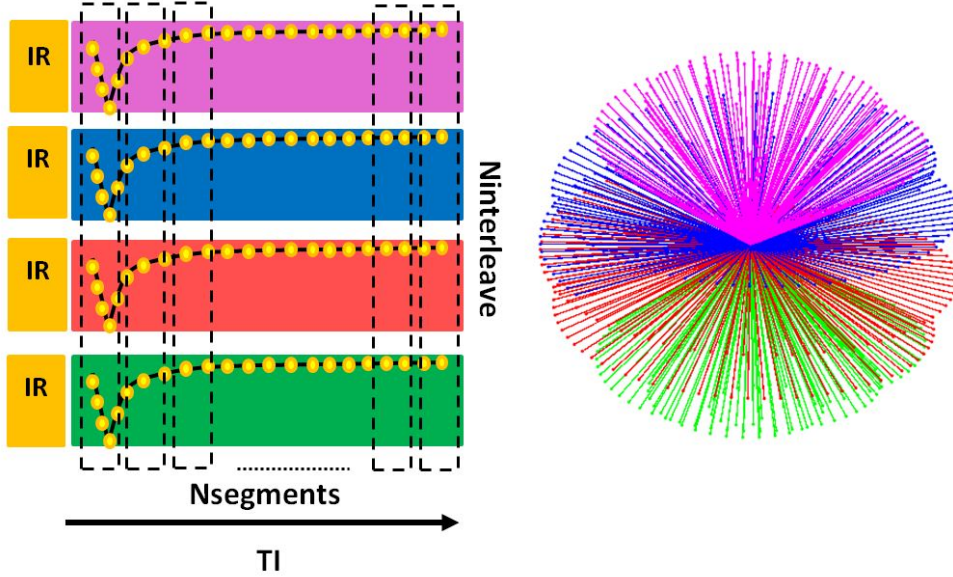$$M_n = M_{ss} - (M_{ss} - M_{t0})(E_{TR} \cos \alpha)^n \quad (4.2)$$

Figure 4.2: Demonstration of undersampling strategy. Data was segmented along the readout (as illustrated in the dashed boxes on the left), and segments acquired at the same TI were grouped together to generate undersampled images. On the right is a representation of the k-space trajectory at one effective TI, which was first generated according to Eq. (4.1), and then realigned into segments with the same effective TI on different interleaves (segments illustrated in dashed boxes, and colors correspond to radial spokes allocated to different interleaves).

where $E_{TR} = \exp(-TR/T1)$, M_{ss} is the steady sate signal given by

$$M_{ss} = \rho \frac{1 - E_{TR}}{1 - E_{TR} \cos \alpha} \tag{4.3}$$

Where ρ is the PD, M_{t0} is the initial signal at the beginning of acquisition,

$$M_{t0} = \rho \frac{1 - E_{TI} - \beta E_{TI}(1 - E_T D) - M_{ss}[1 - (E_{TR} \cos \alpha)^N]\beta E_{TI} E_{TD}}{1 + (E_{TR} \cos \alpha)^N \beta E_{TI} E_{TD}} \tag{4.4}$$

where $E_{TI} = \exp(-TI/T1)$, $E_{TD} = \exp(-TD/T1)$, β is the inversion efficiency and N is the total number of α pulses applied. It should be noted that the model assumes perfect RF pulses and negligible duration of α pulse, which is not achieved in real acquisitions.

The signal curve observed in the IR-RUFIS experiment is a function of the tissue parameters (T1, PD) and acquisition parameters (IR pulse and readout flip angle). Figure 4.3 shows the example of the signal evolution for different T1 values. The signal curves of different T1 values follow similar trends, which implies that they can be represented by low-rank subspace. Eq. (4.2) can be
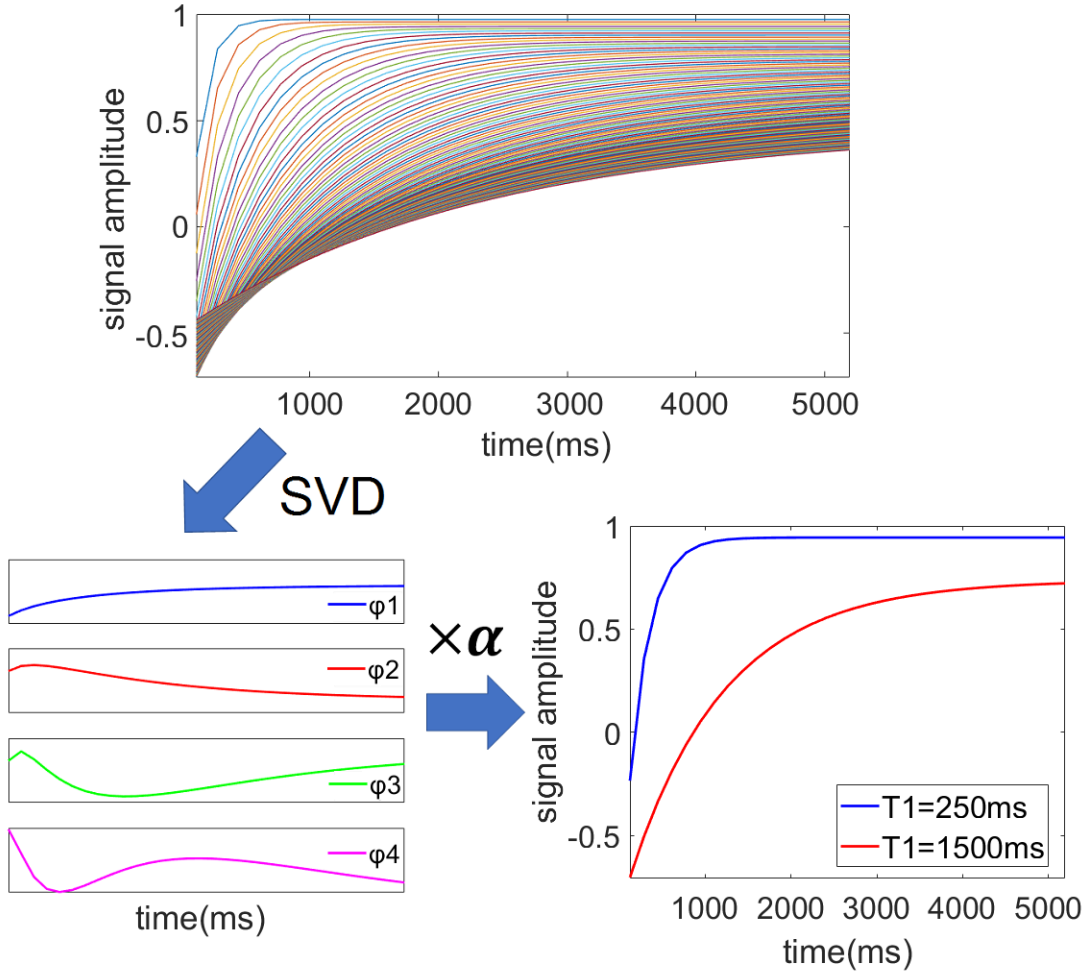
Figure 4.3: Use of temporal subspace to approximate the real signal evolution:The ensemble of calculated signal evolution (middle) was decomposed through SVD. The temporal subspace (bottom left) consists of the first four singular vectors, which were linearly combined to approximate signal evolution (bottom right).

used to generate the dictionary $\mathbf{M}$ for T1 values of interest, where each column represents the signal evolution for a particular T1 value. By conducting singular value decomposition (SVD) of the dictionary, the subspace $\mathbf{\Phi}_K$ can be defined as the first K right singular vectors, and used to approximate the real signal:

$$\hat{\mathbf{M}} = \mathbf{\Phi}_K \mathbf{\Phi}_K^H \mathbf{M} = \mathbf{\Phi}_K \alpha \tag{4.5}$$

Where the modeled signal $\hat{\mathbf{M}}$ can be described by the temporal basis coefficients α. Figure 4.3 illustrates the use of subspace to approximate signal evolution. The size of the subspace is chosen as a trade-off between noise amplifi-
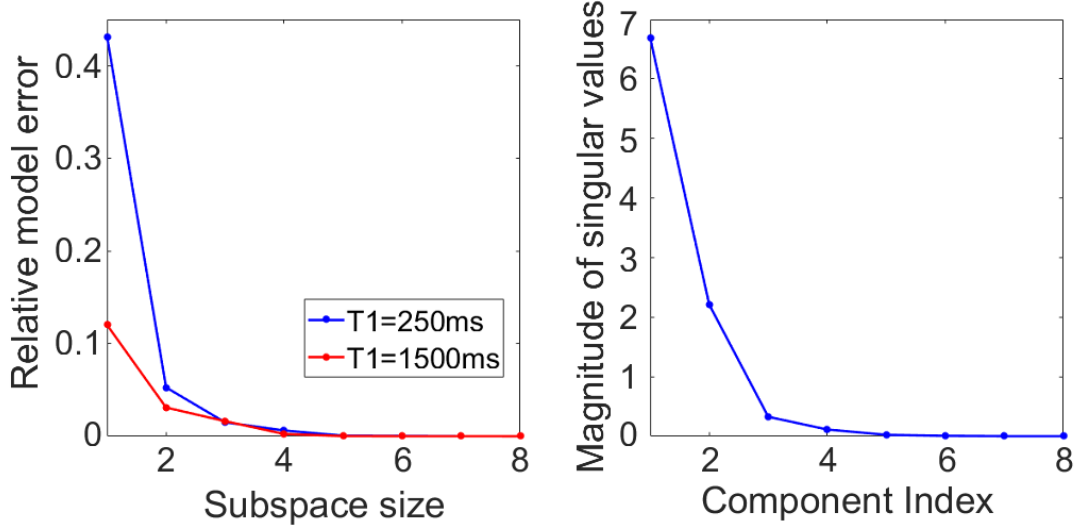
Figure 4.4: The relative modeling error with different subspace size.

cation and modeling error, as the noise in a subspace-constrained reconstruction increases linearly with the subspace size K [81]. The relative modeling errors for different subspace sizes are defined using the Frobenius norm

$$F = \frac{\|\mathbf{\Phi}_K \mathbf{\Phi}_K^H \mathbf{M} - \mathbf{M}\|_2}{\|\mathbf{M}\|_2} \tag{4.6}$$

and shown in Figure 4.4.

4.2.3 Data acquisition and acoustic noise measurement

All experiments were conducted on a GE 3T MR750w scanner with a 12-channel GEM head array coil (GE Healthcare, Waukesha, WI). The general acquisition parameters for phantom and in vivo experiments were as follows: flip angle=2°, readout bandwidth=±15.6 kHz; The data acquisition began 40 ms after the IR pulse and lasted for approximately 5000 ms to acquire 2048 radial spokes for each interleave. Four dummy cycles were performed to reach steady state, followed by 32 interleaves of actual data acquisition. A waiting time of 1000 ms was applied between consecutive interleaves to allow signal recovery.

A phantom consisting of samples with different T1 values (DiagnosticSonar, Livingston, UK) was used in this study. The T1 values of the phantom ranged from 300 to 1565 ms, covering the range of physiological T1 values expected in

brain white matter (WM) and gray matter (GM). Field of view (FOV)=20.1 cm, isotropic resolution=1.5 mm, and TR=2.46 ms. For comparison, the center slice of the phantom was also measured with a Cartesian inversion-recovery spin-echo (IR-SE) sequence at 25 different TIs ranging from 50 ms to 4000 ms, and TR = 13 s which is sufficient long to allow for a near-complete recovery. The reference T1 value was assessed by a three-parameter fit of the acquired images.

Six healthy volunteers, 4 males and 2 females, ages ranged from 28-33 years, participated in the data acquisition. The current study was approved by the local ethnic board and prior informed consents were obtained. FOV=18.5-21 cm, isotropic resolution=1.5 mm, TR=2.30-2.56 ms, and scanning time 3:30 minutes. Two scans of each subjects were acquired to test the repeatability of the proposed method.

Acoustic noise was measured using a Bruel&Kjaer sound level meter (Type 2250) equipped with MR compatible microphone (type 4189). Calibration of sound level meter was conducted before the measurement using a 94 dB and 114 dB sound source (Calibrator Type 4231). The acoustic noise was measured in 2 minutes' duration for the in-bore ambient background, the proposed silent sequence and and a IR prepared fast spoiled gradient echo sequence (acquisition parameter: TR/TE = 7.6 ms/2.8 ms, TI = 900 ms, in-plane resolution = 1.5 × 1.5 mm, slice thickness = 2 mm) as comparison. The C-weighted peak (LCpeak, dBC) and the A-weighted average (LAeq, dBA) sound pressure levels (SPL) were recorded. The microphone was placed in-bore at scanner isocenter inside the head coil. RF transmit was disabled during the measurement to avoid damage to the microphone.

4.2.4 Reconstruction and data analysis

The radial k-space data was first segmented into time frames and then interpolated into a Cartesian grid by convolving the spokes by the commonly used Kaiser Bessel kernel. A dictionary was generated by Eq. (4.2) using T1 values from 100 ms to 5000 ms with 1 ms spacing, from which the temporal basis was calculated. The subspace size was chosen based on the largest allowed modelling error described in Eq. (4.6). In this study, we chose subspace size K=4, which makes the relative modelling error less than 1% for all T1 values used in the simulation. The k-space data was projected onto the subspace before inverse Fourier
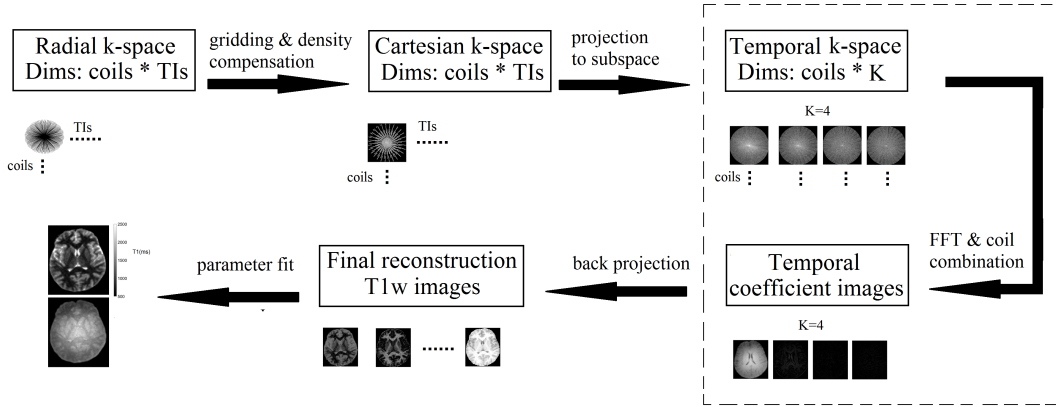
Figure 4.5: Overview of the reconstruction process. 1. Undersampled radial k-space data in each time frame was interpolated into Cartesian grid and non-uniform sampling density was compensated. 2. K-space data time series were projected onto the temporal subspace, which was calculated from Bloch simulation. In the current study, number of time frames is 32 and subspace size K is 4. 3. Inverse fast Fourier transform, and coil combination were conducted in the temporal subspace to generate K coefficient images. 4. Temporal coefficient images were projected back to the original time series. 5. Quantitative T1 and PD maps were obtained by fitting the reconstructed T1w images.

transform to obtain K temporal coefficient images, which were used to estimate the coil sensitivity map. After coil combination, the temporal coefficient images were projected back to the original time series. The reconstruction process is illustrated in figure 4.5.

The quantitative T1 map was computed by a pattern recognition algorithm [91] previously used in magnetic resonance fingerprinting, which compares the observed signal to each of the entries in the dictionary and finds the one with the maximum inner product as the best match. Then the T1 value of that entry is retrieved using the lookup table. The PD of each voxel was computed as the scaling factor between the observed signal and the dictionary entry. We employed a bias-filed correction method based on image ratio [92] to improve T1 contrast. The T1w images were divided by the PD map to eliminate receive RF coil sensitivity B_1^- and PD contrast. The effectiveness of the method was evaluated by comparing whole-brain intensity histograms of T1w images before and after the correction.

The accuracy of the proposed method was examined in the phantom study by comparing to the gold-standard IR-SE sequence. The mean and standard deviations of T1 values were extracted from manually defined regions of interest (ROIs) in each sample. The Pearson correlation coefficient was calculated against

the values obtained from IR-SE. The coefficients of variation (CVs) of the two scans were calculated to test the repeatability of the proposed method.

Subject-specific templates were created by registering the second scan to the first scan of each subject by rigid transformation using the MATLAB image processing toolbox. Brain extraction was conducted on composite T1w image using BET (FMRIB Software Library: www.fmrib.ox.ac.uk/fsl) [93] and were visually inspected to ensure the quality. The mask was applied to T1 and PD maps. To visualize the distribution of T1 values, T1 histograms of a single subject and pooled histogram from all the subjects were generated from the whole-brain volume. The WM and GM T1 peaks were calculated after performing probability density estimate with normal distribution kernel function [94]. The mean and standard deviations of T1 values were extracted from WM and GM ROIs, including bilateral putamen, caudate, internal capsule and posterior WM. The results of the volunteer study were compared to literature values, and CVs were calculated.

4.3 Results

4.3.1 Phantom Study

The results from the phantom experiment and repeatability test are shown in Table 4.1. The effect of enforcing subspace constraint on signal evolution is shown in Figure 4.6. T1 values measured with the proposed method are plotted against reference T1 values derived from the IR-SE experiment in Figure 4.7. The proposed method showed high accuracy and only small deviation from the results of IR-SE, with correlation coefficient $R^2 = 0.9976$. The sample with the smallest T1 value showed the largest percentage difference compared to IR-SE. CVs ranged from 0.09% to 0.83%. T2 values of sample no. 2 and no. 3 were 130.45 ms and 41.90 ms, respectively, calibrated using spin echo. Note that for these two samples, the accuracy of the T1 measurement was not influenced by vastly different T2 values.
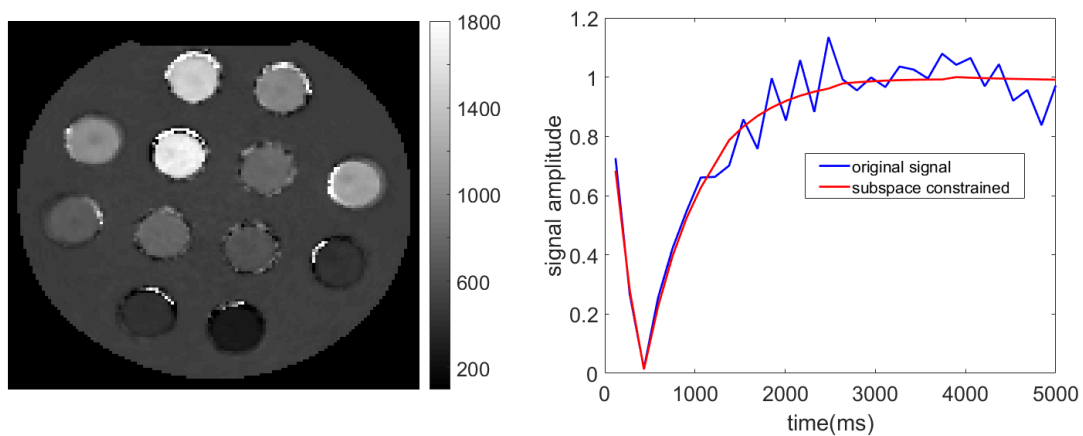
Figure 4.6: Results of the T1 phantom study. Left: T1 map of the phantom. Right: Comparison of the MR signal before (blue) and after (red) applying temporal subspace constraint
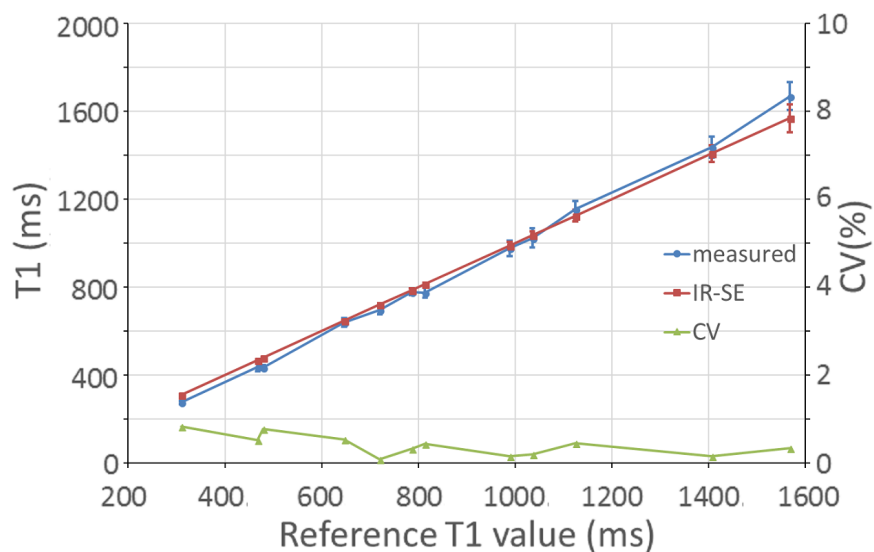

Figure 4.7: Results of the phantom study. T1 values measured by the proposed method (blue) and IR-SE (red). CVs from the repeatability study are shown in green.

**Table 4.1:** T1 measurements and repeatability in phantom experiment

Sample	1	2	3	4	5	6
IR-SE	310± 1	467± 1	479± 1	647± 3	720± 5	786± 7
Scan1	275± 7	436± 19	434± 10	638± 20	695± 18	777± 15
Scan2	272± 8	434± 18	430± 11	635± 19	695± 17	775± 16
Difference (%)	11.84	6.86	9.81	1.52	3.51	1.28
CV (%)	0.83	0.52	0.77	0.54	0.09	0.32
Sample	7	8	9	10	11	12
IR-SE	813± 5	989± 18	1035± 18	1124± 27	1407± 37	1568± 63
Scan1	774± 22	976± 35	1023± 43	1154± 38	1437± 48	1668± 63
Scan2	777± 22	978± 36	1025± 43	1149± 36	1435± 46	1662± 63
Difference (%)	4.69	1.21	1.10	2.42	2.08	6.22
CV (%)	0.43	0.15	0.19	0.45	0.16	0.34

## 4.3.2   In-vivo Parameter Mapping

The axial, sagittal and coronal T1 and PD maps from in vivo imaging and the placements of GM and WM ROIs are shown in Figures 4.8. The volumetric T1 and PD maps with isotropic resolution can be reformatted into different orientations. Table 4.2 summarizes ROI analysis results for the in vivo experiment. Mean T1 values from WM and GM ROIs of all subjects ranged from 702 ms to 767 ms and 1033 ms to 1276 ms, respectively, in accordance with literature values [95, 96]. The PD ratios between WM and GM were calculated by comparing the combined WM and GM ROIs and ranged from 0.81 to 0.86 for all subjects, which were also consistent with literature values [97].The quantitative in vivo results exhibit high repeatability. For ROI analysis, the mean and standard deviations of CVs calculated across all subjects and ROIs were 0.40%±0.37% (max/min=1.55%/0.01%). Figure 4.9 shows the whole-brain T1 histogram from a single subject the pooled histogram from all subjects. The T1 value peaks of GM and WM can be clearly delineated for all subjects, and the peak values are reported in Table 4.3. For histogram analysis of WM and GM peak values, the mean and standard deviations of CVs across all subjects were 0.58%±0.68% (max/min=2.30%/0.08%).

4.3.3   Multiple T1 Images with Bias-field Correction

Figure 4.10a shows the representative images with different T1 contrast after bias-field correction, reconstructed at effective TIs ranging from 118 ms to 5000
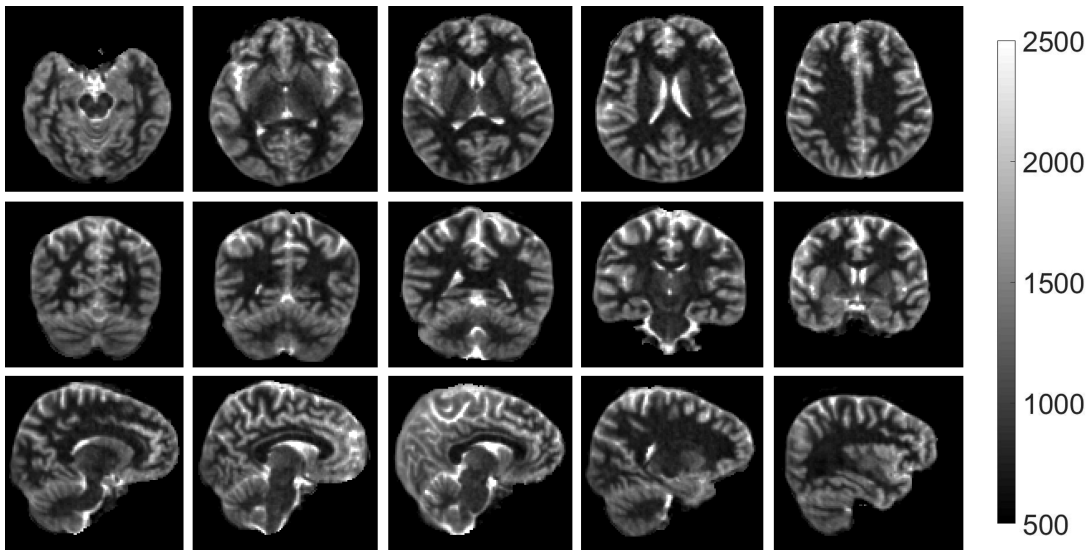
(a) Representative slices of T1 maps in axial, coronal and sagittal plane
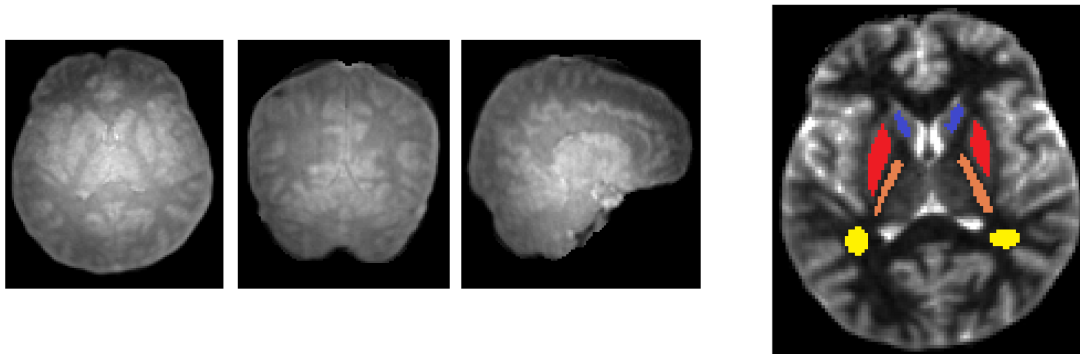
(b) PD maps and ROIs placement on GM and WM. ROIs of left and right putamen, caudate, posterior WM and internal capsule are indicated in red, blue, yellow and orange, respectively. The T1 and PD values from these ROIs are shown in Table 4.2.

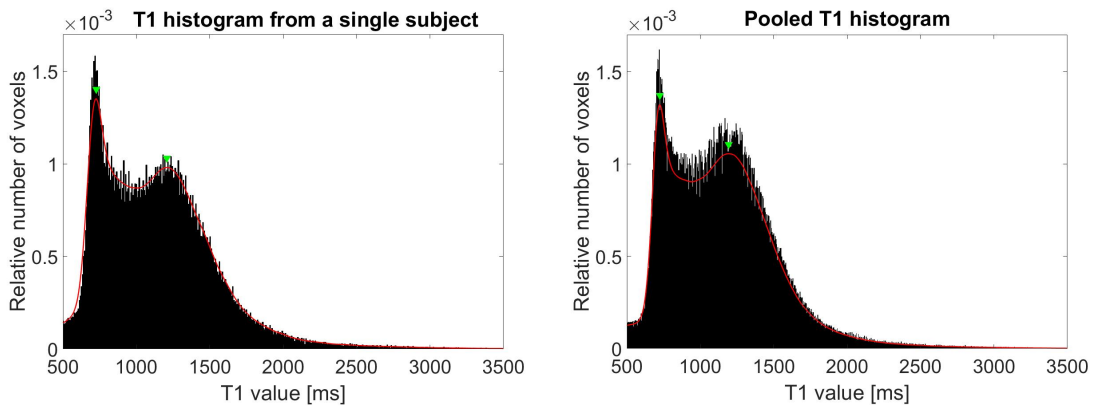**Figure 4.8:** Quantitative maps of the volunteer study

Figure 4.9: Whole-brain histogram of the T1 map from a single subject (left) and all subjects (right). The green arrow points out peaks of T1 values from WM and GM.

Table 4.2: T1 and PD measurements for the selected ROIs in repeated volunteer experiments.

Volunteer		GM T1 value				WM T1 value				PD ratio
		L-Pu	R-Pu	L-Cd	R-Cd	L-PWM	R-PWM	L-IC	R-IC	
	Scan1	1041±65	1069±58	1192±70	1148±77	703±37	725±31	760±34	761±43	
1	Scan2	1037±64	1068±57	1199±67	1147±83	702±31	723±29	763±29	761±46	0.86
	CV(%)	0.28	0.05	0.38	0.04	0.04	0.22	0.28	0.03	
	Scan1	1068±44	1031±47	1179±86	1215±58	748±34	718±34	763±31	744±40	
2	Scan2	1045±35	1020±43	1179±82	1199±56	745±32	719±37	767±26	748±37	0.83
	CV(%)	1.55	0.80	0.01	0.96	0.23	0.04	0.40	0.34	
	Scan1	1075±56	1060±65	1216±47	1194±60	725±32	712±28	758±39	753±26	
3	Scan2	1072±67	1038±61	1235±78	1193±48	726±26	712±27	766±30	746±28	0.81
	CV(%)	0.20	1.45	1.06	0.07	0.14	0.05	0.66	0.66	
	Scan1	1077±52	1084±57	1197±65	1257±65	716±26	716±26	741±41	747±33	
4	Scan2	1072±47	1080±53	1212±63	1260±75	717±21	716±21	746±37	751±28	0.84
	CV(%)	0.35	0.29	0.83	0.12	0.08	0.02	0.47	0.41	
	Scan1	1033±60	1042±62	1277±50	1224±67	726±61	710±31	742±28	718±40	
5	Scan2	1031±57	1040±57	1267±50	1216±44	735±54	713±24	743±31	717±36	0.83
	CV(%)	0.17	0.10	0.53	0.45	0.93	0.26	0.08	0.08	
	Scan1	1090±69	1076±60	1207±69	1219±41	718±22	725±26	730±43	744±40	
6	Scan2	1082±70	1075±60	1196±63	1209±36	721±19	721±20	737±35	736±36	0.83
	CV(%)	0.49	0.05	0.66	0.60	0.33	0.40	0.68	0.78	

Table 4.3: T1 value peaks of GM and WM in whole-brain histogram analysis.

Volunteer		1	2	3	4	5	6
	Scan1	1205	1183	1168	1182	966	1207
GM	Scan2	1204	1174	1190	1163	935	1204
	CV(%)	0.09	0.49	1.32	1.18	2.30	0.21
	Scan1	720	724	745	733	742	727
WM	Scan2	719	725	743	730	746	729
	CV(%)	0.15	0.08	0.16	0.36	0.39	0.23

ms. With the increasing effective TI from left to right, sequential nulling of WM, GM and CSF can be observed. Whole-brain intensity histograms of T1w images before and after bias-field correction are shown in Figure 4.10b. The correction method significantly improved the separation between GM and WM peaks, indicating a better tissue contrast.

4.3.4   Acoustic Noise Measurement

The LAeq and LCpeak values of in-bore ambient background were 72.2 dBA and 95.3 dBC; for the IR-RUFIS sequence, they were 74.8 dBA, 95.7 dBC; for the IR prepared fast spoiled gradient echo sequence which is widely used for T1 imaging, the LAeq was 104.9 dBA. The A-weighting is the most common frequency weighting which best resembles the loudness perceived by the human

ear. The C-weighting is used in peak SPL measurements for evaluating very high-level or low-frequency sounds. Compared to in-bore ambient noise, the IR-RUFIS sequence caused LAeq and LCpeak acoustic noise levels to increase only 2.6 dBA and 0.4 dBC, respectively. Compared to IR gradient echo sequence, the proposed sequence achieved 30.1 dBA acoustic noise reduction, which corresponds to 97% reduction in sound pressure, since the acoustic measurement is in logarithmic scale.

4.4 Discussion

Main Contributions

In the current study, we proposed a quantitative T1 and PD mapping method based on interleaved IR-RUFIS and temporal subspace constraint. The method is efficient in generating volumetric T1 and PD maps in clinically relevant resolution and time (whole-brain 1.5 mm isotropic resolution in 3.5 min) while producing multiple time-resolved multicontrast T1w images. T1 values obtained by the proposed method were compared with IR-SE sequence in phantom studies where the correlation coefficient $R^2 = 0.9976$. CVs ranged from 0.09% to 0.83% in repeatability test. In addition, the sequence is literally silent with the averaged SPL only increasing by 2.6 dBA compared to in-bore background. This feature could greatly improve patient comfort, increase MRI applications in pediatric and fetal imaging, and for people with tinnitus or hyperacusis. It is also worth noting that the accuracy of the current T1 mapping method was not influenced by T2 values. As demonstrated in the phantom results of sample no. 2 and no. 3, the T1 measurements remain accurate despite vast difference in T2 values. Previous studies reported T2 dependent error of SSFP based methods like MOLLI: T1 maps have T2 weighting, causing increased underestimation of T1 values at shorter T2 [98, 99].

Accuracy and Repeatability

For in vivo validation, T1 values extracted from WM and GM ROIs are consistent with literature values. The T1 values in the WM range from 702 ms to 767 ms, and in GM 1033 ms to 1276 ms. The whole-brain T1 histogram is characterized
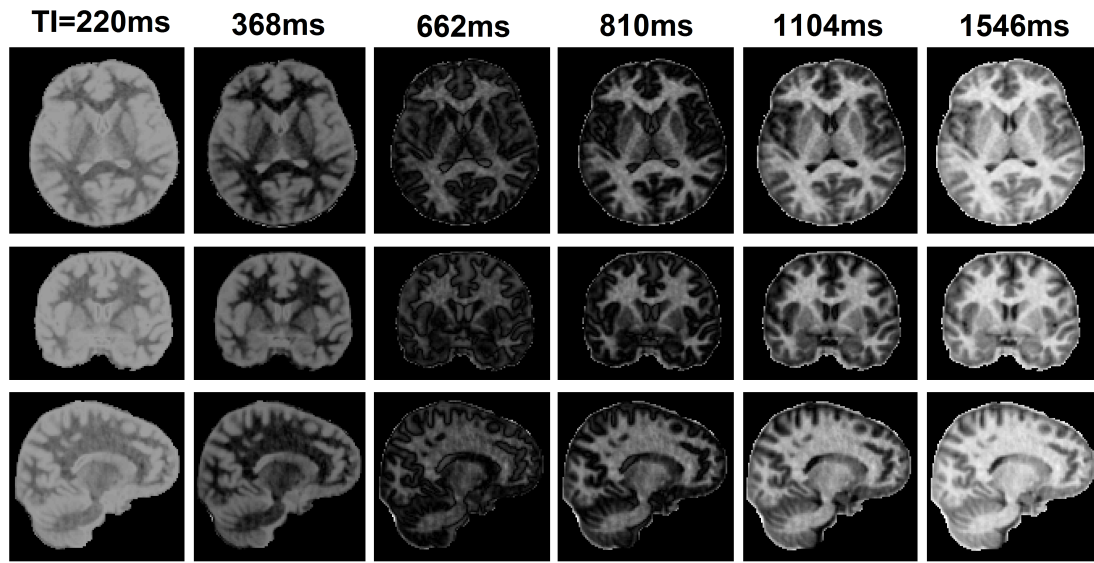
(a) T1w images acquired at different TIs as indicated at the top of each image column. The nulling point of WM, GM and CSF can be observed in columns 2, 3 and 5, respectively.
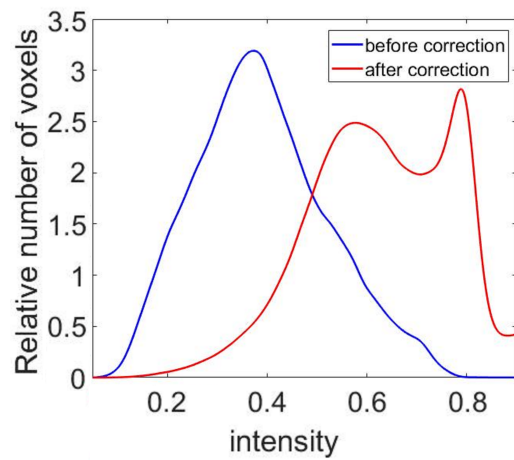
(b) Comparison of whole-brain intensity histogram of T1w images before (blue) and after (red) bias-field correction. The separation of WM and GM peaks is significantly improved after correction.

Figure 4.10: T1w images from volunteer study

by a distinct and sharp peak representing the T1 values found in WM, and a broader peak on the right representing T1 values from GM, extending into larger T1 values from CSF, which is consistent with previous studies [].(Van Walderveen et al 2003, Stikov et al 2015). The scan-rescan tests of the six subjects showed repeatability of CVs ranged from 0.01% to 2.30%. The WM histogram peaks facilitate comparison by providing a distinguishable reference, as previous studies confirmed it to be a biomarker for multiple sclerosis (MS). Compared to normal subjects, the WM T1 histogram peak in MS patients is broader, with lower peak amplitude and shifted towards larger T1 values [100, 68] because of T1 prolongation in normal appearing WM. It can be noted that the CSF peak is not distinctly visible on the T1 histogram in Figure 4.9. This is possibly caused by the partial volume averaging effect [100] or underestimation of long T1 values due to reduced dynamic range. We expect the measurement of long T1 values samples, such as CSF, to be more accurate with a longer acquisition window or waiting time.

Some studies [101, 81] have proposed methods to reconstruct multiple images with different contrast along the relaxation curve in a single exam. In comparison to conventional methods, which only acquire a single contrast at the selected time point, these additional images can provide tissue dynamic information and enable subject-specific retrospective selection of the optimized contrast for diagnosis or segmentation purposes. In the current study, 32 T1w images with TIs ranging from 118 ms to 5000 ms were reconstructed, and nulling points of GM, WM and CSF can be observed in the sequential images. However, the B_1^- inhomogeneity impairs the image quality and intrinsic PD weighting tend to reduce the contrast in T1w images. These factors were eliminated using the technique described in Van de Moortele et al [92]. From the whole-brain intensity histogram of the T1w images after correction, the clear separation between WM and GM peaks indicate that the method achieves a good outcome in bias-field cancellation. The resulting purely T1w images have better anatomical quality and brain tissue differentiation, which are more suitable for segmentation, voxel-based morphometry and diagnosis applications [92].

Quantitative MRI aims to provide absolute measures to overcome bias between scans and sites. However, most T1 mapping literatures are very consistent within studies but not across studies [68]. Inter-study discrepancies could be caused by a variety of reasons: the fitting routines, different study populations (both gender and age can affect T1) as well as the choice of sequences and param-

eters. Stikov et al [68] examined the three most common T1 mapping methods: IR, Look-Locker and VFA. They found excellent agreement between the three methods in phantom experiments. But for in vivo imaging, the Look-Locker underestimates and VFA overestimates T1 values, with the peak of WM T1 histogram varies by more than 30%. These variations could be results of incomplete spoiling and B1 inaccuracy. Even when using the gold standard IR protocol, there are large variations of reported WM T1 values due to different experiment settings. Despite these inter-study discrepancies which make standardization difficult, methods with high repeatability are still reliable and sensitive for detection of changes between groups [100, 68]. Poor scan-rescan repeatability would undermine the comparability of data, as the measurement variations could obscure pathological changes [102]. In the current study, the proposed method exhibits high repeatability in both phantom and in vivo experiments, which is advantageous for clinical application and longitudinal studies.

Limitations

There are several sources of error to consider. T1 values of CSF were underestimated in the volunteer study, as discussed above. In the phantom study, the sample with the smallest T1 value showed the largest percentage error compared to the gold-standard method. The signal recovery is more rapid with a small T1 value; thus, it is more sensitive to the averaging effect within the time frame. We expect to improve the accuracy of small T1 value measurements by using shorter time frames. In addition, when a perfect inversion and excitation RF pulse are not achieved, the signal deviates from the assumed model and introduces bias into the T1 mapping. T1 values can be underestimated with incomplete inversion pulse and overestimated when the effective flip angle of excitation pulse is smaller than the nominal flip angle. To account for RF transmit field inhomogeneity, some studies employ B1 mapping methods [92, 68]. In the gold standard IR-SE method, the inversion efficiency is considered in the 3-parameter fitting. In the current study, we did not incorporate B_1^+ errors into the model and fitting, because it will greatly increase the dictionary size and result in unstable estimation of T1 values. Although the accuracy is high for T1 values of interest in the brain, B_1^+ errors should be considered in future studies to reduce systematic error.

Future Work

Both imaging parameters and reconstruction pipeline of the proposed method provide room for improvement. As a future extension for the current work, other contrasts can be acquired by replacing the inversion recovery with other preparation modules, and the same trajectory can be used to facilitate acceleration. Like in some studies [103, 104], IR and T2/diffusion preparation were applied to reconstruct multi-contrast images. In addition, the proposed method can also be combined with long T2 suppression technique to characterize tissue with short-T2 value, such as tendon or myelin. Impairment of myelin integrity is the biomarker of numerous inflammatory and neurodegenerative diseases. Therefore, imaging of myelin has been of critical importance in neuroradiology research, with various applications such as MS and leukoencephalopathy. Conventional T1w images have been used in myelin imaging, but with low sensitivity and specificity [105]. Larson [106] proposed a method based on ultrashort echo time (UTE) sequence with long-T2 suppression, and visualization of short-T2 component in UTE brain images was significantly improved. With long T2 suppression technique, the current zero TE based method can also be applied for myelin imaging.

Chapter 5

Summary and outlook

The techniques proposed in the current thesis contributes to the areas of image acquisition, reconstruction and quantification of diffusion, T1 and proton-density weighted imaging. Specifically, strategies to ameliorate loud acoustic noise in MRI acquisition process are addressed. High acoustic noise is a major stress factor in MRI scans and may cause subjects hearing loss.The proposed silent acquisition and reconstruction methods were validated in phantom and volunteer studies. Accuracy and repeatability of the proposed methods were evaluated by comparing to standard methods and literature values.

In chapter 2, a silent version of Echo Planar Imaging (EPI) sequence was implemented by switching the oscillating readout gradients from trapezoidal to sinusoidal shape. The spectrum of sinusoidal gradient was band-limited and the output acoustic noise was reduced by shifting the main frequency component to avoid the peak of scanner frequency response functions. The method was validated in phantom and achieved 5 dBA reduction of acoustic noise with maintained image quality. For future studies, the scanner frequency response functions of each physical gradient axis can be explicitly measured to further optimize the sequence . In addition, crusher gradients placed beside the refocusing RF pulse can be merged into diffusion gradients.

In chapter 3, a silent acquisition method of diffusion prepared RUFIS was presented. Stejskal-Tanner and flow-compensated diffusion weighting schemes were implemented. The effect of acquisition parameters on T1 signal contamination was investigated. To correct for underestimation of diffusion coefficient caused by T1 recovery during readout, a phase cycling method was employed at the cost of

prolonged scanning time. Eddy current artifacts were reduced by using dummy cycles before the diffusion preparation block. The method was validated in phantoms with different T1 values and with anisotropy properties. Accurate diffusion measurements were obtained compared to gold standard diffusion EPI. However, when the sequence was validated in volunteers for brain imaging, severe signal loss was still present even when flow-compensated diffusion weighting scheme was utilized, especially in Superior/Inferior direction. The acoustic noise reduction was 20.2 dBA compared to standard diffusion EPI, which equals to 90% reduction in sound pressure. There are several limitations in the technique presented here. First, the hard pulse in T2 preparation cannot achieve homogeneous refocusing. Second, although flow compensation was used in volunteer experiments, motion related artifacts were still observable, indicating that higher orders of motion were non-negligible to cause image degradation. For future studies, adiabatic refocusing pulse could be employed to improve the quality of T2 preparation, and further steps are needed for motion compensation.

In chapter 4, a silent 3D radial sequence was presented for quantitative mapping of T1 relaxation time and proton density, while generating time series of T1-weighted images with bias-filed correction. Inversion recovery prepared RUFIS sequence was used with an interleaved K-space trajectory. Data acquisition was segmented along the readout to generate undersampled images at different effective inversion times. Unaliased images were reconstructed by constraining the signal evolution to a temporal subspace learned from the signal model. Parameter maps were obtained by fitting the data to the signal model, and a bias-field correction method was applied to T1-weighted images. Accuracy and repeatability of the method was evaluated in experiments with phantom and volunteers. For the phantom study, T1 values obtained using the proposed method is highly consistent compared to values obtained using gold standard inversion recovery FSE, $R^2 = 0.9976$. Coefficients of variation (CVs) ranged from 0.09% to 0.83%. Region of interest analysis was used for volunteer study, T1 values from gray and white matter regions were consistent with literature values. In histogram analysis, the peaks of gray and white matter can be clearly delineated on whole-brain T1 histograms. The acoustic noise measured at the scanner isocenter was only 2.6dB higher compared to the in-bore background. To conclude, the proposed method was shown to produce accurate T1 and PD maps with high reproducibility. Rapid and with low acoustic noise, it can greatly enhance patient comfort and increase MR applications in pediatric and fetal imaging. However, both imaging

parameters and reconstruction pipeline in the current work should be optimized for different applications. As a future extension for the current work, more contrasts can be acquired by substituting inversion recovery with other preparation modules, such as T2 or diffusion. Long T2 suppression techniques can also be combined with the proposed method to characterize tissue properties for tendon or myelin, which possess short-T2 value and cannot be efficiently detected by conventional sequences.

To summarize, the thesis focuses on developing multi-contrast MRI acquisition schemes with reduced acoustic noise. The Echo Planar Imaging sequence with sinusoidal readout gradient, silent acquisition techniques for diffusion, T1 and proton density contrasts were implemented and compared to conventional methods. The proposed methods could greatly improve patient comfort during examination and therefore increase the acceptance of the procedure.

Bibliography

[1] Erwin L. Hahn. Spin echoes. *Physical review*, 80(4):580, 1950.

[2] John Pauly, Patrick Le Roux, Dwight Nishimura, and Albert Macovski. Parameter relations for the Shinnar-Le Roux selective excitation pulse design algorithm (NMR imaging). *IEEE transactions on medical imaging*, 10(1):53–65, 1991.

[3] Bjorn Stemkens, Eric S. Paulson, and Rob H. N. Tijssen. Nuts and bolts of 4D-MRI for radiotherapy. *Physics in Medicine & Biology*, 63(21):21TR01, 2018.

[4] Peter Mansfield. Multi-planar image formation using NMR spin echoes. *Journal of Physics C: Solid State Physics*, 10(3):L55, 1977.

[5] Sebastian Schmitter, E. Diesch, M. Amann, A. Kroll, M. Moayer, and L. R. Schad. Silent echo-planar imaging for auditory FMRI. *Magnetic Resonance Materials in Physics, Biology and Medicine*, 21(5):317–325, 2008.

[6] Peter Mansfield, Barry L. W. Chapman, Richard Bowtell, Paul Glover, Ron Coxon, and Paul R. Harvey. Active acoustic screening: reduction of noise in gradient coils by Lorentz force balancing. *Magnetic Resonance in Medicine*, 33(2):276–281, 1995.

[7] Z. H. Cho, S. T. Chung, J. Y. Chung, S. H. Park, J. S. Kim, C. H. Moon, and I. K. Hong. A new silent magnetic resonance imaging using a rotating DC gradient. *Magnetic Resonance in Medicine*, 39(2):317–321, 1998.

[8] A. Katsunuma, H. Takamori, Y. Sakakura, Y. Hamamura, Y. Ogo, and R. Katayama. Quiet MRI with novel acoustic noise reduction. *Magnetic Resonance Materials in Physics, Biology and Medicine*, 13(3):139–144, 2001.

[9] Franciszek Hennel. Fast spin echo and fast gradient echo MRI with low acoustic noise. *Journal of Magnetic Resonance Imaging*, 13(6):960–966, 2001.

[10] Robert A. Hedeen and William A. Edelstein. Characterization and prediction of gradient acoustic noise in MR imagers. *Magnetic Resonance in Medicine*, 37(1):7–10, 1997.

[11] F. Hennel, F. Girard, and T. Loenneker. "Silent" MRI with soft gradient pulses. *Magnetic Resonance in Medicine*, 42(1):6–10, 1999.

[12] Martin Ott, Martin Blaimer, David M. Grodzki, Felix A. Breuer, Julie Roesch, Arnd Dörfler, Björn Heismann, and Peter M. Jakob. Acoustic noise optimized diffusion-weighted imaging. *Magnetic Resonance Materials in Physics, Biology and Medicine*, 28(6):511–521, 2015.

[13] Jana Hutter, Anthony N. Price, Lucilio Cordero-Grande, Shaihan Malik, Giulio Ferrazzi, Andreia Gaspar, Emer J. Hughes, Daan Christiaens, Laura McCabe, and Torben Schneider. Quiet echo planar imaging for functional and diffusion MRI. *Magnetic Resonance in Medicine*, 79(3):1447–1459, 2018.

[14] David L. Price, Janet P. De Wilde, Annie M. Papadaki, Jane S. Curran, and Richard I. Kitney. Investigation of acoustic noise on 15 MRI scanners from 0.2T to 3T. *Journal of Magnetic Resonance Imaging*, 13(2):288–293, 2001.

[15] Matthias J. P. van Osch and Andrew G. Webb. Safety of ultra-high field MRI: what are the specific risks? *Current Radiology Reports*, 2(8):61, 2014.

[16] Maarten J. Versluis, Wouter M. Teeuwisse, Hermien E. Kan, Mark A. van Buchem, Andrew G. Webb, and Matthias J. van Osch. Subject tolerance of 7T MRI examinations. *Journal of Magnetic Resonance Imaging*, 38(3):722–725, 2013.

[17] Julie Rösch, Angelika Mennecke, Michael Knott, Arnd Doerfler, and David M. Grodzki. Quiet FLAIR at 7T MRI. *Investigative Radiology*, 55(11):722–726, 2020.

[18] Heidi Johansen-Berg and Timothy E. J. Behrens. *Diffusion MRI: from quantitative measurement to in vivo neuroanatomy*. Academic Press, 2013.

[19] Robert Turner and Denis Le Bihan. Single-shot diffusion imaging at 2.0 Tesla. *Journal of Magnetic Resonance (1969)*, 86(3):445–452, 1990.

[20] Peter Jezzard and Robert S. Balaban. Correction for geometric distortion in echo planar images from B0 field variations. *Magnetic Resonance in Medicine*, 34(1):65–73, 1995.

[21] Tomokazu Numano, Kazuhiro Homma, and Takeshi Hirose. Diffusion-weighted three-dimensional MP-RAGE MR imaging. *Magnetic Resonance Imaging*, 23(3):463–468, 2005.

[22] Susumu Mori, Ryuta Itoh, Jiangyang Zhang, Walter E. Kaufmann, Peter C. M. van Zijl, Meiyappan Solaiyappan, and Paul Yarowsky. Diffusion tensor imaging of the developing mouse brain. *Magnetic Resonance in Medicine*, 46(1):18–23, 2001.

[23] Rong Xue, Masahiko Sawada, Shozo Goto, Patricia D. Hurn, Richard J. Traystman, Peter C. M. van Zijl, and Susumu Mori. Rapid three-dimensional diffusion MRI facilitates the study of acute stroke in mice. *Magnetic Resonance in Medicine*, 46(1):183–188, 2001.

[24] J. Coremans, M. Spanoghe, L. Budinsky, J. Sterckx, R. Luypaert, H. Eisendrath, and M. Osteaux. A comparison between different imaging strategies for diffusion measurements with the centric phase-encoded turboFLASH sequence. *Journal of Magnetic Resonance*, 124(2):323–342, 1997.

[25] David L. Thomas, Gaby S. Pell, Mark F. Lythgoe, David G. Gadian, and Roger J. Ordidge. A quantitative method for fast diffusion imaging using magnetization-prepared TurboFLASH. *Magnetic Resonance in Medicine*, 39(6):950–960, 1998.

[26] Eun-Kee Jeong, Seong-Eun Kim, and Dennis L. Parker. High-resolution diffusion-weighted 3D MRI, using diffusion-weighted driven-equilibrium (DW-DE) and multishot segmented 3D-SSFP without navigator echoes. *Magnetic Resonance in Medicine*, 50(4):821–829, 2003.

[27] Lan Lu, Bernadette Erokwu, Gregory Lee, Vikas Gulani, Mark A. Griswold, Katherine M. Dell, and Chris A. Flask. Diffusion-prepared fast imaging with steady-state free precession (DP-FISP): a rapid diffusion MRI technique at 7T. *Magnetic Resonance in Medicine*, 68(3):868–873, 2012.

[28] Edwin D. Becker, James A. Feretti, and Thomas C. Farrar. Driven equilibrium Fourier transform spectroscopy. A new method for nuclear magnetic resonance signal enhancement. *Journal of the American Chemical Society*, 91(27):7784–7785, 1969.

[29] Axel Haase. Snapshot FLASH MRI. applications to T1, T2, and chemical-shift imaging. *Magnetic Resonance in Medicine*, 13(1):77–89, 1990.

[30] Catherine F. M. Williams and Thomas W. Redpath. Sources of artifact and systematic error in quantitative snapshot FLASH imaging and methods for their elimination. *Magnetic Resonance in Medicine*, 41(1):63–71, 1999.

[31] Deborah Burstein. Stimulated echoes: description, applications, practical hints. *Concepts in Magnetic Resonance*, 8(4):269–278, 1996.

[32] R. M. Cotts, M. J. R. Hoch, T. Sun, and J. T. Markert. Pulsed field gradient stimulated echo methods for improved NMR diffusion measurements in heterogeneous systems. *Journal of Magnetic Resonance (1969)*, 83(2):252–266, 1989.

[33] Eun-Kee Jeong, Seong-Eun Kim, Eugene G. Kholmovski, and Dennis L. Parker. High-resolution DTI of a localized volume using 3D single-shot diffusion-weighted stimulated echo-planar imaging (3D ss-DWSTEPI). *Magnetic Resonance in Medicine*, 56(6):1173–1181, 2006.

[34] Robert R. Edelman, Jochen Gaa, Van J. Wedeen, Evan Loh, Joshua M. Hare, Pottumarthi Prasad, and Wei Li. In vivo measurement of water diffusion in the human heart. *Magnetic Resonance in Medicine*, 32(3):423–428, 1994.

[35] Sonia Nielles-Vallespin, Choukri Mekkaoui, Peter Gatehouse, Timothy G. Reese, Jennifer Keegan, Pedro F. Ferreira, Steve Collins, Peter Speier, Thorsten Feiweier, and Ranil De Silva. In vivo diffusion tensor MRI of the human heart: reproducibility of breath-hold and navigator-based approaches. *Magnetic Resonance in Medicine*, 70(2):454–465, 2013.

[36] R. L. O'Halloran, Samantha Holdsworth, M. Aksoy, and R. Bammer. Model for the correction of motion-induced phase errors in multishot diffusion-weighted-MRI of the head: are cardiac-motion-induced phase errors reproducible from beat-to-beat? *Magnetic Resonance in Medicine*, 68(2):430–440, 2012.

[37] Jiangang Dou, Timothy G. Reese, Wen-Yih I. Tseng, and Van J. Wedeen. Cardiac diffusion MRI without motion effects. *Magnetic Resonance in Medicine*, 48(1):105–114, 2002.

[38] David P. Madio and Irving J. Lowe. Ultra-fast imaging using low flip angles and FIDs. *Magnetic Resonance in Medicine*, 34(4):525–529, 1995.

[39] M. Weiger and K. P. Pruessmann. MRI with zero echo time. *eMagRes*, 2007.

[40] David M. Grodzki, Peter M. Jakob, and Bjoern Heismann. Ultrashort echo time imaging using pointwise encoding time reduction with radial acquisition (PETRA). *Magnetic Resonance in Medicine*, 67(2):510–518, 2012.

[41] Markus Weiger, David O. Brunner, Benjamin E. Dietrich, Colin F. Müller, and Klaas P. Pruessmann. ZTE imaging in humans. *Magnetic Resonance in Medicine*, 70(2):328–332, 2013.

[42] Yaotang Wu, Guangping Dai, Jerome L. Ackerman, Mirko I. Hrovat, Melvin J. Glimcher, Brian D. Snyder, Ara Nazarian, and David A. Chesler. Water-and fat-suppressed proton projection MRI (WASPI) of rat femur bone. *Magnetic Resonance in Medicine*, 57(3):554–567, 2007.

[43] Dean O. Kuethe, Arvind Caprihan, Irving J. Lowe, David P. Madio, and H. Michael Gach. Transforming NMR data despite missing points. *Journal of Magnetic Resonance*, 139(1):18–25, 1999.

[44] Yaotang Wu, Jerome L. Ackerman, David A. Chesler, Lila Graham, Yan Wang, and Melvin J. Glimcher. Density of organic matrix of native mineralized bone measured by water-and fat-suppressed proton projection MRI. *Magnetic Resonance in Medicine*, 50(1):59–68, 2003.

[45] Fabian Springer, Petros Martirosian, Jürgen Machann, Nina F. Schwenzer, Claus D. Claussen, and Fritz Schick. Magnetization transfer contrast imaging in bovine and human cortical bone applying an ultrashort echo time sequence at 3 Tesla. *Magnetic Resonance in Medicine*, 61(5):1040–1048, 2009.

[46] Edward O. Stejskal and John E. Tanner. Spin diffusion measurements: spin echoes in the presence of a time-dependent field gradient. *The journal of chemical physics*, 42(1):288–292, 1965.

[47] Gaby S. Pell, David P. Lewis, and Craig A. Branch. Pulsed arterial spin labeling using TurboFLASH with suppression of intravascular signal. *Magnetic Resonance in Medicine*, 49(2):341–350, 2003.

[48] Michaela Soellinger, Andrea K. Rutz, Sebastian Kozerke, and Peter Boesiger. 3D cine displacement-encoded MRI of pulsatile brain motion. *Magnetic Resonance in Medicine*, 61(1):153–162, 2009.

[49] Koji Yamashita, Takashi Yoshiura, Akio Hiwatashi, Makoto Obara, Osamu Togao, Nozomu Matsumoto, Kazufumi Kikuchi, and Hiroshi Honda. High-resolution three-dimensional diffusion-weighted imaging of middle ear cholesteatoma at 3.0T MRI: usefulness of 3D turbo field-echo with diffusion-sensitized driven-equilibrium preparation (TFE–DSDE) compared to single-shot echo-planar imaging. *European Journal of Radiology*, 82(9):e471–e475, 2013.

[50] Ralf Deichmann, C. D. Good, Oliver Josephs, John Ashburner, and Robert Turner. Optimization of 3-D MP-RAGE sequences for structural brain imaging. *Neuroimage*, 12(1):112–127, 2000.

[51] Andrew L. Alexander, Jay S. Tsuruda, and Dennis L. Parker. Elimination of eddy current artifacts in diffusion-weighted echo-planar images: the use of bipolar gradients. *Magnetic Resonance in Medicine*, 38(6):1016–1021, 1997.

[52] Matt A. Bernstein, Kevin F. King, and Xiaohong Joe Zhou. *Handbook of MRI pulse sequences*. Elsevier, 2004.

[53] J. D. Trudeau, W. Thomas Dixon, and J. Hawkins. The effect of inhomogeneous sample susceptibility on measured diffusion anisotropy using NMR imaging. *Journal of Magnetic Resonance, Series B*, 108(1):22–30, 1995.

[54] Timothy G. Reese, O. Heid, R. M. Weisskoff, and V. J. Wedeen. Reduction of eddy-current-induced distortion in diffusion MRI using a twice-refocused spin echo. *Magnetic Resonance in Medicine*, 49(1):177–182, 2003.

[55] Stephen J. Gibbs and Charles S. Johnson Jr. A PFG NMR experiment for accurate diffusion and flow studies in the presence of eddy currents. *Journal of Magnetic Resonance (1969)*, 93(2):395–402, 1991.

[56] Ch Boesch, R. Gruetter, and E. Martin. Temporal and spatial analysis of fields generated by eddy currents in superconducting magnets: optimization of corrections and quantitative characterization of magnet/gradient systems. *Magnetic Resonance in Medicine*, 20(2):268–284, 1991.

[57] Thomas L. Chenevert and James G. Pipe. Effect of bulk tissue motion on quantitative perfusion and diffusion magnetic resonance imaging. *Magnetic Resonance in Medicine*, 19(2):261–265, 1991.

[58] Adam W. Anderson and John C. Gore. Analysis and correction of motion artifacts in diffusion weighted imaging. *Magnetic Resonance in Medicine*, 32(3):379–387, 1994.

[59] Dan Greitz, Ronnie Wirestam, Anders Franck, Bo Nordell, Carsten Thomsen, and Freddy Ståhlberg. Pulsatile brain movement and associated hydrodynamics studied by magnetic resonance phase imaging. *Neuroradiology*, 34(5):370–380, 1992.

[60] Christopher Nguyen, Zhaoyang Fan, Behzad Sharif, Yi He, Rohan Dharmakumar, Daniel S. Berman, and Debiao Li. In vivo three-dimensional high resolution cardiac diffusion-weighted MRI: a motion compensated diffusion-prepared balanced steady-state free precession approach. *Magnetic Resonance in Medicine*, 72(5):1257–1267, 2014.

[61] Urs Gamper, Peter Boesiger, and Sebastian Kozerke. Diffusion imaging of the in vivo heart using spin echoes-considerations on bulk motion sensitivity. *Magnetic Resonance in Medicine*, 57(2):331–337, 2007.

[62] G. A. L. L. A. N. JOHNSON and M. A. K. I. JEFFREY H. In vivo measurement of proton diffusion in the presence of coherent motion. *Investigative radiology*, 26(6):540–545, 1991.

[63] Xin Liu, Pedro A. Gómez, Ana Beatriz Solana, Florian Wiesinger, Marion I. Menzel, and Bjoern H. Menze. Silent 3D MR sequence for quantitative and multicontrast T1 and proton density imaging. *Physics in Medicine & Biology*, 65(18):185010, September 2020.

[64] Lothar Spies, Anja Tewes, Per Suppa, Roland Opfer, Ralph Buchert, Gerhard Winkler, and Alaleh Raji. Fully automatic detection of deep white matter T1 hypointense lesions in multiple sclerosis. *Physics in Medicine & Biology*, 58(23):8323–8337, nov 2013.

[65] Andreia Roque, Miguel Ramalho, Mamdoh AlObaidy, Vasco Herédia, Lauren M. Burke, Rafael O. P. De Campos, and Richard C. Semelka. Post-contrast T1-weighted sequences in pediatric abdominal imaging: comparative analysis of three different sequences and imaging approach. *Pediatric radiology*, 44(10):1258–1265, 2014.

[66] Susana Muñoz Maniega, Maria C. Valdés Hernández, Jonathan D. Clayden, Natalie A. Royle, Catherine Murray, Zoe Morris, Benjamin S. Aribisala, Alan J. Gow, John M. Starr, and Mark E. Bastin. White matter hyperintensities and normal-appearing white matter integrity in the aging brain. *Neurobiology of aging*, 36(2):909–918, 2015.

[67] Paul Tofts. *Quantitative MRI of the brain: measuring changes caused by disease.* John Wiley & Sons, 2005.

[68] Nikola Stikov, Mathieu Boudreau, Ives R. Levesque, Christine L. Tardif, Joëlle K. Barral, and G. Bruce Pike. On the accuracy of T1 mapping: searching for common ground. *Magnetic Resonance in Medicine*, 73(2):514–522, 2015.

[69] Xiawei Ou and Daniel Frank Gochberg. MT effects and T1 quantification in single-slice spoiled gradient echo imaging. *Magnetic Resonance in Medicine*, 59(4):835–845, 2008.

[70] Vasily L. Yarnykh. Optimal radiofrequency and gradient spoiling for improved accuracy of T1 and B1 measurements using fast steady-state techniques. *Magnetic Resonance in Medicine*, 63(6):1610–1626, 2010.

[71] Hai-Ling Margaret Cheng and Graham A. Wright. Rapid high-resolution T1 mapping by variable flip angles: accurate and precise measurements in the presence of radiofrequency field inhomogeneity. *Magnetic Resonance in Medicine*, 55(3):566–574, 2006.

[72] Elizabeth Henderson, Graeme McKinnon, Ting-Yim Lee, and Brian K. Rutt. A fast 3D look-locker method for volumetric T1 mapping. *Magnetic Resonance Imaging*, 17(8):1163–1171, 1999.

[73] Sam T. S. Wong and Mark S. Roos. A strategy for sampling on a sphere applied to 3D selective RF pulse design. *Magnetic Resonance in Medicine*, 32(6):778–784, 1994.

[74] Jeffrey Tsao and Sebastian Kozerke. MRI temporal acceleration techniques. *Journal of Magnetic Resonance Imaging*, 36(3):543–560, 2012.

[75] Stefanie Winkelmann, Tobias Schaeffter, Thomas Koehler, Holger Eggers, and Olaf Doessel. An optimal radial profile order based on the Golden Ratio for time-resolved MRI. *IEEE Trans Med Imaging*, 26(1):68–76, 2006.

[76] Philipp Ehses, Nicole Seiberlich, Dan Ma, Felix A. Breuer, Peter M. Jakob, Mark A. Griswold, and Vikas Gulani. IR TrueFISP with a golden-ratio-based radial readout: fast quantification of T1, T2, and proton density. *Magnetic Resonance in Medicine*, 69(1):71–81, 2013.

[77] Zhi-Pei Liang. Spatiotemporal imagingwith partially separable functions. pages 988–991. IEEE, 2007.

[78] Jeffrey Tsao, Peter Boesiger, and Klaas P. Pruessmann. k-t BLAST and k-t SENSE: dynamic MRI with high frame rate exploiting spatiotemporal correlations. *Magnetic Resonance in Medicine*, 50(5):1031–1042, 2003.

[79] Hong Jung, Jong Chul Ye, and Eung Yeop Kim. Improved k-t BLAST and k-t SENSE using FOCUSS. *Physics in Medicine & Biology*, 52(11):3201, 2007.

[80] Henrik Pedersen, Sebastian Kozerke, Steffen Ringgaard, Kay Nehrke, and Won Yong Kim. k-t PCA: temporally constrained k-t BLAST reconstruction using principal component analysis. *Magnetic Resonance in Medicine*, 62(3):706–716, 2009.

[81] Jonathan I. Tamir, Martin Uecker, Weitian Chen, Peng Lai, Marcus T. Alley, Shreyas S. Vasanawala, and Michael Lustig. T2 shuffling: sharp, multicontrast, volumetric fast spin-echo imaging. *Magnetic Resonance in Medicine*, 77(1):180–195, 2017.

[82] Committee on Environmental Health. Noise: a hazard for the fetus and newborn. *Pediatrics*, 100(4):724–727, 1997.

[83] Chao Jin, Huan Li, Xianjun Li, Miaomiao Wang, Congcong Liu, Jianxin Guo, and Jian Yang. Temporary hearing threshold shift in healthy volunteers with hearing protection caused by acoustic noise exposure during 3-T multisequence MR neuroimaging. *Radiology*, 286(2):602–608, 2018.

[84] P. Radomskij, M. A. Schmidt, C. W. Heron, and D. Prasher. Effect of MRI noise on cochlear function. *The Lancet*, 359(9316):1485–1486, 2002.

[85] J. A. Flaherty and K. Hoskinson. Emotional distress during magnetic resonance imaging. *The New England journal of medicine*, 320(7):467–468, 1989.

[86] Marc Dewey, Tania Schink, and Charles F. Dewey. Claustrophobia during magnetic resonance imaging: cohort study in over 55,000 patients. *Journal of Magnetic Resonance Imaging*, 26(5):1322–1327, 2007.

[87] Masahiro Ida, Toshiki Wakayama, Matthew L. Nielsen, Takayuki Abe, and David M. Grodzki. Quiet T1-weighted imaging using PETRA: initial clinical evaluation in intracranial tumor patients. *Journal of Magnetic Resonance Imaging*, 41(2):447–453, 2015.

[88] Samantha J. Holdsworth, Sarah J. Macpherson, Kristen W. Yeom, Max Wintermark, and Greg Zaharchuk. Clinical evaluation of silent T1-weighted MRI and silent MR angiography of the brain. *American Journal of Roentgenology*, 210(2):404–411, 2018.

[89] Sedat Alibek, Mika Vogel, Wei Sun, David Winkler, Christopher A. Baker, Michael Burke, and Hubertus Gloger. Acoustic noise reduction in MRI using silent scan: an initial experience. *Diagnostic and interventional radiology*, 20(4):360, 2014.

[90] R. Deichmann and A. Haase. Quantification of T1 values by SNAPSHOT-FLASH NMR imaging. *Journal of Magnetic Resonance (1969)*, 96(3):608–612, 1992.

[91] Debra F. McGivney, Eric Pierre, Dan Ma, Yun Jiang, Haris Saybasili, Vikas Gulani, and Mark A. Griswold. SVD compression for magnetic resonance fingerprinting in the time domain. *IEEE Trans Med Imaging*, 33(12):2311–2322, 2014.

[92] Pierre-François Van de Moortele, Edwards J. Auerbach, Cheryl Olman, Essa Yacoub, Kâmil Uğurbil, and Steen Moeller. T1 weighted brain images at 7 Tesla unbiased for Proton Density, T2* contrast and RF coil receive B1 sensitivity with simultaneous vessel visualization. *Neuroimage*, 46(2):432–446, 2009.

[93] Stephen M. Smith. Fast robust automated brain extraction. *Human brain mapping*, 17(3):143–155, 2002.

[94] Rahel Heule, Josef Pfeuffer, and Oliver Bieri. Snapshot whole-brain T1 relaxometry using steady-state prepared spiral multislice variable flip angle imaging. *Magnetic Resonance in Medicine*, 79(2):856–866, 2018.

[95] David C. Zhu and Richard D. Penn. Full-brain T1 mapping through inversion recovery fast spin echo imaging with time-efficient slice ordering. *Magnetic Resonance in Medicine*, 54(3):725–731, 2005.

[96] Xiaoqing Wang, Volkert Roeloffs, Jakob Klosowski, Zhengguo Tan, Dirk Voit, Martin Uecker, and Jens Frahm. Model-based T1 mapping with sparsity constraints using single-shot inversion-recovery radial FLASH. *Magnetic Resonance in Medicine*, 79(2):730–740, 2018.

[97] Paolo Farace, Rolando Pontalti, Luca Cristoforetti, Renzo Antolini, and Marina Scarpa. An automated method for mapping human tissue permittivities by MRI in hyperthermia treatment planning. *Physics in Medicine & Biology*, 42(11):2159, 1997.

[98] Neville D. Gai, Christian Stehning, Marcelo Nacif, and David A. Bluemke. Modified Look-Locker T1 evaluation using Bloch simulations: human and phantom validation. *Magnetic Resonance in Medicine*, 69(2):329–336, 2013.

[99] Peter Kellman and Michael S. Hansen. T1-mapping in the heart: accuracy and precision. *Journal of cardiovascular magnetic resonance*, 16(1):2, 2014.

[100] Marianne A. A. Van Walderveen, Ronald A. Van Schijndel, Petra J. W. Pouwels, Chris H. Polman, and Frederik Barkhof. Multislice T1 relaxation time measurements in the brain using IR-EPI: reproducibility, normal values, and histogram analysis in patients with multiple sclerosis. *Journal of Magnetic Resonance Imaging*, 18(6):656–664, 2003.

[101] Steven Kecskemeti, Alexey Samsonov, Samuel A. Hurley, Douglas C. Dean, Aaron Field, and Andrew L. Alexander. MPnRAGE: A technique to simultaneously acquire hundreds of differently contrasted MPRAGE images with applications to quantitative T1 mapping. *Magnetic Resonance in Medicine*, 75(3):1040–1053, 2016.

[102] S. M. Leary, G. J. M. Parker, V. L. Stevenson, G. J. Barker, D. H. Miller, and A. J. Thompson. Reproducibility of magnetic resonance imaging measurements of spinal cord atrophy: the role of quality assurance. *Magnetic Resonance Imaging*, 17(5):773–776, 1999.

[103] Jonathan I. Tamir, Valentina Taviani, Shreyas S. Vasanawala, and Michael Lustig. T1-T2 shuffling: Multi-contrast 3D fast spin-echo with T1 and T2 sensitivity. volume 25, page 0451, 2017.

[104] Zhaoyang Fan, Wei Yu, Yibin Xie, Li Dong, Lixin Yang, Zhanhong Wang, Antonio Hernandez Conte, Xiaoming Bi, Jing An, and Tianjing Zhang. Multi-contrast atherosclerosis characterization (MATCH) of carotid plaque with a single 5-min scan: technical development and clinical feasibility. *Journal of cardiovascular magnetic resonance*, 16(1):1–12, 2014.

[105] Cornelia Laule, Irene M. Vavasour, Shannon H. Kolind, David K. B. Li, Tony L. Traboulsee, G. R. Wayne Moore, and Alex L. MacKay. Magnetic resonance imaging of myelin. *Neurotherapeutics*, 4(3):460–484, 2007.

[106] Peder E. Z. Larson, Paul T. Gurney, Krishna Nayak, Garry E. Gold, John M. Pauly, and Dwight G. Nishimura. Designing long-T2 suppression pulses for ultrashort echo time imaging. *Magnetic Resonance in Medicine*, 56(1):94–103, 2006.

List of Figures

List of Tables

Acknowledgments

First and foremost, I am extremely grateful to my supervisors, Prof. Dr. Bjoern Menze and Prof. Dr. Axel Haase for their continuous support, kind of guidance and invaluable advice during my PhD study. I would also like to express my sincere gratitude to PD. Dr. Marion Menzel, who took an important part, bridging between partners in the Marie Curie Initial Training Network BERTI: Biomedical Imaging & Informatics. I genuinely appreciate the opportunities and resources you provided me for this project.

This project was conducted in close collaboration with scientists form the General Electric Research Center. I would like to thank the team manager, Dr. Timo Schirmer, for giving me trust and opportunity to learn from and be part of the team. I would also like to express my sincere gratitude to Dr. Ana Beatriz Solana, Dr. Florian Wiesinger, Dr. Jonathan Sperl and Dr. Anne Menini, your insightful feedback, dedicated support and guidance helped me go through difficult times in research.

I would like to thank Prof. Dr. Derek Jones, who supervised my work at Cardiff University Brain Research Imaging Center. Although the secondment was only for short three month, I had your support in every matter. It was a great chance to get know the colleagues in your lab and their brilliant research to better understand neurological and psychiatric conditions using state of art brain imaging techniques. Your deep knowledge, ground-breaking work and extraordinary personality has deeply inspired me.

I would also like to thank all the BERTI doctoral candidates and colleagues: Aurelien, Beatriz, Eduardo, Eugen, Fatih, Jaber, Marwan, Miguel, Ming, Nicolas, Pedro, Saeed, Shufang, Suat, Teresa, Tim and Yash. What a pleasure to get to know and work with such outstanding people like you, to share our knowledge and ideas, and spend wonderful times in summer schools and seminars. It was a privilege to join such an international, creative and supportive team. Hope our path will cross again soon in the future!

Furthermore, I would like to thank the administrative team of BERTI project and TUM Graduate Center of BioEngineering, Dr. Petra Dorfner, Katharina Lang, Dr. Andrea Glogger, Dr. Anja Drescher and Julia Knürr. You are so great at organizing activities and supported us in every way, your dedicated work added color our academic life and made everything go so smoothly!

Scientific Contributions

X Liu, PA Gómez, AB Solana, et al. Silent 3D MR Sequence for Quantitative and Multicontrast T1 and Proton Density Imaging. Physics in Medicine & Biology, 2020 65(18): 185010.

C Niu, Y Wang, AD Cohen, **X Liu**, et al. Machine Learning may Predict Individual Hand Motor Activation from Resting-State fMRI in Patients with Brain Tumors in Perirolandic Cortex. European Radiology, accepted in Dec 2020.

X Liu, PA Gómez, T Sprenger, et al. Fast, volumetric and silent multi-contrast zero echo time imaging. 25th Annual Meeting of the International Society for Magnetic Resonance in Medicine (ISMRM) 2017, Honolulu, USA.

C Niu, X Ling, P Lin, **X Liu**, M Zhang, et al. Active and Passive FMRI for Preoperative Localization of Motor Function Areas in Brain Tumor Patients. Proceedings of ISMRM 25th Annual Meeting, Honolulu, 2017.

C Niu, X Ling, P Lin, **X Liu**, M Zhang, et al. Anticorrelated Networks Dysfunction in Patients with Brain Tumor in Frontal Lobe. Proceedings of ISMRM 25th Annual Meeting, Honolulu, 2017.

X Liu, MI Menzel, F Wiesinger, et al. 3D Distortion Free Diffusion MRI using Magnetization Prepared RUFIS. ISMRM Workshop on Diffusion MRI, Lisbon, 2016.

C Niu, **X Liu**, Y Yang, et al. Assessing Region of Interest Schemes for the Corticospinal Tract in Patients with Brain Tumors. Medicine 2016 95(12): e3189.

C Niu, **X Liu**, P Lin, Z Min, W Li, L Guo, M Wang, Q Li, M Zhang. Combing fMRI and probabilistic DTI tractography to improve corticospinal tract visualization in patients with brain tumor. Proceedings of ISMRM 24th Annual Meeting, Singapore, 2016.

B Dionisio Parra, H Nicolas, **X Liu**, M Middione, et al. New perspectives in simultaneous EEG-fMRI using multiband and quiet pulse sequences. Proceedings of ISMRM 24th Annual Meeting, Singapore, 2016.

X Liu, F Wiesinger, AB Solana, et al. A Simulation Framework to Investigate T1 Contamination on Diffusion Prepared RUFIS. Proceedings of ESMRMB Edinburgh, Magn Reson Mater Phy 2015, vol 28.

X Liu, Y Yang, P Lin et al. Reproducibility of Diffusion Tensor Imaging in Normal Subjects: an Evaluation of Different Gradient Sampling Schemes and Registration Algorithm. Neuroradiology 2014, 56(6): 497–510.